NANYANG TECHNOLOGICAL UNIVERSITY

# Aromatic Heterocyclic Resin: Precursor for Carbon Materials and High Temperature Foams

Liu Ming

School of Materials Science and Engineering
Nanyang Technological University

2012

# Aromatic Heterocyclic Resin: Precursor for Carbon Materials and High Temperature Foams

Liu Ming

A thesis submitted to the Nanyang Technological University in fulfillment of the requirement for the degree of Doctor of Philosophy

2012

# ACKNOWLEDGEMENTS

I wish to extend my sincerest gratitude and appreciation to the following persons, who have made invaluable contribution towards the completion of this research project.

I would like to express my heartfelt gratitude to my supervisor Prof Hu Xiao for his influential role during the PhD course not only in pursue of knowledge but more importantly in character building. His constant encouragement and invaluable advices made this work possible and me a mature adult.

The support and encouragement from my beloved family were the greatest assets to me without them nothing could have been accomplished smoothly. This work is dedicated to them for their love, care and their constant support in every possible way.

Next, I would like to deliver my sincere thanks to Dr. Dai Jie from DSO National Laboratories for his valuable discussion and suggestions, and to all the professors, technicians and fellow group mates for their useful assistance in countless ways. To my fellow colleagues in the post graduate room in Polymer Laboratory for the laughter and joy, their presence lightened up the dull moments throughout the course.

Finally, I would like to acknowledge the Nanyang Technological University, Defence Science & Technology Agency and Temasek Laboratories @NTU for providing scholarship and financial support.

# TABLE OF CONTENTS

**ABSTRACT** ..... i
**ABBREVIATIONS** ..... iii
**LIST OF FIGURES** ..... v
**LIST OF TABLES** ..... viii

**1 INTRODUCTION** ..... 1
**1.1 Research Background and Current Challenges** ..... **1**
**1.2 Objectives and Scope of this Research** ..... **4**
**1.3 Thesis Organization** ..... **6**

**2 LITERATURE REVIEW** ..... 7
**2.1 Polymer for High Temperature Applications** ..... **7**
2.1.1 Phthalonitrile-Based High Temperature Resin ..... 7
2.1.2 Curing of Phthalonitrile Thermosetting Polymer ..... 8
2.1.3 Structural Formation during Polymerization ..... 11
**2.2 Carbon Materials Developed from Organic Precursor** ..... **15**
2.2.1 Methods for Producing Carbon Films ..... 16
2.2.2 Organic Precursors for Carbon Materials Preparation through Pyrolysis ... 17
2.2.3 Structural Formation and Characterization of Carbon Materials ..... 17
**2.3 Polymer Foam** ..... **20**
2.3.1 Fundamental Principles of Foam Formation ..... 21
2.3.2 Nanofillers for Nanocomposite Foam ..... 29
2.3.3 Effects of Nanofillers on Foam Quality ..... 33
2.3.4 Effects of Nanofillers on Foam Properties ..... 33
2.3.5 State of the Art Foams for HT Applications ..... 35
**2.4 Blowing Agents for Polymer Foams** ..... **36**
2.4.1 Blowing Agents selection ..... 37

**3 RESORCINOL BASED PHTHALONITRILE (RPH) RESIN: THERMAL PROPERTIES AND CARBONIZATION STUDIES** ..... 39
**3.1 Experimental** ..... **40**
3.1.1 Materials ..... 40
3.1.2 RPh polymerization and carbonization ..... 41

3.1.3 Characterization ..... 42
**3.2 Results and Discussion ..... 44**
3.2.1 Synthesis of RPh ..... 44
3.2.2 Thermal Properties of RPh ..... 44
3.2.3 Structural Formation during Curing and the Relationship to Thermal Properties ..... 51
3.2.4 Development of Carbon Materials using RPh Precursor ..... 58
**3.3 Summary ..... 65**

**4 PREPRATATION AND PROPERTIES OF RPH FOAM** ..... 67
**4.1 Experimental Procedures ..... 68**
4.1.1 Chemical Blowing Agents (CBA) Studies ..... 68
4.1.2 Viscosity of Polymer Melt ..... 69
4.1.3 Theoretical Calculations ..... 69
4.1.4 Foaming Process ..... 70
4.1.5 Characterizations ..... 71
**4.2 Results and Discussion ..... 72**
4.2.1 RPh Foam Preparation ..... 72
4.2.2 Thermal Stabilities of RPh Foams ..... 80
4.2.3 Mechanical Properties of RPh Foams ..... 83
**4.3 Summary ..... 85**

**5 NANOCOMPOSITE RPH FOAMS** ..... 87
**5.1 Experimental ..... 88**
5.1.1 Materials ..... 88
5.1.2 Viscosity Profile of Nanofiller Filled Polymer Melt ..... 89
5.1.3 Nanocomposite Foam Preparation ..... 89
5.1.4 Foam Characterizations ..... 89
**5.2 Results and Discussion ..... 90**
5.2.1 Nanocomposite Foams Fabrication ..... 90
5.2.2 Effects of Nanofillers on Thermomechanical Properties of Nanocomposite Foams ..... 99
5.2.3 Effects of Nanofillers on Compression Properties of Nanocomposite Foams ..... 101
5.2.4 Effects of Nanofillers on Thermal Properties of Nanocomposite Foams ..... 104
**5.3 Summary ..... 105**

**6 CONCLUSIONS AND RECOMMENDATIONS FOR FUTURE WORK** ..... 107

**6.1 Conclusions ..... 107**

6.1.1 Structural formation and carbonization studies of RPh resin ..... 107

6.1.2 Foaming strategy for RPh Foam Fabrication ..... 108

6.1.3 Nanofillers for Foam Morphology and Properties Enhancement ..... 109

**6.2 Recommendations for Future Studies ..... 110**

**LIST OF PUBLICATIONS** ..... I

**REFERENCES** ..... II

**APPENDICES** ..... XII

I Curing Kinetics Studies of RPh Resin ..... XIII

II Degradation Kinetics of RPh Resin ..... XV

III MWNT and GH Surface Modifications ..... XVIII

IV Supporting Figures ..... XX

# ABSTRACT

Phthalonitrile based polymers have been intensively and persistently studied over the past few decades due to their potential as high temperature (HT) resistant thermoset. All studies so far emphasised on the resin formulation as HT matrices. This study focused on understanding the detailed structural formation responsible for the superior thermal properties of resorcinol-based phthalonitrile (RPh) polymer and extending its applications as organic precursors for carbon materials and resin for ultra-low density HT foams.

High crosslinking density was essential in order to acquire the exceptional thermal performances, although Fourier Transform Infrared Spectroscopy indicated the formation of less thermally stable linear structure formation at high curing additive content. It was proposed that the trapping of the linear chains inside the cavities of the aromatic heterocyclic structures formed a highly crosslinked and thermally resistant system. Systematic studies on kinetic of curing and degradation further supported the hypothesis. The 86% char yield at 800 °C makes RPh an excellent carbon precursor. The results showed that the carbon films obtained through pyrolysis of RPh precursor were smooth and crack free, exhibiting excellent mechanical robustness and integrity which were comparable or even surpassed the carbon films obtained from epoxy or pitch. The obtained bulk electrical conductivity of 87 S/cm made RPh carbon film a potential candidate for electronic applications.

RPh foams were prepared for the first time via a synchronized single step gelation-foaming process based on the established resin viscosity profile and chemical blowing agent gas liberation. The density could be precisely controlled with the lowest obtainable density of 0.04 g/cm$^3$. Well-distributed closed cells were obtained. The RPh foams showed excellent short and long term thermal stability and strength retention (>90%) after thermal aging at 280 °C for 100 hours in air which surpassed any reported polymer foams.

Three types of nanofillers with distinct aspect ratios, 0D fumed silica (FS), 1D multiwall carbon nanotubes (MWNT) and 2D expanded graphite nanosheets (GH) were selected for nanocomposite foam preparation. Results showed the nanofillers functioned as nucleation agents, rheological modifiers and reinforcement fillers. The cell density was increased by

3 orders of magnitude and the cell size distribution was narrowed. Unique ‘cage-like’ structures consisted of closed cells interconnected by microvoids were obtained. The formation of physical gel upon MWNT made foaming possible when synchronization of gelation and gas liberation cannot be established. Three fillers were found to provide varying levels of enhancement of the nanocomposite foam properties with GH being the most effective filler. Reinforcement mechanisms were proposed to explain the findings.

# ABBREVIATIONS

| | |
|---|---|
| AFM | Atomic force microscopy |
| APB | 1,4-bis-(4-aminophenoxy) benzene |
| CBA | Chemical blowing agent |
| CNT | Carbon nanotubes |
| DMA | Dynamic mechanical analysis |
| DMSO | Dimethyl sulfoxide |
| DSC | Differential scanning calorimetry |
| DTGA | Differential thermal gravimetric analysis |
| FS | Fumed silica |
| FTIR | Fourier transform Infra-red |
| E' | Storage modulus |
| E" | Loss modulus |
| GH | Expanded graphite |
| MWNT | Multi-walled carbon nanotubes |
| PI | Polyimide |
| RPh | Resorcinol based phthalonitrile |
| SEI | Scanning electron imaging |
| SEM | Scanning electron microscopy |
| $T_{5wt\%}$ | On set degradation, defined at 5 % weight loss |
| $T_g$ | Glass transition temperature |
| TEM | Transmission electron microscopy |
| TGA | Thermal gravimetric analysis |
| $T_m$ | Melting temperature |

| | |
|---|---|
| A | Total interfacial area |
| a | Conversion |
| $C_E$ | Equilibrium Concentration |
| $C_i$ | Concentration of heterogeneous sites |
| $C_s$ | Saturation Concentration |
| $\Delta F$ | Change in free energy |
| $\Delta G_{crit}$ | Critical nucleation formation energy |

| | |
|---|---|
| $E_a$ | Activation energy for curing |
| $E_d$ | Activation energy for thermal decomposition |
| $f_i$ | Frequency factor of gas molecules joining the nucleus |
| g | Surface Tension |
| I | Intensity |
| $k_B$ | Boltzmann factor |
| $N_o$ | Cell density |
| P | Pressure |
| q | heating rate |
| R | Radius of bubble |
| $r_p$ | Polymer density |
| $r_f$ | Foam density |
| T | Absolute temperature |
| $T_{peak}$ | peak exotherm temperature |
| $T_{max}$ | Temperature at maximum weight loss |
| $V_f$ | Void fraction |
| $W_{max}$ | Residual weight at maximum rate of weight loss |

# LIST OF FIGURES

Figure 2-1 Ternary phase diagram of amorphous carbon. $sp^3$, $sp^2$ and H at corners correspond to diamond, graphite and hydrocarbon respectively[54].....19

Figure 2-2 (a) Low-density open cell foam (b) High-density closed cell foam (c) Structural foam with cellular core and integral solid skin [61].....20

Figure 2-3 Relationship between changes in gas concentration in a polymer melt and bubble nucleation and growth of foam cells [11]. .....22

Figure 2-4 Surface geometry of nucleating agents with rugged surface, β indicate the semiconical angle [69]. .....24

Figure 2-5 Reduction of critical nucleation energy by nucleating agent properties. f (m,*w*) is a function of surface contact angle and surface curvature, *w* is relative radius of nucleating agent [70].....26

Figure 2-6 (a) (b): Low density polyurethane and polystyrene foam showing cells in polyhedral shape, (c) high density PS foam showing rather spherical cells [71-73].....27

Figure 2-7 Schematic showing typical fumed silica.....31

Figure 2-8 Schematic of single- walled nanotube and multi-walled nanotube.....31

Figure 2-9 Schematic illustration of preparing expanded graphite.....32

Figure 2-10 SEI images of (a) PS foams, (b) PS/2% commercial clay, and (c) PS/5% clay produced by in-situ polymerization [70].....33

Figure 2-11 Ashby Diagram for strength vs. maximum service temperature for materials selection[122].....36

Figure 3-1 Progressive curing profile used for curing and postcuring of RPh polymer.41

Figure 3-2 (a) TGA and (b) DTGA curves of RPh with 5 mol% APB underwent progressive curing. Tests were done in flowing $N_2$, heating rate of 10 ºC/min. .....46

Figure 3-3 Storage modulus (a) and tan δ (b) of RPh/APB polymer at different curing stages (5 mol% APB). .....48

Figure 3-4 FTIR spectra of RPh with 0, 2, 5, 10 and 20 mol% of APB as curing additive after curing at 220ºC for 2 hours.....52

Figure 3-5 FTIR spectra of RPh with 5 mol% APB and 20 mol% APB at different curing stages.....54

Figure 3-6 Conversion of C≡N group as a function of curing and postcuring stages. ...55

Figure 3-7 Relative peak intensity for triazine (1520 $cm^{-1}$ and 1360 $cm^{-1}$) and phthalocyanine (1010 $cm^{-1}$) with (a) 5 mol% APB and (b) 20 mol% APB..56

Figure 3-8 SEI images of cross sections of carbonized films at 300, 500, 800 and 1000 ℃. .....59

Figure 3-9 AFM images of the surface morphologies of the films carbonized at 300, 500, 800 and 1000 ℃.RMS is surface roughness in root mean square. .....60

Figure 3-10 Raman Spectra of RPh films carbonized at different temperature obtained at room temperature. Inset shows $I_D/I_G$ ratio. ..... 64

Figure 4-1 Schematic showing the experimental set up for determination of gas liberation number of gas forming agents. ..... 69

Figure 4-2 TGA thermographs showing CBA thermal decomposition under isothermal heating. ..... 73

Figure 4-3 TGA thermographs showing CBA decomposition at 220 °C under different heating rate. ..... 73

Figure 4-4 Viscosity of RPh/APB at different temperature ..... 75

Figure 4-5 Diagram showing the relationship between gas liberation and viscosity change at 190 °C and 220 °C. ..... 75

Figure 4-6 SEI images showing foam morphologies of RPh foams foamed at (a) 200 °C and (b) 280 °C. ..... 76

Figure 4-7 SEI images showing morphologies for foams with (a) 1.5, (b) 2.5 and (c) 3.0 wt% of CBA, all foams have the density of 0.15g/cm$^3$ , and foamed under 220 °C. (d), (e) and (f), present the cell size distribution in terms of percentage. ..... 78

Figure 4-8 Nomenclature of a typical cell structure and the development stages of rigid RPh foam. Step 1 shows foaming mixture, Step 2 shows bubble growth, Step 3 shows cell coalescence during cell growth and step 4 shows the final bimodal foam structure. ..... 80

Figure 4-9 (a) TGA and (b) DTGA graphs showing effects of postcuring on thermal stability in nitrogen. (Foam used: density 0.15 g/cm$^3$, 2.5 wt% CBA). ..... 82

Figure 4-10 TGA graphs showing effect of density thermal stability in $N_2$. ..... 83

Figure 4-11 Stress-strain curves of foam samples up to densification, insert showing the stress-strain curve for strain range of 0-15 %. ..... 84

Figure 4-12 $\sigma_y$, $\sigma_{50}$ (fully filled symbol) as a function of foam density, and , $\sigma_{50}$ retention (hollow symbol) for foams subjected to thermal aging at 280 °C for 100 hours in air. ..... 85

Figure 5-1 SEI images of foam morphologies for (a) RPh foams ..... 91

Figure 5-2 Complex viscosity of RPh/nanofillers systems as a function of time at constant shear rate of 1/s. ..... 92

Figure 5-3 TEM images showing bubbles formation at nanofiller-rich regions. (a) RPh/FS foam, and (b) RPh/MWNT foam. ..... 94

Figure 5-4 Cell size distribution of (a) RPh foam, (b) FS/RPh foam, (c) MWNT/RPh foam, and (d) GH/RPh foam. ..... 96

Figure 5-5 SEI images showing dispersion state of (a) 2 wt% FS, (b) 2 wt% MWNT and (c) 2 wt% GH in RPh matrix, and (d) (e) and (f) are respective images showing the filler rich sites under higher magnifications. Insert scale bar represents 100 nm. ..... 97

Figure 5-6 Schematics illustrating concentration restoration of nanofiller cluster in the cell wall, the polymer melt was dragged along with the nanofiller, led to cell

thinning and eventually rupture when the underlying polymer failed to restore the thinned cell membrane. SEI images showing microvoid being initiated at FS cluster.....98

Figure 5-7 Schematics illustrating cell wall rupture initiated by particle existing in the cell wall due to dewetting. .....99

Figure 5-8 Storage modulus and loss modulus of RPh/FS foams. .....100

Figure 5-9 Storage modulus for different nanocomposite foams as a function of filler content. .....101

Figure 5-10 Compression stress-strain curves for nanocomposite foams at density of 0.12 g/cm$^3$ at room temperature. .....102

Figure 5-11 Specific compression stress as a function of nanofiller content at foam density of 0.12 g/cm$^3$. .....103

Figure 5-12 Schematic illustration of a cell and the cell wall. TEM miages showing the nanofillers dispersion state in the cell walls of (a) FS, (b) MWNT and (c) GH. The micrographs were taken in the direction perpendicular to the cell wall thickness direction.....103

Figure 5-13 SEI images of GH enhanced RPh foam (a) on cell strut and (b) “Armoured cells”.....104

Figure I-1 Typical dynamic DSC thermograms of RPh/APB system.....XIII

Figure II-1 DTGA curves of typical RPh/APB system at different heating rate in (a) $N_2$ and (b) air. .....XVI

Figure II-2 Kissinger plots of the main degradation stage of RPh/APB systems in $N_2$..... .....XVI

Figure III-1 SEI images of the treated MWNT and GH. .....XIX

Figure IV-1 Complex viscosity of RPh/nanofillers systems as a function of time at constant shear rate of 1/s and viscosity change under dynamic shear rate. XX

Figure IV-2 Storage modulus and loss modulus of the nanocomposite foams (a) (d): FRPh/FS, (b) (e):RPh/MWNT, and (c) (f): RPh/GH. Pure RPh foams were included in (a) and (d) as reference. Reference is taken as 0 wt% filler....XXI

# LIST OF TABLES


Table 2-1 List of available phthalonitrile based polymer and the thermal properties.....9

Table 2-2 List of different nanofillers, the geometries, and surface area to volume ratios.....30

Table 2-3 Theoretical and experimental properties of carbon nanotubes and graphene [93-99].....32

Table 3-1 The thermogravimetrical parameters obtained from TGA analysis done in $N_2$ corresponding to different curing stages. $T_g$ was determined from the tan δ peak from storage modulus versus temperature curves in Figure 3-3. .....47

Table 3-2 The thermogravimetric parameters corresponding to cured RPh/APB resin systems at a heating rate of 10 ºC/min in $N_2$ and air.....50

Table 3-3 Activation energy for curing ($E_a$) and activation energy for thermal decomposition ($E_d$) corresponding to cured RPh/APB resin. .....50

Table 3-4 Mechanical properties of RPh films carbonized in Argon gas. .....62

Table 3-5 Conductivity, integrated area ratio of $I_D/I_G$ and the corresponding $L_a$ domain size. .....65

Table 4-1 Gelation time for RPh/curing additive at different temperature. .....74

Table 4-2 Relationship of CBA content in wt% to foam density, foaming grade, average cell diameter, and cell density. .....77

Table 4-3 Thermal oxidative parameters of RPh foams obtained by TGA.....81

Table 5-1 Foam density, cell density and average cell diameter of pure and nanocomposite RPh foams.....95

Table 5-2 Thermal properties of RPh/FS foams.....104

Table 5-3 Thermal properties of RPh/MWNT foams. .....105

Table 5-4 Thermal properties of RPh/GH foams. .....105

Table I-1 Peak exotherm temperatures at different heating rates and the corresponding Ea of the RPh/APB systems obtained by Kissinger method.....XIV

Table II-1 $T_{max}$ and Ed of the major degradation stage of RPh/APB resin in $N_2$ and in air calculated by the Kissinger equation. ..... XVII

# 1 INTRODUCTION

## 1.1 Research Background and Current Challenges

In an effort to identify advanced polymeric materials to be used for high temperature (HT) applications, polymers with short and long term high thermo-oxidative stability have been heavily investigated. However, most organic polymers decompose when heat to moderate or high temperature. For this reason, only few are able to withstand long period of time at temperature above 150-200 °C. Snow and Griffith demonstrated the condensation of tetranitrile under appropriate conditions produced thermally stable polymers consisting of aromatic heterocyclic units [1]. Keller from the United States Naval Research Laboratory later on synthesized and patented a whole family of phthalonitrile based resin demonstrating superior thermal properties which surpassed many HT resistant polymers such as BMI, polyimide and phenolic resins [1-6]. Most of his investigations focused on the resin formulation and properties characterization, curing mechanism and structural formations during crosslinking were less studied. The high processing temperature and long processing time made phthalonitrile resin a less studied material and the applications were limited to bulk and composite applications. No attempt was ever made to expand the potential applications of this class of thermoset. The high char yield and thermal stability made it worthwhile to investigate the possibility of using phthalonitrile resin as precursor for carbon material development and extend its application to areas dominated by carbon materials.

Besides bulk polymer resin, porous structure for HT applications is another area worth looking into for phthalonitrile resins. Polymeric foams are cellular plastics consist of a continuous solid phased with gas phase defining the voids. The history of polymer foam

can be traced back to the 1950's where the first phenolic foam was produced unintentionally. Since then polymer foams are found virtually in every aspect of the modern world and are used in a wide variety of applications such as disposable packaging, furniture cushioning, insulation materials, and even in surfboards and aeroplanes. However, few reports were targeted for HT foam developments and often were found with shortcomings. For instance, foams made from epoxy, polyurea, polypyrrones, and phenolic resins have unsatisfactory service temperature (usually below 200 °C) [7-10]. Foaming of polybenzimidazoles (PBI) required temperature above 400 °C [11], the rigid polyimide (PI) foam developed by the National Aeronautics and Space Administration required tedious fabrication procedures [12]. Till now, there were no reports on any foam systems which can be used at temperature more than 300 °C for an extended period of time. Using phthalonitrile based thermoset for HT foam development maybe a feasible solution which has not been reported yet.

The success of many foam fabrications depend on the proper selection of a gas releasing agent which matches the solidifying process of the polymer matrix. Temperature, heating rate, pressure and rheology are important foaming parameters to be synchronized during the foaming process, mismatch of any of the parameters would lead to foaming failure. However, to establish a proper foaming condition for phthalonitrile resin is a challenging task due to the less establish crosslinking mechanism and long crosslinking time(up to days). Till now, all reports on phthalonitrile resin were based on void free resin development with long gelation time. No one has attempted to reduce the gelation time, which is an important requirement for foaming applications in order to match the short gas liberation time frame form the blowing agents. The high processing temperature also limited the selection of suitable gas forming materials. This study aimed to look into the

areas which were less studied and yet important for foam preparation and establish a facile and effective foaming methodology.

HT foams found its applications in many attractive areas such as aerospace, defence and electronic industries. However, when being used in these fields, it is necessary to improve the thermal and mechanical properties further. There is little doubt that incorporating nanofillers in a polymer matrix will lead to tremendous improvements in various aspects of material performances. When come to delicate systems such as film or foam where at least one of the dimensions is in the submicron regime, the nano-sized fillers appeared to be the most appropriate candidates. Fundamental understanding of the correlation between nanocomposite processing and foam development is necessary for the preparation of the nanocomposite foam. The effectiveness of nanofillers functioning as nucleation agents needs to be understood. The influence of nanofillers on the gelation and rheological properties of the nanocomposite needs to be investigated systematically. The in-depth understandings generated will assist in the effective development of phthalonitrile nanocomposite foams and serve as a critical prerequisite for tailoring of the morphology-dependant foam properties.

## 1.2 Objectives and Scope of this Research

It is evident that it is worthwhile to explore and expand the potential applications of phthalonitrile foams due to its exceptional thermal performance. The objectives and scope of research include:

*(1) To identify the intrinsic factors and structural formations responsible for the superior thermal properties and explore its potential as organic precursor for carbon materials development.*

The thermal properties were explored in terms of post curing conditions and the curing additive content. FTIR was employed to trace the macrostructural formation to provide insights of the high thermal properties. Kinetic of curing and degradation were systematically studied to support the hypothesis made on the factors affecting the thermal behaviour. Carbon materials were developed through pyrolysis at different temperature. The resultant films were cahratcerized in term of morphology, mechanical and electrical properties using Atomic Force Microscope (AFM), Scanning Electron Microscope (SEM), nanohardness tester, and Raman Spectroscopy.

*(2) To establish a synchronized polymer crosslinking- gas liberation process for effective and well controlled foam fabrication and to investigate the structure/property relationship of phthalonitrile based foam.*

Polymer melt viscosity profile and the gas liberation process of blowing agents were systematically studied under different temperatures and heating rates in order to establish a balanced relationship of the two parameters for successful foaming. The foaming parameters were optimized for controlling the foam development. The foam morphology,

thermal and mechanical property were characterized by SEM, TGA, and Instron mechanical tester.

(3) *To investigate the nucleation efficiency of nanofillers and their effects on rheological behaviour of the nanofiller/polymer melt in order to establish nucleation-foaming-morphology relationship.*

Three types of nanofillers with distinctly different aspect ratio were used for the study. Foam morphologies were observed using SEM and discussed with respect to the rheological changes caused by different nanofiller additions. The formation of unique porous structure was studied and discussed. Direct evidence of nanofillers as nucleation agent was observed using Transmission Electron Microscope (TEM). Foam qualities including foam morphology, cell size distribution, and cell type were examined and calculated.

(4) *To study the effects of nanofillers on the thermal, thermo-mechanical and mechanical properties of nanocomposite foams to gain insight into morphology/structure relationship of phthalonitrile based nanocomposite foam.*

It is essential to study the effects of type of nanoparticles on the foam quality for target-specific foam development. The thermal and mechanical properties were investigated for different type of nanocomposite foams and discussed based on the foam structure and effects of filler type. The reinforcement mechanisms of nanofillers on foam structure were proposed.

## 1.3 Thesis Organization

This thesis is organized into 5 main chapters. Chapter 2 reviews the past literatures of interest pertaining to this work including, high temperature resistant polymer resin, its preparation and properties, fundamentals of foaming process in polymer system and a brief introduction on effects of nanofillers in foam development. Chapter 3 identified resorcinol-based phthalonitrile polymers (RPh) to be a suitable candidate for high temperature applications. Hypothesis on the factor responsible for the superior thermal properties was proposed and supported by systematic studies. The superior thermal properties were highlighted. Carbonized RPh films were obtained and characterized. Chapter 4 reported the fabrication of RPh foam. The effects of various foaming parameter: curing temperature, chemical blowing agent content on foam morphology and quality were discussed. The thermal and mechanical properties and the mechanical property retention upon long term thermal aging were reported. Chapter 5 detailed the development of RPh nanocomposite foams. The roles of nanofillers in foam development were discussed in detail. The thermal and mechanical properties were reported and reinforcement mechanism of various nanofillers was proposed. Chapter 6 summarized the main findings of this work and presented the future recommendations.

# 2 LITERATURE REVIEW

## 2.1 Polymer for High Temperature Applications

For the last few decades, much success was achieved in synthesizing polymers that exhibited outstanding thermal stability. The key to such success was to incorporate highly thermal stable structures such as aromatic and/or heterocyclic rings into the resin systems. [4]. These cyclic rings in the chain made rotation of chain segments difficult and hence resulted in polymers which are more resistant to deformation, having higher melting points and glass transition temperatures.

### 2.1.1 Phthalonitrile-Based High Temperature Resin

Bisphthalonitriles were first used as precursors for high temperature resistance polymer synthesis about 50 years ago by Marvel and Martin [13] when they attempted to produce a network of linked phthalocyanine units. The inflexibility in spacer group between the phthalonitrile ends of the monomers resulted in material consisted of only two to three linked units. Monomers with spacer group containing flexible carbon chains, such as aliphatic diamides and ethers, fluorinated hydrocarbon chains, and small polyphenyl ethers were synthesized, greater reaction appeared to be evident [5, 14-18]. A thermally stable polymer with high $T_g$ and char yield was obtained by heating the phthalonitrile monomers alone at an elevated temperature of 280°C for 6 days. However, the high curing temperature and long curing time make it impractical for processing. New monomer designs were attempted to bring down the processing temperature. It was demonstrated that by attaching the reactive terminal phthalonitrile ends with aromatic ether spacer group, the softening temperature was decreased by about 75°C, the melt became completely free-flowing around 145°C (comparing to ~280 °C) [4]. The long curing time was drastically reduced form days to mere couple of hours by heating the

monomer with appropriate co-reactants or curing additives including amines, strong organic acids, metals, and metallic salts [1, 14, 19, 20].

Keller from the United States Naval Research Laboratory has intensively synthesized and patented a series of phthalonitrile based monomers over the past few decades, with bisphenol [6, 17], aromatic ether [4], phosphine oxide [21, 22], and thioether [2, 23], ect. as spacer linkages being incorporated between the terminal phthalonitrile units. A summary of the currently available phthalonitrile based polymer, their chemical structures, physical and thermal properties were summarized in Table 2-1.

### 2.1.2 Curing of Phthalonitrile Thermosetting Polymer

Ideally, the energetically favourable highly aromatic phthalocyanine formation will transform the phthalonitrile monomers into an aromatic heterocyclic macromolecular network. However it was mentioned in all reports that the neat polymerization of phthalonitrile monomers requires continuous heating for several days at elevated temperature before viscosity increase was detected. This slow polymerization rate was believed to be attributed to the rigid linking sites or the absence of active hydrogen to initiate the nitrile groups [1]. The presence of metal or metallic salts, proton-donating organic reducing agents, coreactants or initiator were hence added to accelerate the polymerization reaction.

**Table 2-1 List of available phthalonitrile based polymer and the thermal properties.**

| Phthalonitrile Based Resins | | Melting Point °C | Char Yield and Postcuring Conditions |
|---|---|---|---|
| Bisphenol Phthalonitrile [23] | 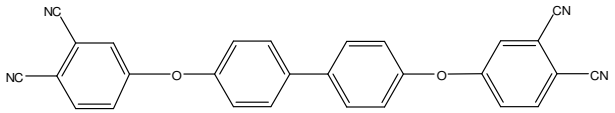 | 232 | 78% at 800 °C in $N_2$. Postcured at 316 °C for 15 hours, 350 °C for 2 hours |
| Bisphenol A Phthalonitrile [17] | 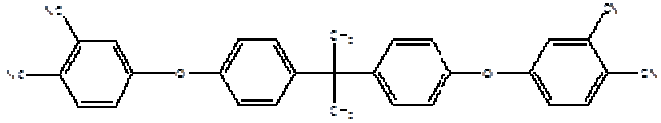 | 195 | 79% at 1000°C in $N_2$. Postcured at 375 °C for 4 hours, 425 °C for 8 hours |
| Imide containing Phthalonitrile [3] | 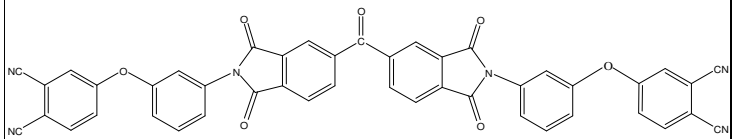 | 245-248 | 64% at 800 °C in $N_2$. Postcured at 315 °C for 16 hours, 375 °C for 24 hours |

| | | | |
|---|---|---|---|
| Phthalonitrile - Functional Polybenzoxazines [24, 25] | 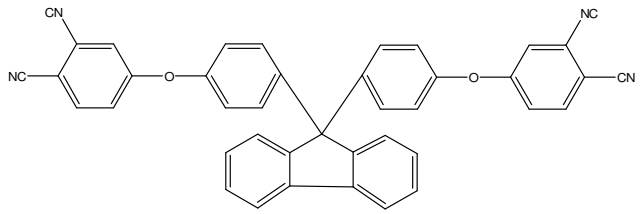 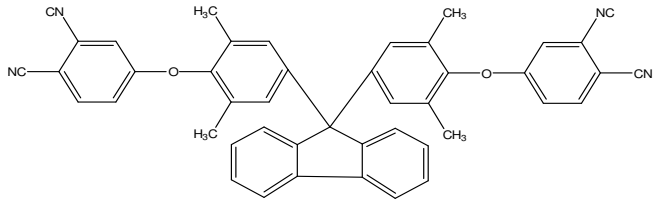 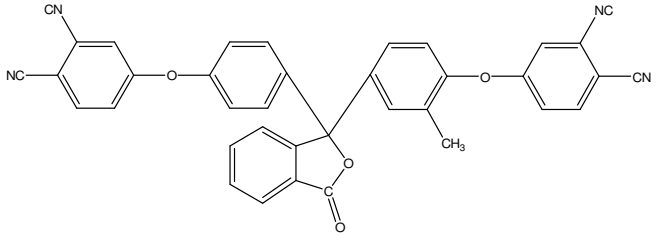 | | At 800 °C in $N_2$. Postcured at 250 °C for 6 hours<br>76 %<br>80%<br>68% |

Wöhrle and co-workers carried out thorough studies on the formation of polyphthalocyanine using finely divided metals and metallic salts as curing additives [20]. However, the incomplete molecular dispersion of the metals and their salts in the organic matrix greatly restricted the obtainable degree of conversion, and the metal-oxidation deteriorated the resin's resistance to heat when being exposed to oxidizing atmosphere. Organic coreactants became a more favourable choice for being soluble in the polymeric network and formed metal-free phthalocyanine. Hydroquinone was used by Snow to promote the reaction [14], but the curing additives were unable to incorporate into the polymer structure when present in large quantity. This problem was overcame by using reducing agents which contained phthalonitrile group, as being demonstrated by Pascal and co-workers [26] who used 3.4-dicyanobenzhydrol as co reactant in the polymerization. Keller and Price showed amine to be an excellent cutting additive and the amine cured phthalonitrile polymers were more thermally stable than their neat cured counterparts without significant deterioration in the mechanical properties [27, 28].

Effective curing additives have greatly accelerated the curing process; however there were not many reports discussed the polymerization and structural formation in details. This is mainly due to the difficulties in separating the macrostructures formed during the complex crosslinking process for analysis. Nevertheless, the formations for some of the structures were discussed individually through model studies and will be explained in more details in the later part of this chapter.

### 2.1.3 Structural Formation during Polymerization

The highly crosslinked complex system made structure characterization challenging, and a high degree of structural uncertainty remained till today. The crosslinked thermoset was

believed to be consisted of a mixture of linear chain of polyisoindolenine and macrocyclic structures of polypthaloncyanine and polytriazine depending on the amount and the type of curing additive used. Several reaction schemes were proposed by various groups and were summarized and presented.

***Polyisoindolenine***: It was suggested that amine curing additive added to the phthalonitrile monomer melt would initially attacked the C≡N group to produce a N-substituted-3-iminosoindoline unit (X) as illustrated in Scheme 2-4 [1]. This reaction involves only one of the phthalonitrile units and X is believed to be a reactive self-propagating species that attacks other C≡N groups led to chain extension and reactive chain end regeneration to occur. The reactions continued till eventually form the linear polyisoindolenine chain.

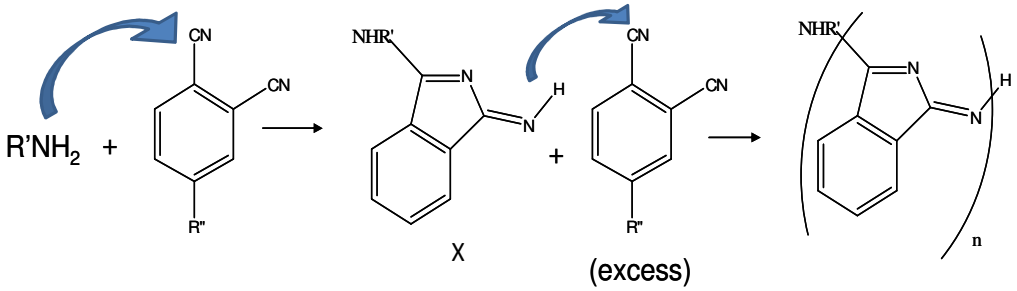


R': aromatic unit

R": 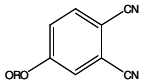


**Scheme 2-1 Formation of a poly(isoindolenine) [1].**

***Phthalocyanine:*** Several reaction schemes for the formation of phthalocyanine were proposed. Scheme 2-2 illustrates the proposed phthalocyanine formation from phthalonitrile resin by Keller and Griffith using activated copper to promote the reaction

[29]. It was proposed that phthalocyanine nucleus were formed by four divalent 3-iminoisoindoleine units, which is a highly reactive mesometic form of phthalonitrile.

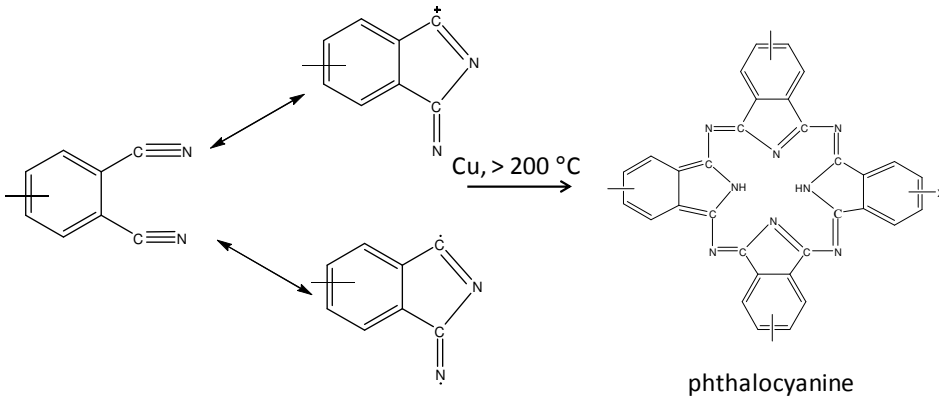


**Scheme 2-2 Proposed reaction for the formation of phthalocyanine [29].**

Tomoda et al. Described the formation of metal free phthalocyanine using alkoxide and suggested that the alkoxide anion performed a nucleophilic attack at the nitrile (C≡N) groups of phthalonitrile to form a 1-alkoxy-3-iminoisoindolenine intermediate (I) as shown in Scheme 2-3 [30]. It was speculated that the addition-elimination of four such intermediates and the subsequent reduction and cyclization led to the formation of phthalocyanine.

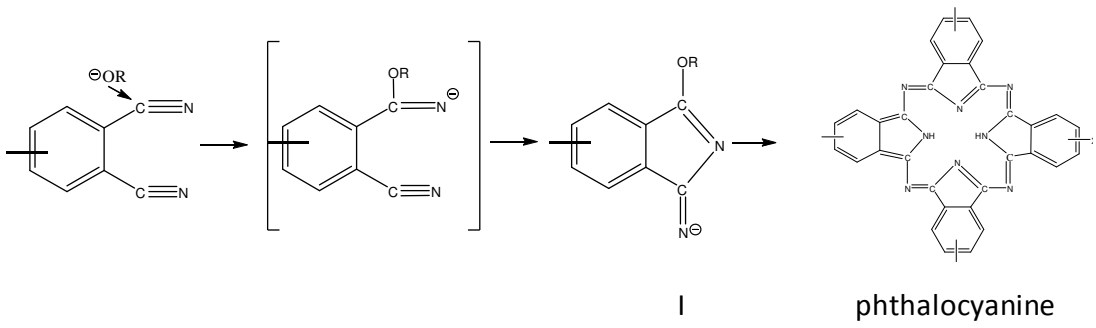


**Scheme 2-3 Proposed reaction for the formation of phthalocyanine [30].**

Snow and Griffith carried out extensive studies on the synthesis and characterization of phthalocyanine network polymer using model compounds[14]. It was suggested that the cyclotrtramerization of four phthalocyanines formed a phthalocyanine network where, ideally, bis(phthalonitrile) monomers are transformed to a phthalocyanine network polymer as illustrated in Scheme 2-4.

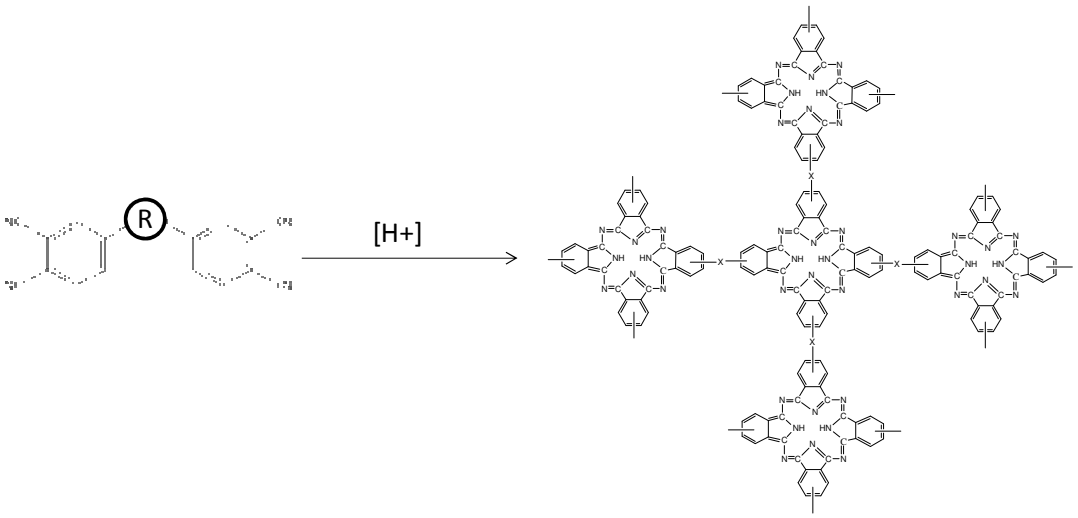


**Scheme 2-4 Formation of phthalocyanine network from bis(phthalonitrile) monomer.**

***Triazine:*** Triazine is another major product of the polymerization process and was clearly identified by the characteristic peak at 1360 $cm^{-1}$ and 1520 $cm^{-1}$ FTIR spectrum. The formation of a triazine ring was proposed by Burchill using amine as curing additive and illustrated in Scheme 2-2 [31]. According to the proposed mechanism, the formation of the amidine groups occurred via initial protonation of the cyano group nitrogen followed by nucleophilic attack by free base at the carbon. When 3 organic cyano compounds were transformed into amidine, cyclization occurred to give a triazine and eventually form polytriazine.

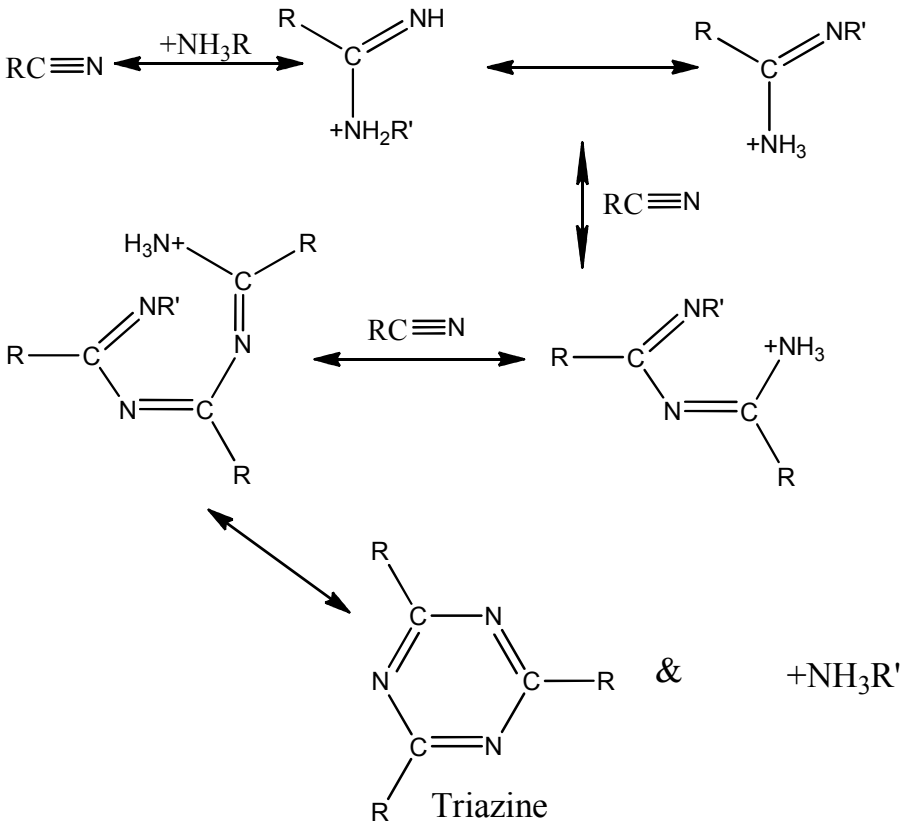


**Scheme 2-5 Formation of a triazine [29].**

## 2.2 Carbon Materials Developed from Organic Precursor

Carbon based materials hold a crucial role in most of the modern developments from electronics, catalyst carriers to biomedical devices. The great versatility of carbon is contributed by the excellent mechanical properties retention at high service temperature, the almost metal like conductivity, optical transparency, low friction, protection and resistance against chemical corrosion. Since carbon is the main constituent of organic materials, polymers with high carbon yield are commonly used as organic precursors for carbon materials development.

### 2.2.1 Methods for Producing Carbon Films

Many have reported the preparation of carbon materials in various forms, such as fiber, void free film, and macro and mesoporous films from various high carbon content precursors. Here the discussion was limited on carbon film development. There are quite a number of methods to produce carbon films on substrates, using electron gun, pulsed laser, chemical vapour, ion beam, plasma or sputtering depositions [32-37]. These methods are preferred because of the better quality films produced. The surfaces are smoother, thickness is easily controllable and the films with submicron thickness minimized film shrinkage and reduced crack formation. However, it is a must to point out that these methods are accompanied by stringent operation conditions such as high vacuum, inert environment, specific deposition parameters, high operation temperature and dangerous carbon precursors. Moreover, sophisticated and expensive equipments are needed to carry out the deposition process. Graphene is a single-atom thick two dimensional metastable sheet composed of $sp^2$ carbon that has attracted great attention due to its remarkable electronic, thermal and mechanical properties. In bottom-up approached, graphene is synthesised by a variety of methods such as chemical vapour deposition, arc discharge, epitaxial growth on SiC [38-41]. In top-down processes, graphene sheets are produced by mechanical exfoliation, direct sonication, chemical or thermal reduction and superacid dissolution of graphite or graphite derivatives [42-46]. Unfortunately, the mentioned methods for graphene production generally faced common challenges of limited sheet dimensions and scalability. On the other hand, pyrolysis of organic films coated on substrates provides a convenient way to produce carbon films. A high temperature heating chamber with inert gas protection is all that required for pyrolysis process. Among the various methods used for carbon films preparation, the ones prepared by carbonization of organic precursors are termed as “thick films” due to the

micrometer thickness. Comparing to the thin films prepared by other methods, they were inadequate in the mechanical properties such as hardness and modulus mainly caused by film shrinkage and the thermal stress being piled up during heating and cooling down. However the simplicity, low cost and scale up ability make it a more attractive method in some cases.

### 2.2.2 Organic Precursors for Carbon Materials Preparation through Pyrolysis

Thermal stability and high carbon yield upon pyrolysis are the primary requirements for organic materials to be used as precursors for carbon materials development. Phenolic resins are among one of the frequently used materials as precursor for its high flame resistance and good thermal insulation behaviour. It has a typical carbon yield about 55 % and electrical conductivity from few up to hundreds of $S/cm^{-1}$ [47-49]. Highly refined cellulose from wood was used to produce highly amorphous carbon is used by Rhim et al to observe the carbonization mechanism [50]. They have provided an extensive study on the carbon structure evolution and correlate the conversion process to five distinct electrical conducting regions. Unconventional organic precursors were also used for such application. Borlinos et al produced carbon film of polyvinylpyrrolidine through gas phase deposition [51]. Nakano successfully incorporated iodine and titanium dioxide into polyvinyl alcohol to stabilize the film for pyrolysis [52]. The carbonized composite film achieved electrical conductivity of 0.01 S/cm. Poly (p-phenylene terephthalamid) was also used but resulted with high porosity upon pyrolysis [53].

### 2.2.3 Structural Formation and Characterization of Carbon Materials

Carbon films are predominately made up of carbon and “property-modifier” such as heteroatoms like hydrogen, oxygen and nitrogen, or inorganic particles like metal oxide,

metal particles. The film properties are strongly dependant on the graphite-like ($sp^2$) and diamond-like bonds ($sp^3$) present in the system. The ternary diagram in Figure 2-1 clearly illustrates the different type of amorphous carbon consisting of hydrogen, $sp^2$ and $sp^3$ bonded carbon at various compositions [54]. Amorphous carbon consists of a significant amount of $sp^3$ bonded carbons are termed as diamond like carbons. Sputtered a-C (sputtered carbon) and ta-C (tetrahedral amorphous carbon) are forms of non-hydrogenated carbons. Sputtered a-C has more $sp^2$ bonded carbon atoms compared to ta-C which can have up to 85% $sp^3$ bonded carbon atoms as shown in the ternary phase diagram. A carbon material consists of highly disordered amorphous carbon shows properties which are distinct from one with 'perfect' polycrystalline graphite and this lead us to the structural characterization the carbon films. Since Raman bands obtained for polycrystalline graphite was correlated to information obtained from x-ray diffraction by Tuinstra and Koenig [55], Raman spectroscopy is being used extensively to analyze structural features for graphitic materials. A carbon material derived from organic material generally show the following peaks on a Raman spectrum, at ~ 1580 $cm^{-1}$ or known as the G band corresponds to an ideal graphitic lattice and is due to carbon in-plane vibration. Structural defects are reflected by D band at ~ 1350 $cm^{-1}$ with a shoulder at ~1620 $cm^{-1}$ (D′ band) [55, 56]. Normally deconvolution of the Raman spectra are needed to reveal the actual structural information for quantitative analysis of the bands, especially for materials with structural defects which caused severe band overlapping [57].

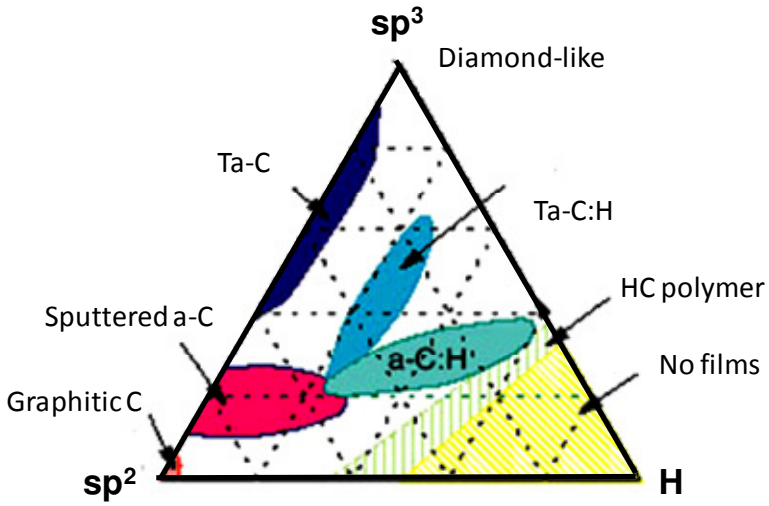


**Figure 2-1 Ternary phase diagram of amorphous carbon. $sp^3$, $sp^2$ and H at corners correspond to diamond, graphite and hydrocarbon respectively[54].**

## 2.3 Polymer Foam

Polymeric foams are expanded or cellular plastics generally consist of at least two phases, a gaseous phases existing within the solid matrix defining the voids. These versatile materials can be obtained in various forms of blocks, sheets, slabs, boards or being sprayed onto substrates as coatings, foamed in places between walls or as a core in mechanical structures. Polymer foams are traditionally used in areas where insulation, sound or impact damping and weight reductions were required. In recent years, biocompatible polymer with high porosity and interconnected pores are becoming popular choices for tissue engineering such as scaffolds or bone implants [58-60]. Polymer foams may be structurally homogeneous with uniform cellular morphology throughout or they may be structurally anisotropic. They may have an integral solid polymer skin or they may be multi-component in which the polymer skin is of different composition to the polymeric cellular core. Cartoon illustrations for different physical forms of cellular polymer are shown in Figure 2-2.

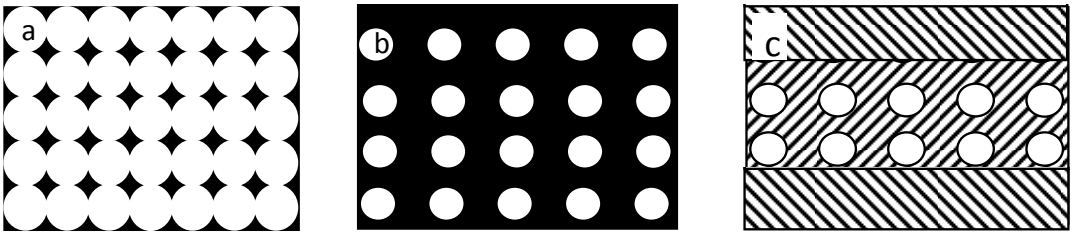


**Figure 2-2 (a) Low-density open cell foam (b) High-density closed cell foam (c) Structural foam with cellular core and integral solid skin [61].**

***Classification of polymeric foams:*** Polymer foams can be classified into rigid and flexible foams or be classified based on the composition and cell morphology. A rigid foam is defined as one in which the polymer exists in the crystalline state or, if amorphous, is below its $T_g$. Following from this, a flexible cellular polymer is a system in

which the matrix polymer is above its $T_g$. The foam cell size categorizes foams into macrocellular (>100 μm), microcellular (1-100 μm), ultramicrocellular (0.1-1 μm) and nanocellular (0.1-100 nm).

Another way of classifying polymer foam is through the connectivity of the cells. Opened cell foams contain gas bubbles that are connected to each other and formed an interconnected network. These foams are usually produced by free expansion or with cell breaking agents being added during foaming process to purposely cause cell openings. Individual cells in opened cell foams are interconnecting like in sponge and have better absorptive capability which allows the cells to be filled with whatever they are surrounded with. However, the opened cell foams are generally more inferior in mechanical performances. Closed cell foams consisted of cells which are isolated from each other by solid cell struts; a feature helps to improve the insulation, dimensional stability and prevents moisture absorption. Normally the closed cell foams have higher compressive strength and are generally denser comparing to opened cell foam[62].

### 2.3.1 Fundamental Principles of Foam Formation

Among the various ways of producing foam materials, this study focused the discussion on the most widely used method of producing foamed polymers: dispersing a gas throughout a fluid polymer phase and stabilizing the resultant foam. There are three fundamental steps involved in the method mentioned above: bubble formation, bubble growth, and bubble stabilization. In-depth understandings of the foaming principles are essential to obtain of a foam product with desirable cell structure.

***Bubble formation:*** The first step in producing foam is the formation of gas bubbles in a liquid system. Gas can be physically introduce into the system through agitation or can be the result of a specific gas-releasing reaction, such as the formation of carbon dioxide when isocyanate reacts with water in the formation of water-blown urethane foams [63]. Gas can also be generated through volatilization of a low-boiling solvent such as trichlorofluoromethane. Figure 2-3 follows the time course of the events in a gas/polymer system for bubble initiation. At zone I, the gas dissolves in the polymer melt and increase the gas concentration until above the saturation concentration ($C_s$), the system becomes supersaturate, bubble self-nucleation starts and continues as long as the gas saturation is above $C_s$ (Zone II). When the gas concentration is reduced to below self-nucleation level via bubbles formation, no new bubbles will be initiated but gas will still diffuse from the liquid into the existing bubbles causing them to grow (Zone III). The bubble growth will continue to grow till the gas concentration has been reduced to the equilibrium ($C_E$) level.

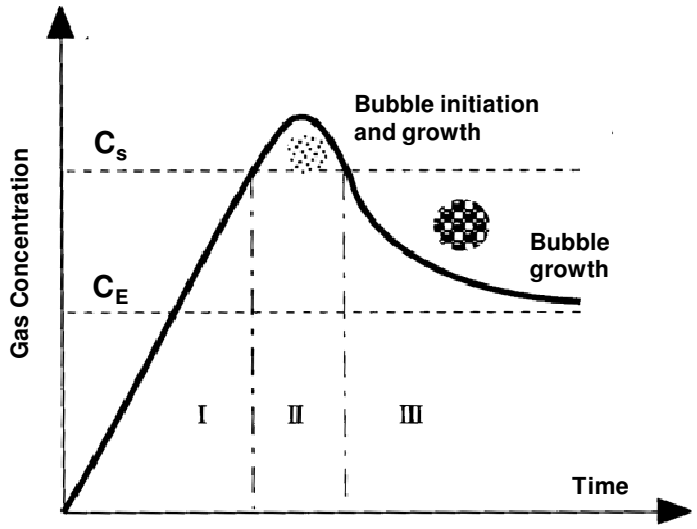


**Figure 2-3 Relationship between changes in gas concentration in a polymer melt and bubble nucleation and growth of foam cells [11].**

It is difficult to initiate bubbles by self-nucleation process because formation of bubbles in a liquid requires an increase in free energy (ΔF) of the system, as shown in Equation 2-1. Bubble formation can be made easier by lowering the surface tension at the liquid-gas interface through (i) adding nucleation agents, and (ii) increasing the temperature to reduce ΔF.

$$\Delta F = \gamma . A \qquad \textbf{Equation 2-1}$$

where γ is the surface tension of the liquid and A is the total interfacial area.

*Bubble formation due to nucleation agent addition:* The classical steady state nucleation theory is often used to qualitatively describe the number of nucleation sites ($N_i$) generated by nucleation agents [64-67]:

$$N_i = C_i f_i \exp\left(-\Delta G_{crit} / k_B\right) \qquad \textbf{Equation 2-2}$$

Here $\Delta G_{crit}$ is the critical nucleation formation energy and is related to the contact angle between gas/polymer melt/nucleation agents interface, $k_B$ is the Boltzmann factor, and T is the absolute temperature. $C_i$ is the concentration of heterogeneous nucleation sites; $f_i$ is frequency factor of gas molecules joining the nucleus. However, it has to point out that the data obtained by the theory shows a great deal of discrepancy from actual experiments because the classical theory overestimated the energy required. The nucleation formation energy is dependent on the critical nucleus size which is an inaccessible parameter during actual foaming process. The nucleation efficiency of nucleation agents is affected by the size, shape, distribution, concentration, and surface treatments of the nucleation agents being added. A general selection guideline for nucleating agents was proposed by McClurg and Leung [68, 69]:

- The nucleation agents should be able to lower the surface energy barrier needed for bubble initiation relative to homogeneous nucleation and unintentional heterogeneous nucleation caused by contaminants in the polymer matrix.
- Ideal nucleating agents should have uniform sizes, surface geometries, surface properties, and easily dispersible.
- A rugged surface as illustrated by Figure 2-4 that contain many conical crevices of small semiconical angles ( β ) is preferred.

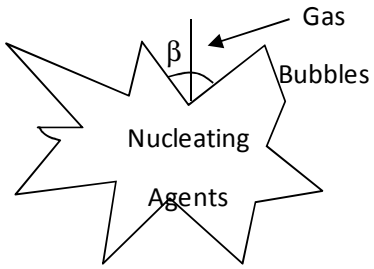


**Figure 2-4 Surface geometry of nucleating agents with rugged surface, β indicate the semiconical angle [69].**

Lee et al carried out studies to compare the nucleation efficiencies of carbon nanofibers, carbon nanotubes and exfoliated nanoclay in PS matrix [70]. The results showed that Equation 2-2 gives a much over estimation of the potential nucleation density, mainly due to the poor dispersion of the nanofillers. Among the three nanofillers being compared, nanofibers showed the highest measured cell density and the efficiency was higher than nanotubes or nanoclay by at least 4 orders. Lee et al credited the high efficiency of nanofibers to the good dispersion and low nucleation energy barrier [70]. Figure 2-5 illustrates how the reduction of critical energy is affected by the nucleants, in terms of surface property (contact angle) and particle geometry (surface curvature). In heterogeneous nucleation, the highest nucleation efficiency can only be achieved when the nucleation on the nucleant surface is energetically favoured. The minimum amount of

energy needed for nucleation is known as the critical energy, it is affected by the nucleant geometries. Here, f(*m,w*) is the energy reduction factor, which is a function of contact angle θ (between the gas and polymer and particle surface) and the relative curvature (*w*) of the nucleant surface (radius R) to the critical radius ($r_{crit}$) of the nucleated phase as shown in Equation 2-3.

$$f(m,w) = 1 + \left(\frac{1-mw}{g}\right)^3 + w^3\left[2 - 3\left(\frac{w-m}{g}\right) + \left(\frac{w-m}{g}\right)^3\right] + 3mw^2\left(\frac{w-m}{g} - 1\right) \qquad \textbf{Equation 2-3}$$

Where $m = \cos\theta$, $w = R/r_{crit}$, $r_{crit} = 2\sigma/(P_G-P_L)$, $g = (1+w^2-2mw)^{0.5}$

Qualitatively, nucleating agent with small contact angle and high surface curvature caused more effective critical energy reduction and results in higher efficiency. High nucleation efficiency will be achieved not only by choosing the right geometry and surface, but more importantly a good dispersion [66, 67, 70]. The PS/CNTs system in Figure 2-5 is used as illustration, if the CNTs are completely dispersed; the relative radius *w* is 0.2 considering that the radius of an individual tube is 0.5 nm. In that case, f is 1.8 and the nucleation energy on any single tube surface would approach the homogeneous limit, completely diminishing the benefit of heterogeneous nucleation. In PS/CNF system, the relative radius *w* is around 21 for individual CNF. With a typical contact angle of 20 ° Equation 2-3 yields a reduction factor f of 0.006

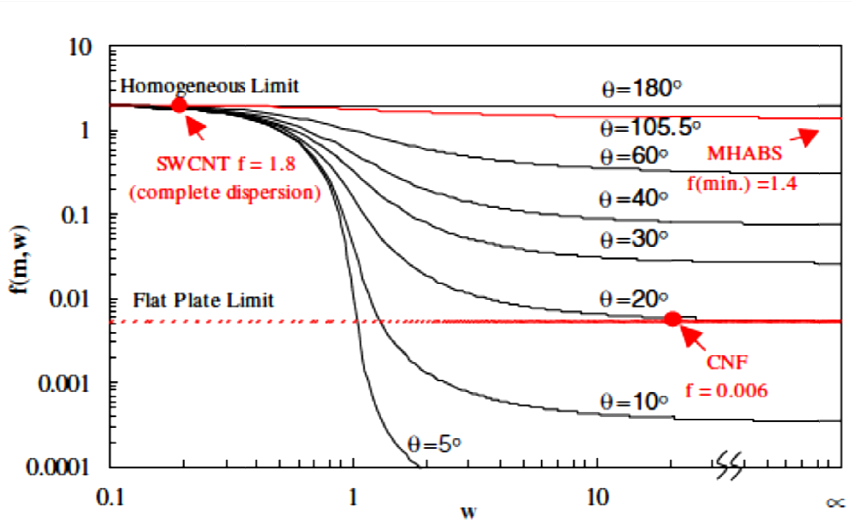


**Figure 2-5 Reduction of critical nucleation energy by nucleating agent properties. f (m,w) is a function of surface contact angle and surface curvature, w is relative radius of nucleating agent [70].**

***Bubble growth:*** Bubble once formed may grow through gas diffusion from the liquid phase into the bubbles. Based on thermodynamics, for a given volume, the system will be more stable with fewer larger cells than with many smaller cells. Hence bubble coalescence is favoured to produce larger cells to achieve system stabilization. Another driving force for bubble growth is the pressure difference established in the system. At equilibrium, gas pressure in a spherical bubble is larger than the pressure in the surrounding fluid by a difference of ΔP as explained in Equation 2-4.

$$\Delta P = \frac{2\gamma}{R} \qquad \textbf{Equation 2-4}$$

R is the radius of the bubble.

For two adjacent bubbles of radii $R_1$ and $R_2$, the pressure difference is given as:

$$\Delta P^2 = 2\gamma \left(\frac{1}{R_1} - \frac{1}{R_2}\right) \qquad \textbf{Equation 2-5}$$

From the equation one can deduce that gas will tend to diffuse from smaller bubbles (higher pressure) to the larger ones, resulting in the disappearance of the small bubbles and bigger bubbles grow further at the same time.

Gas volume from early foaming stage is small and the bubble remains spherical. As bubble volume increases, the fluid phase becomes insufficient to maintain the spherical shape and results in polyhedral shapes. As bubbles grow enough to give a low density foam, the typical shapes are dodecahedron, with many four-and five-sided membranes separating the cells [61]. Figure 2-6 gives examples for polyhedral and spherical cells.

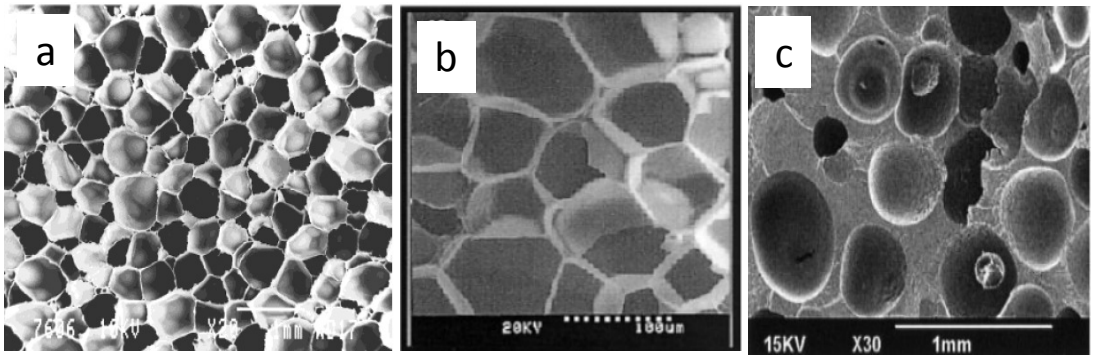


**Figure 2-6 (a) (b): Low density polyurethane and polystyrene foam showing cells in polyhedral shape, (c) high density PS foam showing rather spherical cells [71-73].**

Street et al. were among the first few who studied the growth of a gas bubble in viscous, non-Newtonian liquid with effect of heat, mass and momentum transfer taken into consideration [74]. In a real foaming system, a large numbers of bubbles grow simultaneously during foam expansion and Street's theory was inadequate to represent the phenomenon. Amon and Denson proposed a cell model based on mathematical analysis [75] to account for depletion of gas with a finite amount of liquid being stretched during bubble expansion. According to the model, the foam is divided into spherical

microscopic unit cells of equal and constant mass, each consisting of a liquid envelop and a concentric spherical gas bubble. The cell model is capable of describing important quantitative features of a real system of numerous bubbles growing in close proximity to one another. Arafmanesh and Advani conducted numerical study to simulate bubble growth in a Newtonian fluid driven by gas diffusion and the transfer momentum between the fluid and the bubbles [76]. The discussion included the predicted foam density and the experimental results and provided explanation accounted for the sources of errors. For all the theories mentioned above, it was found that the rate of bubble growth or collapse was enhanced by the elasticity of the liquid surrounding the cell.

***Bubble stabilization:*** Before solidification occurs, the stabilization process of the polymeric foams can be related to the stability of liquid foam. Many reports found related to the stability of liquid foams. By nature these foams are thermodynamically unstable; movements of the liquid cell through capillary actions and gravity further promote the collapse of the foams due to cell thinning. Bubble stabilization is generally achieved by two ways, melt viscosity increase or stabilization by adsorbed particles on foam cell surface. When the viscosity or melt strength of the liquid cell wall was increased by temperature reduction or increased chemical reaction rate, the force required to overcome pressure difference increased. This effect combats excessive liquid cell movement and hence slows down cell thinning process and stabilizes the cell structure. There have been several recent examples of foams being stabilized by particles adsorbed at air/liquid interface forming a rigid shell that protects the bubbles against coalescence [77-84].

Added particles also alter the viscosity of the polymer melt which influenced the bubble stability to a great extend. The movement or diffusion of the adsorbed particles on the

bubble surface on the other hand, jeopardized the bubble stabilization if the liquid cell membrane does not solidify on time. During cell expansion, the concentration of the adsorbed component, such as solid surfactants or reinforcement fillers changed and this change may be restored through *Marangoni effect* or *Gibbs effect*. As the particles flow from areas of high concentration (low surface tension) to low concentration, it drag along some of the underlying polymer melt and restore the film thickness, this mechanism is known as the *Marangoni effect* [61, 85].This mechanism provides a source of film elasticity and resilience. The second process is known as *Gibbs effect*, when the adsorbed component's concentration is replenished by diffusion from the interior to the surface, however this process does not restore liquid to the film and caused bubble breakage. If these two mechanisms are the only factors influencing the bubble stability, one may design a system where *Marangoni effect* dominates to make self-healing of the bubbles possible and to prevent cell coalescence and collapse

### 2.3.2 Nanofillers for Nanocomposite Foam

Nanofillers are ideal fillers to be used for nanocomposite foam development due to the nature of the foam structure. The submicron to nano sizes makes them an ideal additional component for foams because the foam cell walls are normally of micron to nano thickness especially for the low density foams. Traditionally three types of nanofillers of distinct geometries illustrated in Table 2-2 are used. 0D nanofillers has all the three dimensions in the nanometer scale, typical examples are spherical silica particles, nanocrystals, metal nanofillers and block copolymers. Nanotubes and nanofibers have two dimensions in nanoscale and the third is much larger. The last type of nanofillers has lateral dimension in the range of several hundred of nanometres to microns and nanoscale thickness.

**Table 2-2 List of different nanofillers, the geometries, and surface area to volume ratios.**

| 0 D Particulate | 1 D Tubes/Fibrous | 2D Layered Platelets |
|---|---|---|
| 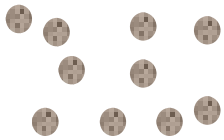 | 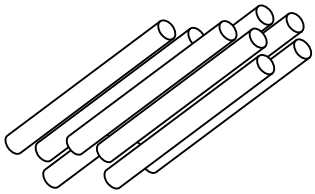 | 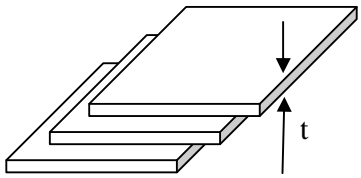  |
| 3/r | 2/r + 2/l | 2/t + 4/l |
| Silica, Ceramics, Metal particles, | Carbon Nanotubes Nanofibers | Monotmorillonite, Nanographite |

In this study, three types of nanofillers with distinct geometries and aspect ratios were shortlisted, 0D fumed silica (FS), 1D multi-walled carbon nanotubes (MWNT) and 2D expanded graphite (GH).

***Fumed Silica*** is also known as pyrogenic silica, is formed when microscopic droplets of amorphous silica are fused into highly branched chains of 0.1-0.2 μm and agglomerate into tertiary particles. The nature of the surface of the aggregates will to a large extent determine the dispersions as well as the compatibility of FS with the matrix or solvent. The siloxane and the silanol functional groups are found on the surface of the pristine fumed silica which may form hydrogen bonds with either the solvent or attach to the neighbouring aggregates during solvent dispersion process to improve the dispersion and stabilization of the nano sized particles [86]. FS aggregates has high surface to mass ratio, the typical specific surface area is between 50 $m^2/g$ and 400 $m^2/g$.

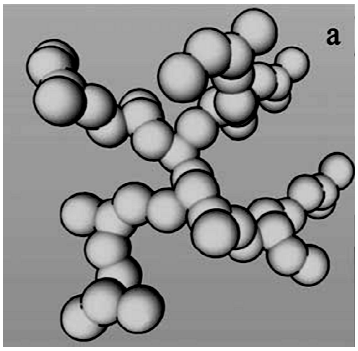


**Figure 2-7 Schematic showing typical fumed silica.**

***Carbon nanotubes:*** The coaxial arrangement of graphene sheets made up of $sp^2$ carbons provided exciting carbon tube-like nanostructures. By adjusting the synthesis conditions, carbon nanotubes can be made single wall or multi wall, Figure 2-9 shows schematics of typical single wall nanotubes, and multi-walled nanotubes with interlayer spacing ~0.34 nm. And the packing for each layer of the hexagonal carbon sheets caused the difference in conductivities. Arm-chair and 33% of the zig-zag nanotubes have continuous conducting band, the remaining of the zig-zag nanotubes are semiconductors [87, 88].

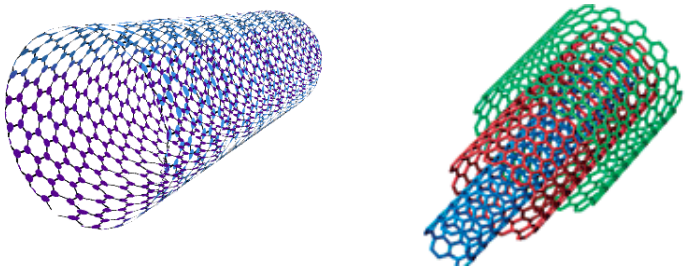

**Figure 2-8 Schematic of single- walled nanotube and multi-walled nanotube.**

***Graphite nanoplatelet***e is of 2D platelet form with covalent bonds connect the carbon atoms within the same layer, weak van de Waals forces existed between the layers of the carbon sheet. The weak inter layer forces make it possible for atoms or molecules to intercalate into the interlayer spaces of the expanded graphite. Figure 2-10 outlines one of the reported methods for expanded graphite [89-91].

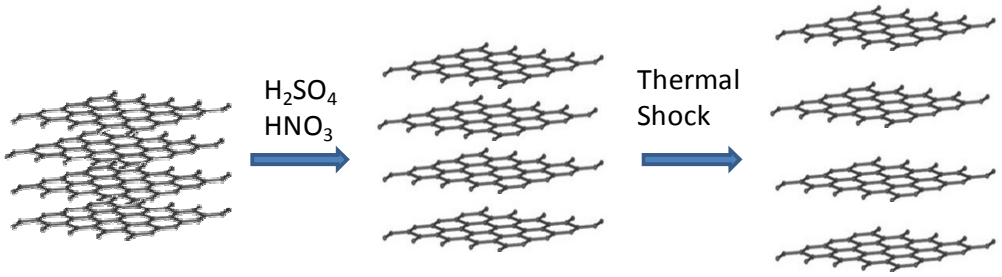


**Figure 2-9 Schematic illustration of preparing expanded graphite.**

Table 2-3 presents the unique mechanical, electrical, optical and thermal properties of CNT and graphite. The superior properties exhibited by both have generated interests and opportunities for new composites development and applications [92-97].

**Table 2-3 Theoretical and experimental properties of carbon nanotubes and graphene [93-99].**

| Properties | CNT | Graphene |
|---|---|---|
| Specific density | 0.8 g/cm$^3$ for SWNTs;<br>1.8 g/cm$^3$ for MWNTs(theoretical) | 2.26 g/cm$^3$ |
| Elastic modulus | ~1 TPa for SWNTs;<br>~0.3-1 TPa for MWNTs | 1 TPa ( in plane) |
| Strength | 50-500 GPa for SWNTs;<br>10-60 GPa for MWNTs | 130 GPa |
| Resistivity | 5-50 μΩ cm | 50 μΩ cm ( in plane) |
| Thermal expansion | Negligible(theoretical) | -1.5 x 10 $^{-6}$ |
| Thermal stability | >700 °Cm in air, 2800°C in vacuum | 450 – 650 °C in air |
| Specific surface area | 10-20 m$^2$/g | - |

### 2.3.3 Effects of Nanofillers on Foam Quality

The key in obtaining a uniform cell structure is through simultaneous nucleation of many bubbles from a polymer melt saturated with gas. The nucleating agents in foams act by initiating many bubbles simultaneously and depleted the excess gas available for bubble growth, rather than fewer larger bubbles, many small bubbles were generated. Colloidal silica, micro-expanded silica, inorganic particles are commonly used nucleating agents.

A uniform dispersion of these particles alters the polymer melt viscosity or promotes the nucleation process for the gaseous phase at the particles sites. PEEK foams were made possible by adding carbon-nanofibers [100]. Various reports were made on the improvement of morphology and cell size control for nanocomposite foams. Although the nucleation mechanism is still under investigation, it has been shown in many reports that particles functioned as nucleating agents [64, 101-103] and improved the nucleation efficiency in many nanocomposite/polymer systems at very low particle concentrations, e.g. PC/nano-silica [101], PU/SiC, PU/$TiO_2$ [104] ,PP/clay [105], PS/clay [106-108]. Figure 2-10 shows the significantly reduced cell size resulted from nanoclay addition.

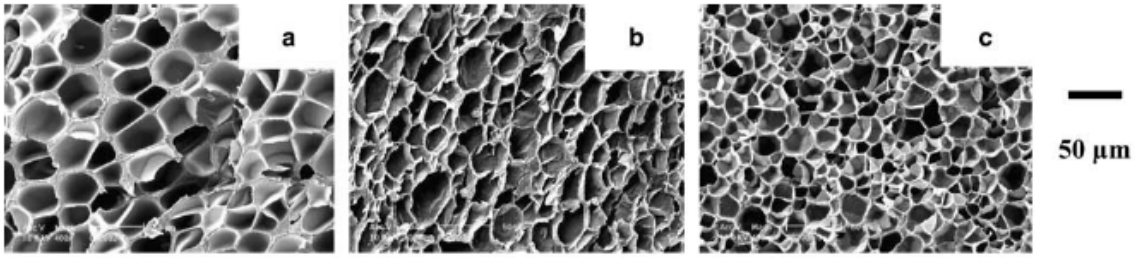


**Figure 2-10 SEI images of (a) PS foams, (b) PS/2% commercial clay, and (c) PS/5% clay produced by in-situ polymerization [70].**

### 2.3.4 Effects of Nanofillers on Foam Properties

Nanofillers are excellent choices as reinforcement for nanocomposite polymeric foams development for couple of reasons. Firstly their large surface area make them superior

candidate as reinforcement for nanocomposites. There is no lacking of literatures on improvements due to nanofillers addition in all aspects of properties for nanocomposites. Secondly, conventional fillers cannot be physically accommodated into delicate systems such as films and foams but the limitations were reduced by a great deal with the introduction of nanofillers. However the fundamental issues such as dispersion, alignment and interfacial interaction remained as the primary causes hindering nanocomposite developments where the dimensions are much smaller and the problems mentioned above are more severe. Nevertheless, much focus was still placed on nanocomposite developments due to the tremendous improvements brought along by the introduction of nanofillers.

When bubbles were being introduced into a polymer matrix for foam structure formation, properties, especially mechanical properties are inevitably weakened by the introduction of gas phases and inhomogeneous bubble distribution further elevates the problem. These sacrifices can be compensated by the addition of nanofillers such as Silica [109] ,$TiO_2$ [110], cellulose derivatives [111], carbon nanofibers [70], carbon nanotubes[112, 113], graphene [113, 114], and nanoclay [115-117] . These nanofillers improved the properties mainly by two aspects. Firstly, through improving the foam methodology, foam with well distributed cells or narrow cell size distribution has much better mechanical properties comparing to a inhomogeneous system [117]. Various reports were made on the reinforcement effects of polymeric foams, the deteriorated mechanical properties caused by the cellular structure can be compensated by the reinforcement. Wouterson reported by adding 3 wt% fiber, the tensile strength, Young's modulus and fracture toughness of epoxy syntactic foam increased by 40, 115 and 95 % respectively [118]. 10% nanofibrils increased the yield strength of amylopectin-based foams by 82 % [119]. Improvements in

compression modulus, tensile strength, Young's modulus, $T_g$ and thermal properties of nanocomposite polyimide foams were reported by Cook [120].

The thermal properties of the nanocomposite foams were also improved over the neat counterparts. The new species produced at the interlayer of nanoclay improved the thermal properties of clay/PU foam [115-117, 121]. Functionalized graphite sheets and carbon nanotubes improved the thermal stability and char yield of silicone foams arising from the strong nanofillers/polymer interactions and confinement of the polymer in the intercalated layers [113, 114].

### 2.3.5 State of the Art Foams for HT Applications

Polymer foams are being seen in everyday's life from packaging to insulation and even be found in transport and aerospace applications. However, they are seldom being used for applications where high temperature is required. Form the materials selection chart illustrated by Figure 2-11, there is no polymer foam which can be used at temperature higher than 200 ℃. Over the years researchers have been looking into this area and there are some promising findings. Comparing to thermoplastic foams, thermoset foams appeared to be more suitable for HT applications because they do not melt but turn to char by heating and the relatively better thermal resistance.

So far, there were only several reports on HT polymer foams; each with their own shortcomings. For instance, foaming of polybenzimidazoles (PBI) required post foaming treatment at temperatures above 400 ℃ [11]. The rigid polyimide (PI) foam developed by the National Aeronautics and Space Administration required tedious fabrication procedures [12]. Foams made from epoxy, polyurea, polypyrrones, and phenolic resins

were also developed, however still with limited service temperatures (< 200 °C) [7-10]. No report found on any polymeric foam which can be used at temperature higher than 200 °C for an extended period of time.

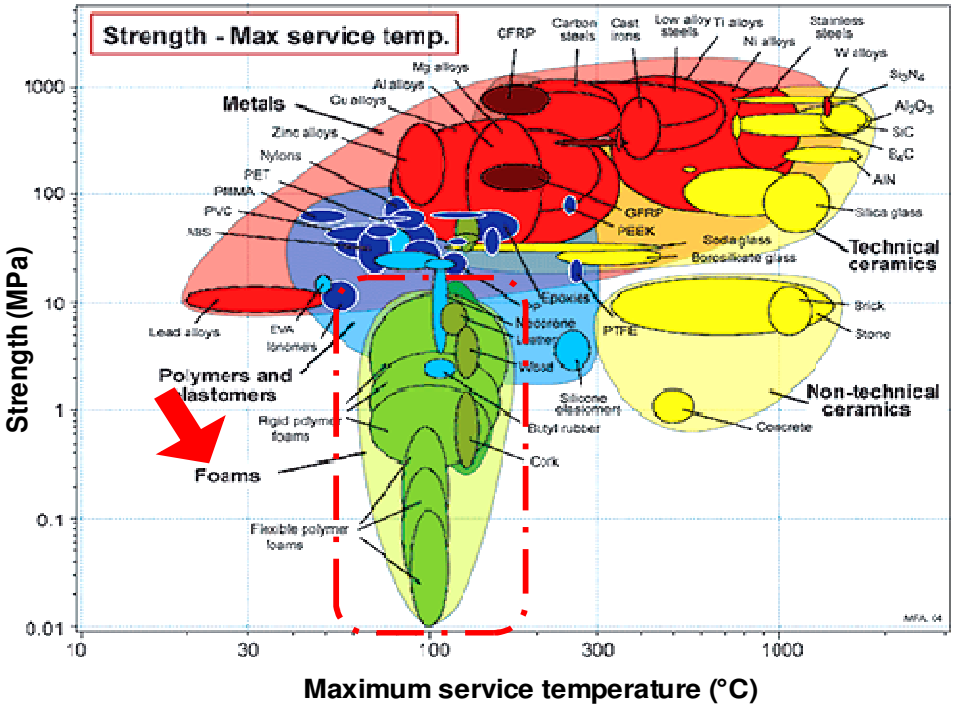


**Figure 2-11 Ashby Diagram for strength vs. maximum service temperature for materials selection[122].**

## 2.4 Blowing Agents for Polymer Foams

The structure of cellular gas-filled polymers can be formed either by foaming a polymer system or by introducing gas-filled microspheres (microballoons) into a system, or by extracting materials by a post-treatment, resulting in the formation of cells or pores. Among these, one step reactive foaming is the most generally employed method to produce thermoset cellular structure and this cannot be done without the use of blowing agents. In this research, the scope of discussion is limited to foam formation by blowing agents and discussions on syntactic foams and other foaming methods were ignored.

All types of blowing agents are being characterized by:

1. The gas number: the volume of gases being liberated by 1 g of the blowing agent per unit time (1 min) at the maximum gas liberation temperature.
2. The initial decomposition/boiling temperature.
3. The temperature range of the maximum rate of decomposition.
4. The rate and kinetics of the gas liberation, and,
5. The pressure of the foaming system developed by gas.

The above mentioned characteristics provide an approximate data and adjustments have to be made for real foam development.

### 2.4.1 Blowing Agents selection

There are various requirements to be taken into account when selecting a blowing agent.

1. The decomposition or reaction temperature must be close to the melting temperature and the hardening temperature of the polymer.
2. Gas must be liberated within a narrow temperature range.
3. Highly exothermic reaction should be avoided to prevent the polymer matrix from thermal damage.
4. The liberated gas and residual component should not have negative effect on the polymerization process of the polymer matrix.
5. The gas released should be readily dispersed and dissolved in the polymer melt.

***Inorganic blowing agents***: These are inorganic solid materials which liberate gaseous products as result of thermal decomposition. They are readily available and are produced in large scale. However they are not popular choices comparing to their organic counterparts due to the poor dispersion in polymer matrix. Consequently, the foams produced tend to have non-uniform structures.

***Organic chemical blowing agents*** (CBA): They are mostly individual solid compounds or mixtures of compounds that liberate gas as a result of chemical reaction, thermal decomposition or through interactions with other components within the formulation. CBAs can be well dispersed into the polymeric foaming compositions and can be processed with ordinary equipments. However, the residual components from incomplete decomposition may act as plasticizers and reduce the foam performances.

# 3 RESORCINOL BASED PHTHALONITRILE (RPH) RESIN: THERMAL PROPERTIES AND CARBONIZATION STUDIES

Condensation of suitable tetranitrile with aromatic diamine under appropriate conditions produced thermally stable polymers consisting of repeating macrocyclic units [1]. The general polymerization mechanisms were reviewed in Chapter 2. Snow and Griffith demonstrated the preparation of such polymers from phenoxy-, (phenylthio)-, and (phenylseleno) phthalonitrile compounds [14]. The cyclotetramerization of phthalonitrile functional groups produced phthalocyanine macrocycle structures with superior thermal and oxidative properties comparing to many high temperature resistant polymers such as BMI, polyimide and phenolic resins [1-6].

Keller reported that amine curing additive could reduce the curing time and produce more thermally stable polymer resin. Depending on the type of amine additive, a maximum of 50 ºC increase was observed for the temperature at 10 percent weight (10 wt%) loss upon heating in air [1]. Bisphenol A-linked phthalonitrile resins cured with amines have shown only 10 wt% loss at temperatures within 440 - 490 ºC [12]; exhibiting an anaerobic char yield of 75% when heated at 800 °C in nitrogen for 100 hours [14]. In this study we chose aromatic diamine as the curing additive due to its high melting point and stability at high processing temperatures.

Most investigations on this class of polymers so far focused on the effects of formulation on thermal and mechanical properties. Discussion which relates the structural formations during crosslinking to the thermal stability were lacking. In addition, little was known about the carbonization behaviour despite the superior thermal properties demonstrated

[123]. In this chapter, resorcinol based phthalonitrile (RPh) resin was used as a model study due to the relatively lower processing temperature. Systematic studies were carried out aiming to give an in-depth understanding of the intrinsic factors that affect the thermal decomposition of phthalonitrile resins. Investigations were carried out to establish a correlation between the structures and thermal properties to be used as a guideline for future applications. Systematically studies on the carbonization and characterization of phthalonitrile based polymer will be carried out and discussed.

## 3.1 Experimental

### 3.1.1 Materials

***Synthesis of 1,3-bis(3,4-dicyanophenoxy)benzene:*** Laboratory synthesised bis(3,4-dicyanophenoxy)benzene, a resorcinol-based phthalonitrile (RPh) was used in the study. Resorcinol, anhydrous potassium carbonate, anhydrous dimethyl sulfoxide (DMSO) were purchased from Sigma Aldrich and used as received. 4-nitrophthalonitrile was generously provided by DSTA National Laboratory, Singapore, purchased from Tee Hai Chemicals and used as received.

RPh was prepared following a modified procedure described by Keller et al [5]. Resorcinol, 4-nitrophthalonitrile and pulverized anhydrous potassium carbonate, at molar ratio of 1:2:3 were added into a 150 ml, three-neck round bottom flask equipped with magnetic stirring device was added. The mixture was stirred for 24 hrs in inert environment at room temperature in DMSO solvent before poured slowly into dilute hydrochloric acid solution. The obtained pale yellow precipitate i.e. resorcinol-based phthalonitrile monomer (RPh) was filtered by vacuum-assisted filtration and washed with deionized water till the pH of the filtrate became 7. The crude product was washed with

diethyl ether and dried under vacuum at 100 °C. Further purification was carried out by re-crystallization of the crude product from acetonitrile for characterization.

### 3.1.2 RPh polymerization and carbonization

***Prepolymer Preparation:*** Prepolymer was prepared by adding 1, 4-bis (4-aminophenoxy) benzene (APB), purchased from Tokyo Chemical Industry and used as received, to the molten RPh monomer in round bottom flask with $N_2$ purging to prevent oxidation of amine. The mixture was quenched after 10 to 15 minutes of stirring. This process made use of the fast initial reaction between amine and nitrile groups which tied the amine onto the resin. A typical characteristic of the reaction is the formation of a dark green coloured product which is soluble in common solvents such as acetone, chloroform and DMF.

***Curing Procedures:*** The molten prepolymer was degassed at 200 ºC inside the vacuum oven. A progressive curing profile was employed for all samples throughout the studies in Chapter 3. Postcuring above 300 °C was carried out in an inert environment to minimize oxidation.

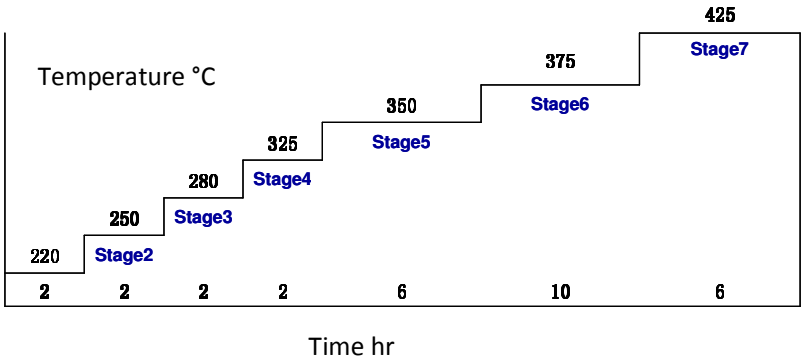


**Figure 3-1 Progressive curing profile used for curing and postcuring of RPh polymer.**

***Carbonization:*** RPh prepolymer was dissolved in DMF and spin coated at 3000 rpm on quartz substrates. The film was then placed inside vacuum oven to remove excess solvent.

Further polymerization was carefully controlled to prevent film shrinkage. Cured films were postcured following the progressive curing schedule shown in Figure 3-1 before carbonization. Carbonization was done at the temperature of 500 °C to 1000 °C inside a Lindberg tube furnace from Thermo Scientific with continuous purging of argon.

### 3.1.3 Characterization

***Differential Scanning Calorimetry (DSC)*** DSC was used for curing studies of the RPh/APB system. APB (1 – 50 mol %) and RPh monomer were mixed and sealed in hermetic pans. Dynamic heating scans were carried out using DSC Q10, TA Instruments, from 50 °C to 350 °C at heating rates of 5, 10, 15 and 20 °C/min under flowing $N_2$ (40 ml/min).

***Fourier Transform Infra-red (FTIR)*** APB and RPh were dried inside vacuum oven to minimize the effects of moisture on curing. APB was solution-mixed with monomer in acetone before casting on potassium bromide pellet and the solvent dried off. The prepared film was cured in $N_2$ following the curing profile illustrated in Figure 3-1 and was took out periodically for FTIR scans from 400-4000 $cm^{-1}$ with spectral resolution of 4 $cm^{-1}$ using Perkin Elmer Instruments Spectrum GX FTIR spectrometer at room temperature.

***Thermal Gravimetric Analysis (TGA)*** Thermal decomposition kinetics studies were carried out using Thermogravimetric Analyzer Q500, TA Instruments. Dynamic heating from 50 to 850°C was performed to study degradation at heating rate of 5, 10, 15 and 20 ºC $min^{-1}$ in $N_2$ and air (60 ml/min). The sample size was typically about 10 to 15 mg.

***Dynamic Mechanical Analysis (DMA)*** Storage moduli (E′) and loss moduli (E″) were recorded with DMA Q800, TA Instruments. Single cantilever geometry was used for temperature sweep from 50 ºC to 450 ºC at 1 Hz and heating rate of 3 ºC/min in air.

Samples were cast in a mold with dimensions of 30 mm x 15 mm x 3 mm. They were degassed at 200 ºC before curing and polished for analysis.

***Atomic Force Microscope (AFM)*** Dimension 3100 AFM (Veeco, CA) was used to image films under ambient conditions in tapping mode with a silicon tip (resonant frequency of 320 kHz, spring constant of 42 N/m) at a scanning rate of 1 Hz and sample lines of 512.

***Scanning Electron Microscope (SEM)*** A JEOL 6360 SEM was used for morphology examination. Samples were sputter coated with platinum before observation.

***Raman Spectroscopy*** Raman spectroscopy provides a standard non-destructive way to characterize carbon materials ranging from amorphous to crystalline carbons. Confocal microscopy from Witec alpha-300 was used to characterize the carbonized RPh samples. The specifications are: excitation laser wavelength 488nm (2.54eV), gratings 300, 600, 1800 Grooves/mm, vacuum sealed thermoelectric (TE) cooled CCD. He-Ne laser beam was illuminated on samples through a 100X objective lens with a spot size of ~0.5 μm and the laser power was tuned below 1 mw to avoid heating or destroying of samples. The Si peak at 520.6 $cm^{-1}$ was used as a reference for wavenumber calibration. Detailed scans were carried out from 400 to 3500 $cm^{-1}$ under ambient conditions.

***Nanoindentation*** Hysitron TI 950 TriboIndenter$^{TM}$ equipped with diamond Berkovich probe was used to perform nanoindentation tests. All tests were performed in displacement controlled feedback mode to a peak displacement of 300 nm. A load sequence of 20 s loading, 5 s holding and 20 s unloading was used. 4 indentations were taken for each sample for average reading.

***Four-point Probe*** Sheet resistivity of the carbonized films was measured on quartz stage using four point probe from Keithley. The operating current was 4.35 x $10^{-3}$ A.

## 3.2 Results and Discussion

### 3.2.1 Synthesis of RPh

The monomer was synthesized according to Scheme 3-1 (yield ~ 80%) through nucleophilic displacement of a nitrile-substituent from 4-nitrophthalonitrile by the dialkaline salt generated from resorcinol. The reaction took place at room temperature in anhydrous polar aprotic solvent e.g. DMSO and DMAC with the presence of base. Bases that can be used include sodium carbonate, potassium carbonate, sodium hydroxide, and potassium hydroxide. When using a strong base such as sodium hydroxide or potassium hydroxide, water would be formed as a by-product during the formation, should be removed by azeotropic distillation to prevent possible reaction of the cynao groups.

FTIR spectra of 4-nitrophthalonitrile and RPh were used to monitor the synthesis reaction. The disappearance of the nitro group absorption peaks at 1538cm$^{-1}$ and 1355cm$^{-1}$ indicated the completion of the reaction. The final pale yellow powder has a melting point of 186 C° and is soluble in common organic polar solvent such as acetone, dimethylformamide, and tetrahydrofuran.

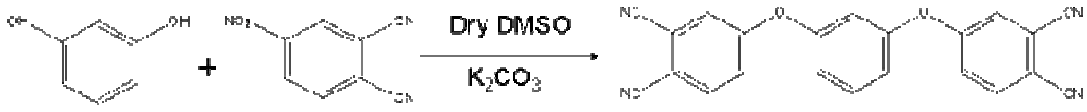


**Scheme 3-1 Synthesis scheme of 1, 3-bis (3, 4-dicyanophenoxy) benzene.**

### 3.2.2 Thermal Properties of RPh

In this study, the onset of degradation is defined as the temperature at 5% weight loss ($T_{5wt\%}$), percentage of residue/char yields at 600 ºC ($T_{600}$) and 800 ºC ($T_{800}$) were

determined as a function of extent of postcuring and ABP content. The apparent activation energy of degradation ($E_d$) was determined by analyzing temperature at the maximum rate of weight loss ($T_{max}$) from differential TGA (DTGA) curves.

***Effect of Postcuring:*** RPh with 5 mol% APB was used to study the effects of postcuring on the thermal stability. Figure 3-2 shows TGA and DTGA curves of RPh/APB systems at each curing stage. DTGA curves revealed two degradation stages at around 350 ºC and 470 ºC at earlier postcuring stages (Stage 1-3). The degradation at 350 ºC could be attributed to incomplete crosslinking network formation which started to diminish with progressive postcuring. The main degradation peak shifted from 470 ºC to 530 ºC with progressive curing. Substantial reduction of the maximum degradation rate (lowered peak intensity) was also observed from Figure 3-2(b), an indication of a more thermally stable system.

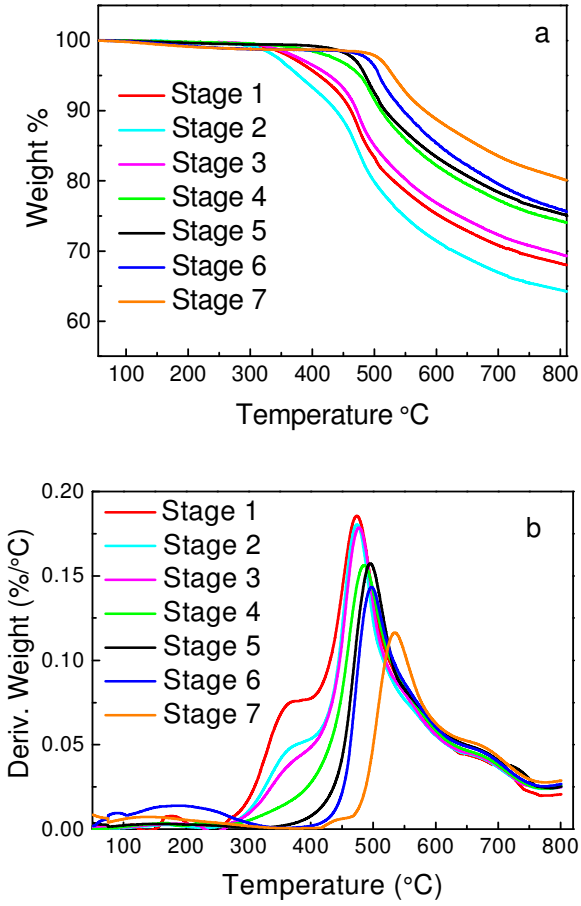


**Figure 3-2 (a) TGA and (b) DTGA curves of RPh with 5 mol% APB underwent progressive curing. Tests were done in flowing $N_2$, heating rate of 10 °C/min.**

The corresponding thermal parameters temperature at maximum weight loss ($T_{max}$) determined from DTGA graphs, temperature at 5wt% weight loss ($T_{5wt\%}$), weight retention/char yield at 600 °C($T_{600}$) and weight retention/char yield at 800 °C ($T_{800}$) at different stages of postcuring were summarized in Table 3-1. $T_{max}$ increased by 55 °C (473 to 528 °C), while more strikingly $T_{5wt\%}$ increased by 147 °C (378 to 525 °C). The extraordinarily high char yields at high temperatures are definitely worth noting. For example, after 6 stages of postcuring, $T_{600}$ approached 88% and $T_{800}$ was as high as 79% in $N_2$. This high thermal stability was probably attributed to the increased crosslinking

density and the formation of macrocyclic structures, the detailed structural formation will be discussed in the later part of this chapter.

**Table 3-1 The thermogravimetrical parameters obtained from TGA analysis done in $N_2$ corresponding to different curing stages. $T_g$ was determined from the tan δ peak from storage modulus versus temperature curves in Figure 3-3.**

| Curing Stages | $T_{max}$ (ºC) | Temperature at 5wt% Loss (ºC) | Char yield at 600ºC (%) | Char yield at 800ºC (%) | $T_g$ ( ºC) |
|---|---|---|---|---|---|
| Stage 1 | 473 | 378 | 75.3 | 64.4 | -* |
| Stage 2 | 472 | 411 | 71.4 | 68.2 | -* |
| Stage 3 | 476 | 428 | 76.9 | 69.6 | 225 |
| Stage 4 | 495 | 477 | 83.2 | 74.3 | 255 |
| Stage 5 | 498 | 486 | 83.4 | 75.3 | 326 |
| Stage 6 | 511 | 508 | 85.4 | 75.9 | 360 |
| Stage 7 | 528 | 525 | 87.9 | 79.4 | > 450** |

*** $T_g$ measurements were not carried out. ** No $T_g$ was detected below 450ºC.**

Changes of storage modulus (E′) and loss modulus (E″) upon heating were measured by DMA (Figure 3-3 a and b) which provided evidence of the increased crosslinking density during post curing. More crosslinked system can be evidenced from the gradual increase of E′ through progressive curing as well as the shift of the glassy to rubbery state transitions to higher temperature. It should be highlighted that after 7 stages of postcuring, the polymer exhibited mechanical properties corresponding entirely to the glassy state over the entire testing temperature up to 450 ºC in air. Figure 3-3(a) shows significant broadening of the transition region and plateauing at higher level. Signifying the formation of a highly crosslinked polymer with molecular weight heterogeneity which exhibiting an exceptionally high glass transition temperature ($T_g$). This was further proven by the shifting of E″ peak to higher temperature and the reduced E″ values as post curing proceeded.

Temperature at tan δ peak is often taken as the $T_g$ of a polymer, whereas the peak intensity and breadth are sensitive to the amplitude and homogeneity of the macromolecular chains respectively [124]. The increasing crosslinking density greatly restricted the chain motions and reduced the damping capability, causing the peak intensity to decrease from 0.7 to 0.05. It was observed from Figure 3-3 (c) that the significant increase in tan δ half width after stage 5 indicated the non-uniform distribution of molecular chains inside the system. The above observations led to the conclusion that postcuring enhanced the crosslinking density in the cured polymer network. It is hypothesized that the final cured system consisted of linear and macrocyclic molecular chains with very different chain length and molecular weight.

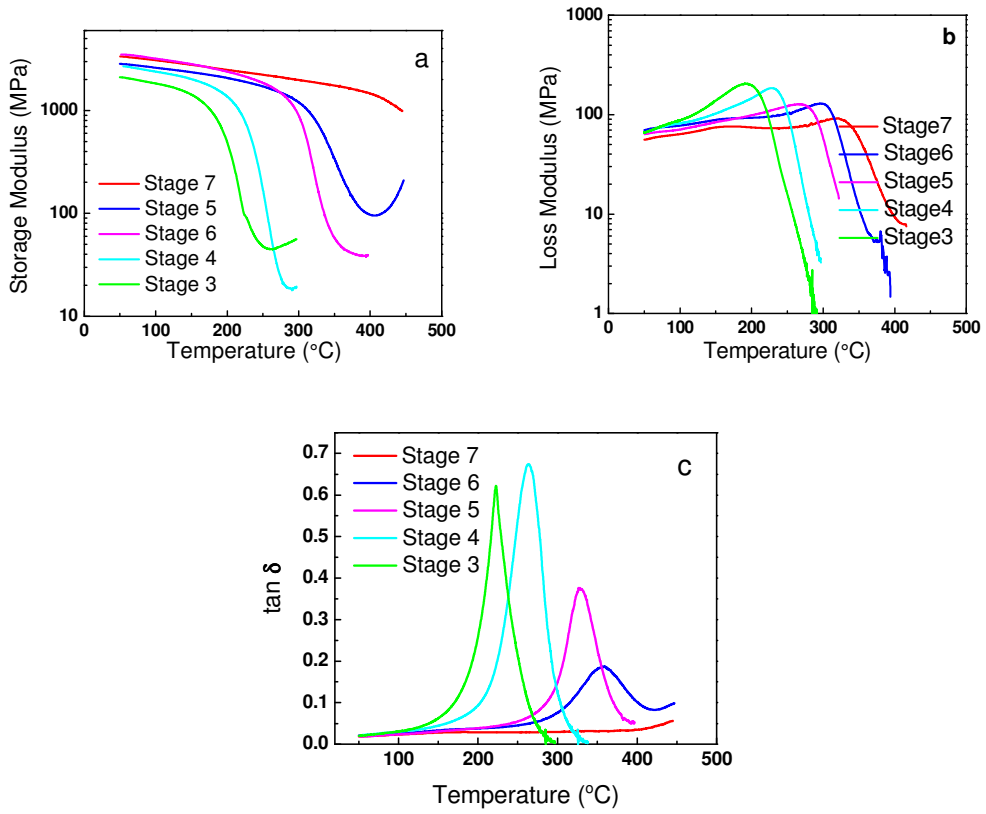


**Figure 3-3 (a)Storage modulus (b)loss modulus and (c) tan δ of RPh/APB polymer at different curing stages (5 mol% APB).**

***Effects of APB content:*** Table 3-2 summarized the values of $T_{5wt\%}$ and char yield for systems with APB content ranging from 0 – 20 mol % tested in $N_2$ and air at heating rate of 10 ºC $min^{-1}$.

The kinetics of curing was analysed using the established Kissenger model which does not require prior knowledge of the reaction mechanism[125]. For thermoset curing, the maximum reaction rate $(d\alpha/dt)_{max,}$ occurred when $d(d\alpha/dt)/dt$ is zero. The activation energy ($E_a$) for curing were obtained from Equation 3-1 and the values were summarized in Table 3-3 (details on kinetics studies were attached in the Appendix I).

$$ln\left(qT_{peak}^{\ 2}\right) = ln\left(\frac{AR}{E_a}\right) + \left(\frac{1}{T_{peak}}\right)\left(\frac{E_a}{R}\right) \qquad \textbf{Equation 3-1}$$

where $T_{peak}$ is the peak exotherm temperature, q is the constant heating rate, and R is the universal gas constant. The value of $E_a$ can be obtained from the slope of the plot $\ln(q/T_{peak}^{2})$ versus $1/T_{peak}$.

The apparent decomposition activation energy ($E_d$) was determined by the Kissenger method[125] illustrated by Equation3-2. The values were obtained from the plot of $ln(\alpha/T_{max})$ versus $1000/T_{max}$.

$$ln\frac{\alpha}{T_{max}^{\ 2}} = \ln\left(\frac{nRAW_{max}^{\ n-1}}{E_a}\right) - \frac{E_d}{RT_{max}} \qquad \textbf{Equation 3-2}$$

in which α is the heating rate, $T_{max}$ is the temperature at the maximum rate of weight loss, $n$ is the apparent reaction order, $R$ is the universal gas constant and $W_{max}$ is the residual weight at maximum rate of weight loss. Average $T_{max}$ values of repeated TGA runs were used for calculation (details on kinetics studies were attached in the Appendix II).

**Table 3-2 The thermogravimetric parameters corresponding to cured RPh/APB resin systems at a heating rate of 10 ºC/min in $N_2$ and air.**

| mol% APB | Temperature at 5 wt % Loss | | Char Yield at 600ºC (wt %) | | Char yield at 800ºC (wt %) | |
|---|---|---|---|---|---|---|
| | $N_2$ | Air | $N_2$ | Air | $N_2$ | Air |
| 0 | 553 | 520 | 89.5 | 84.9 | 80.0 | 38.7 |
| 2 | 527 | 517 | 87.9 | 80.2 | 79.9 | 29.3 |
| 5 | 525 | 520 | 87.9 | 80.2 | 79.4 | 19.5 |
| 10 | 534 | 520 | 88.9 | 80.5 | 80.4 | 29.4 |
| 20 | 522 | 511 | 88.8 | 74.6 | 80.6 | 18.4 |

**Table 3-3 Activation energy for curing ($E_a$) and activation energy for thermal decomposition ($E_d$) corresponding to cured RPh/APB resin.**

| mol% APB | | 0 | 2 | 5 | 10 | 20 |
|---|---|---|---|---|---|---|
| $E_a$ (kJ/mol) | | - | 49.1 | 63.9 | 87.1 | 98.2 |
| $E_d$ (kJ/mol) | $N_2$ | 326.6 | 237.5 | 212.1 | 221.5 | 232.6 |
| | $R^{2*}$ | 0.9996 | 0.9992 | 0.9866 | 0.9963 | 0.9976 |
| | Air | 175 | 82.4 | 83.0 | 83.3 | 82.6 |

*** $R^2$: linear fit regression coefficient**

The 'neat' resin exhibited advantages in terms of onset degradation temperature, char yield and activation energy for thermal decomposition ($E_d$) over resins containing APB, however the long curing time made it a less favourable choice and hence ignored. The data in Table 3-3 further corroborated the superior thermal and thermo-oxidative stabilities which are rarely observed in other high temperature resistant thermosets mentioned in Chapter 2. $T_{5wt\%}$ of the systems were found to be between 520 and 534 °C when tested in $N_2$. Onset decomposition temperature was maintained within 511 - 520 °C when tested in air. Furthermore, the char yields were approaching 90% and 80% at 600 °C and 800 °C respectively. Even when tested in air, the resin has an average char yield

of nearly 80% at 600 °C. Only under severe conditions, i.e. 800 °C in air, char yield was reduced to below 30%. The activation energy for curing ($E_a$) served as a clear indication of the different structural formations during curing and should lead to different thermal stabilities. But the results shown to be otherwise, increasing the concentration of APB in this case did not seem to have any significant effect on the thermal decomposition behaviour and contradicted the finding by Keller [1].

### 3.2.3 Structural Formation during Curing and the Relationship to Thermal Properties

The changes of IR absorbance associated with nitrile (C≡N) absorption at 2230 $cm^{-1}$ and several other bands (phthalocyanine at 1008 $cm^{-1}$, triazine at 1530 $cm^{-1}$ and 1360 $cm^{-1}$) were investigated to study the effect of ABP content on structural formation during curing. Reaction between phthalonitrile and curing additives is expected to produce a complex macromolecule as mixture as shown in Scheme 3-2 based on the type and quantity being added.

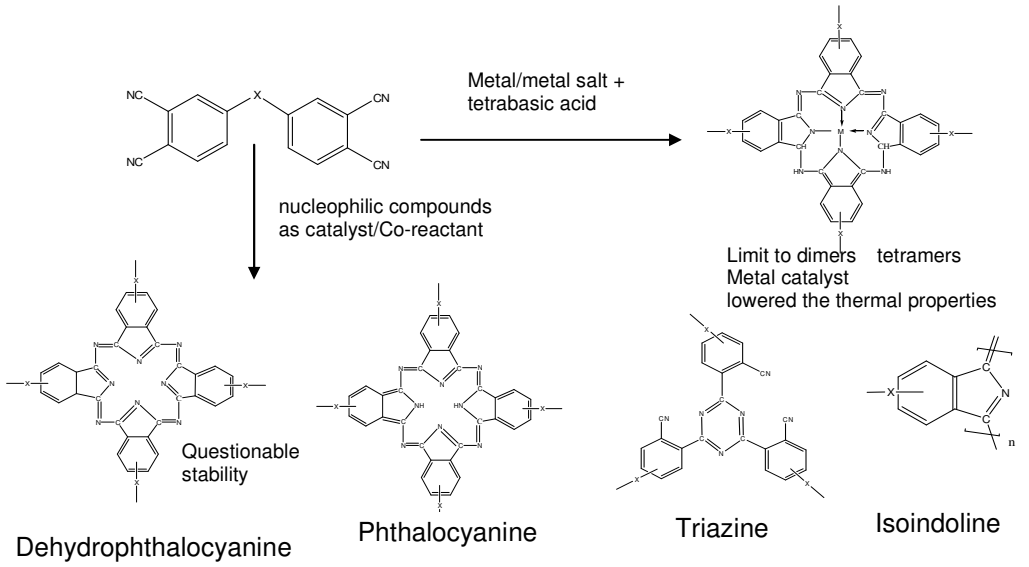


**Scheme 3-2 The possible structures formed during polymerization of phthalonitrile monomers with different types of curing additives.**

FTIR spectra of RPh with 0, 2, 5, 10 and 20 mol% of APB were presented in Figure 3-4. After curing at 220 ºC for 2 hours, IR absorbance peaks appeared at 1520 $cm^{-1}$ and 1360 $cm^{-1}$, and 1008 $cm^{-1}$ for all the RPh/APB systems, indicating the formation of triazine and phthalocyanine IR respectively [14]. In fact, the formation of triazine was observed as early as 30 minutes after curing at 220 ºC. IR absorbance attributed to phthalocyanine formation only started to appear after about 2 hours of curing at 220 ºC. The phenomenon shows that APB favours the triazine formation. By increasing the APB content, other species such as cyclic imide groups (1725 $cm^{-1}$) and linear isoindolenine (1620 $cm^{-1}$) were also observed. This has further proven that higher APB content initiates a more complex curing system which required higher $E_a$ (Table 3-3) to support the curing reactions. Without APB, there was no sign of any peaks mentioned appearing after 2 hours of curing at 220 ºC; in fact, they were only observed after at least 72 hours of curing.

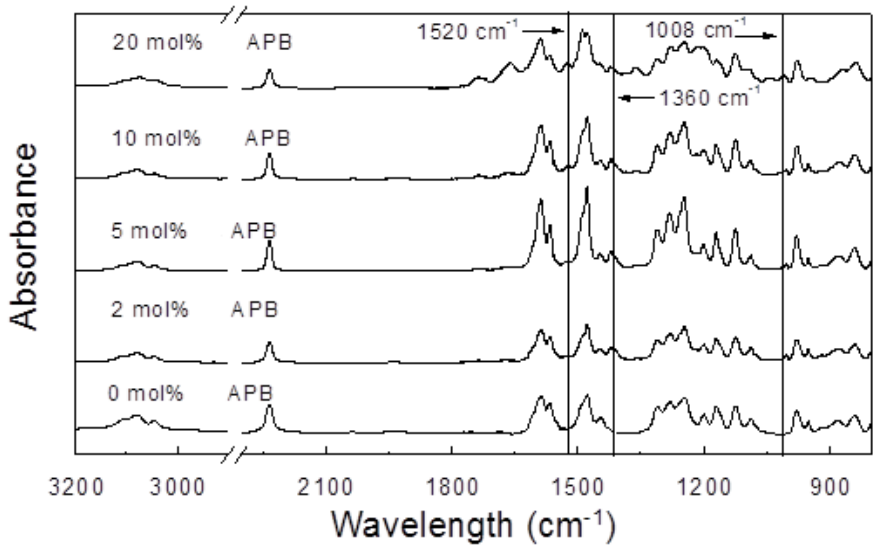


**Figure 3-4 FTIR spectra of RPh with 0, 2, 5, 10 and 20 mol% of APB as curing additive after curing at 220ºC for 2 hours.**

Attempts were made to quantify the percentage of conversion for C≡N groups and the appearances of triazine and phthalocyanine groups as a function of amine content. The IR absorption peak at 1600 $cm^{-1}$ attributed to aromatic structure vibration was selected as the reference band at which normalization was done. The corrected intensity was then used for conversion (α) calculation using Equation 3-3.

$$\alpha = \frac{I_{(x)t}/I_{(ref)t}}{I_{(x)0}/I_{(ref)0}} \qquad \textbf{Equation 3-3}$$

where $I_{(ref)\,0}$ , $I_{(ref)t}$ are the intensities for the reference peak at time **0** and **t** respectively.

where $I_{(x)\,0}$ , $I_{(x)t}$ are the intensities for the specific peaks at time **0** and **t** respectively.

The intensity change of C≡N peak (2230 $cm^{-1}$) at each curing stage was monitored and the degree of conversion was calculated and presented in Figure 3-6 for resins with 5 and 20 mol% of APB (Figure 3-5). At 20 mol% of APB, C≡N consumption occurred rapidly between Stages 1 and 4 and started to level off after that, the conversion rate was much reduced for the 5 mol% APB system. Despite the rate increase, the additive did not improve the degree of conversion; about 35% of unreacted C≡N groups for both systems remained after seven stages of postcuring. Further conversion appeared to be unlikely due steric hindrance and high degree of network interlocking. The more rapid conversion at early postcuring stages with 20 mol% APB (Figure 3-7) was due to the simultaneous formation of isoindolenine, triazine and phthalocyanine that consumed more C≡N functional groups.

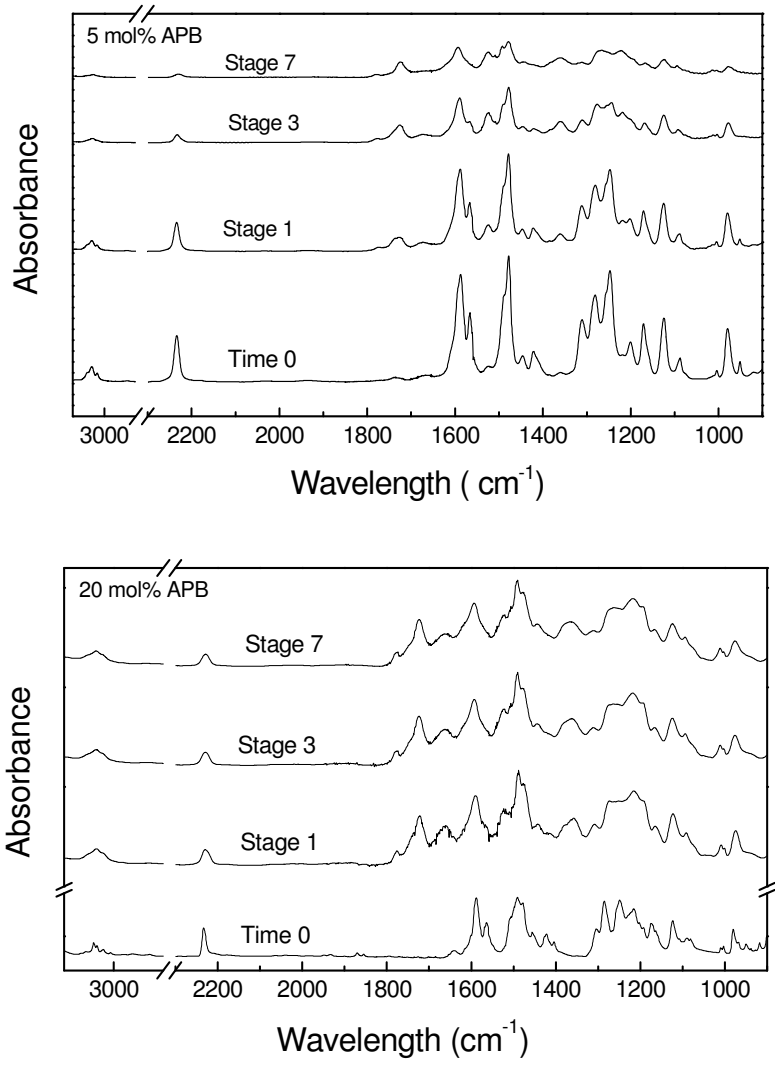


**Figure 3-5 FTIR spectra of RPh with 5 mol% APB and 20 mol% APB at different curing stages.**

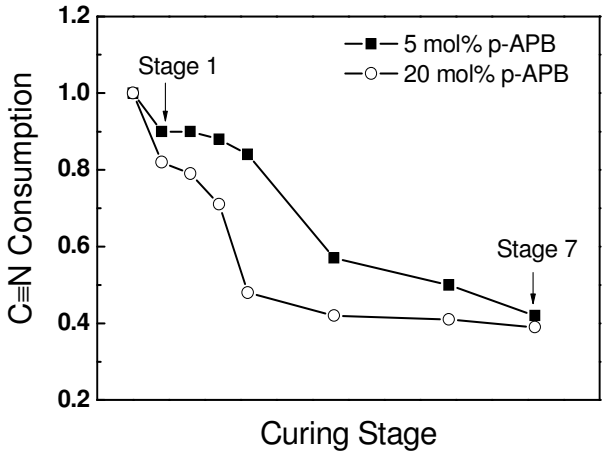


**Figure 3-6 Conversion of C≡N group as a function of curing and postcuring stages.**

Appearance of triazine and phthalocyanine were also monitored by the intensity changes based on Equation 3-1. It is important to point out that α is used to indicate the formation instead of consumption. $I_{(x)0}$ was the IR absorption peak intensity taken at the time when triazine or phthalocyanine was first being observed through FTIR scans. Comparisons in Figure 3-7 show that for systems with 5 mol% APB, the relative peak intensity for triazine was about four times more than that of the phthalocyanine. At 20 mol% APB, the relative peak intensities for both species were similar. The decrease in triazine content may be due to the formation of cyclic imide and isoindolenine at the expense of triazine and phthalonitrile.

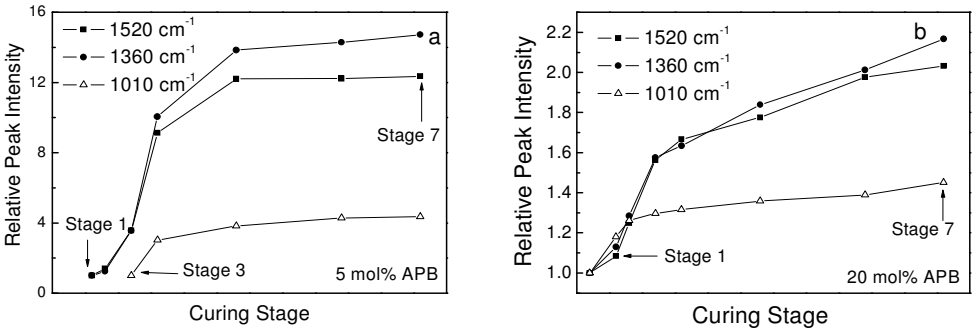


**Figure 3-7 Relative peak intensity for triazine (1520 $cm^{-1}$ and 1360 $cm^{-1}$) and phthalocyanine (1010 $cm^{-1}$) with (a) 5 mol% APB and (b) 20 mol% APB.**

By monitoring C≡N functional group conversion and the structural formation during curing by FTIR, different type and amount of macrostructures existing in different systems could be observed. Naturally, different thermal properties would be expected; however, thermogravimetric parameters presented in Table 3-2 showed that all RPh/APB systems demonstrated similar performance despite the large APB quantity variations. Scheme 3-3 provides a simple graphical illustration showing linear polyisoindolenine chain entering the cavities created by polyphthalocyanine and polytriazine. The existence of polyisoindolenine and cyclic imide groups would have led to poorer performance being less heat resistant, however, the results shown to be otherwise. It was reported before that the linkage between the reacting phthalonitrile would produce cavities of different sizes between the phthalocyanine and triazine units [3, 14]. The linear structure might have entered the cavities and resulting in a densely packed structure that is thermally resistant.

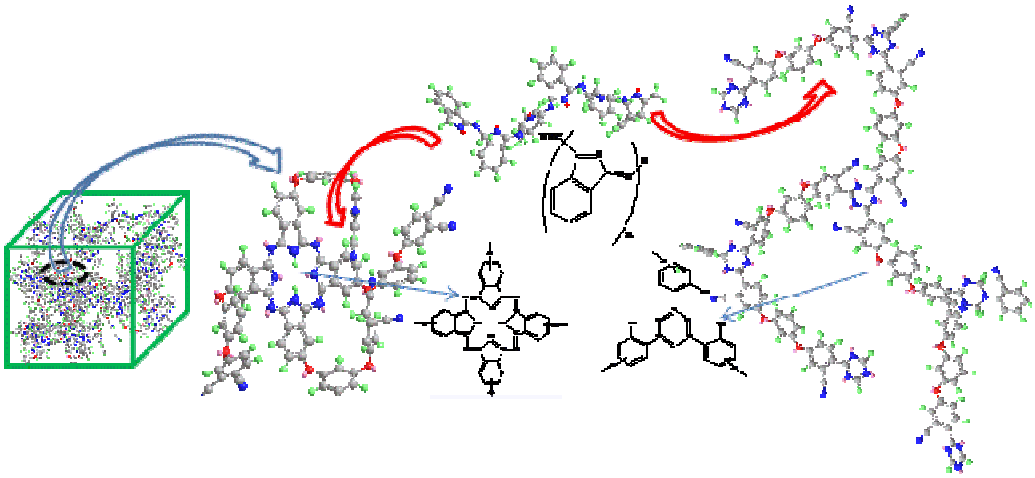

**Scheme 3-3 Schematic diagram showing linear polyisoindolenine chain entering the cavities created by polyphthalocyanine and polytriazine.**

Sulphuric acid is a solvent for monomeric phthalocyanine and many polymeric phthalocyanine [13, 126]. RPh resin was immersed in both cold and hot concentrated sulphuric acid aimed to isolate the phthalocyanine formed for quantitative analysis; however both were unable to dissolve the cured resin. Nevertheless, the insoluble nature could serve as an evidence for the significant degree of crosslink obtained during curing. Snow mentioned that as the crosslinking density approaching maximum, the structure should have a thermal stability far above that of monomeric phthalocyanine which was later further supported by Achar [126]. Achar reported TGA data showing phthalocyanine polymer undergo weight loss around (500-525 °C), 150 °C above monomeric phthalocyanine. Hence although no detailed quantitative analysis was carried out, the hypothesis made on the formation of a highly crosslinked system was supported by the insolubility in concentrated sulphuric acid and TGA.

### 3.2.4 Development of Carbon Materials using RPh Precursor

The exceptionally high char yield in both inert environment and air made RPh an ideal candidate for carbon materials such as carbon-carbon composite. RPh prepolymer can be easily dissolved in common solvent, e.g. DMF or acetone and spin-coated onto quartz substrates. The film thickness can be easily controlled by the prepolymer concentration and spin-coating speed.

***Morphology***

Herein is the first reported use of RPh as precursor for carbon film development through carbonization. The carbonization was carried out in Argon gas to minimize oxidation. The resultant morphologies were observed using SEM and AFM. SEM images in Figure 3-8 revealed voids inside the film grew larger as temperature increase and eventually formed an interconnecting network that is permeable to carbonization gases. Nevertheless, it is worth highlighting that the voids observed were less than 500 nm and no crack was observed even after carbonization at 1000 °C.

Topography of the films at each carbonization temperature was examined by AFM. AFM images in Figure 3-9 show that the polymer surface remained smooth up to 800 °C with surface roughness around 0.5 nm. In fact mirror-like surfaces were observed upon visual inspection. Voids started to appear on the surface and within the films at 800 °C. The carbonization process caused film shrinkage and escape of the decomposed volatiles which resulted in new voids formation and enlargement of the voids already existed since the initial polymerization stage. The voids grew as carbonization process proceeded via two possible routes: (i) the existing voids were further enlarged by thermal decomposition

of the neighbouring network and (ii) smaller voids collapsed during film shrinkage formed comparatively larger pores.

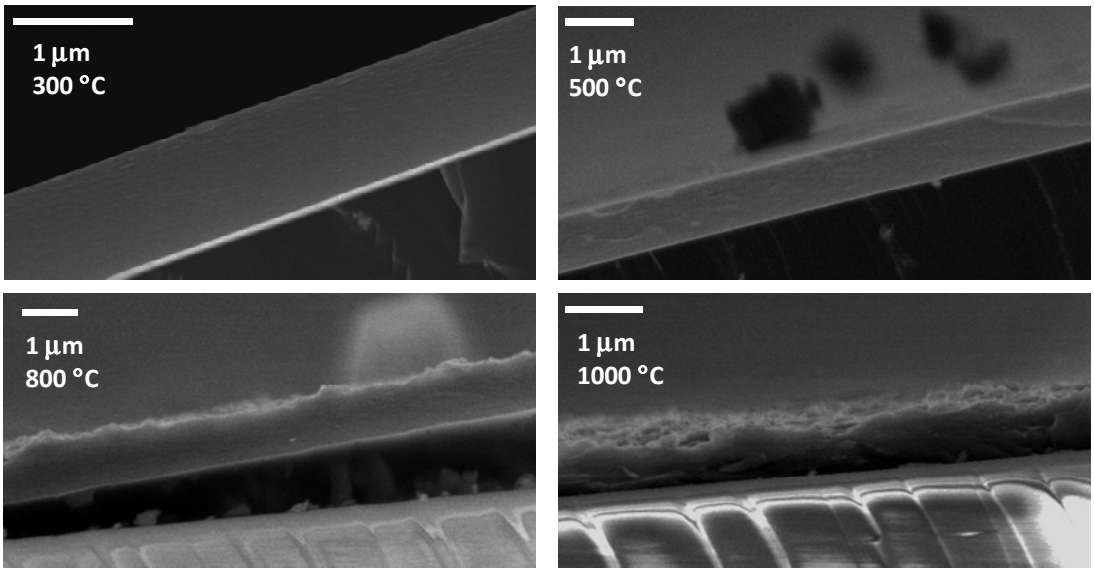


**Figure 3-8 SEI images of cross sections of carbonized films at 300, 500, 800 and 1000 °C.**

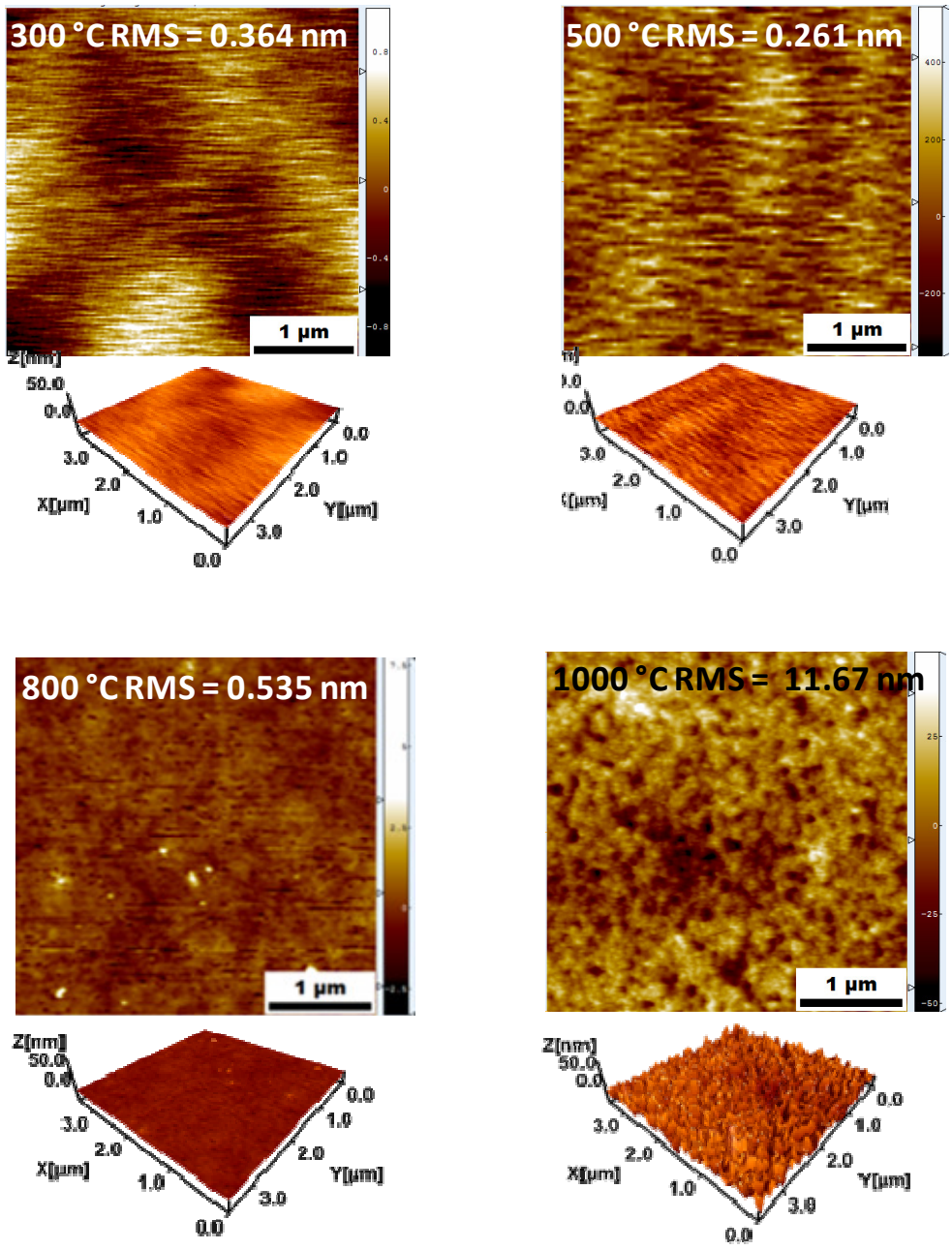


**Figure 3-9 AFM images of the surface morphologies of the films carbonized at 300, 500, 800 and 1000 °C.RMS is surface roughness in root mean square.**

***Mechanical Properties***

Mechanical integrity of carbon films is an important consideration for practical applications. A Hysitron TI 950 TriboIndenter™ was used to perform nanoindentation tests on five film samples carbonized at different temperatures in Ar. The Young's modulus and hardness obtained provide good indication for mechanical properties of the films. Young's modulus was obtained by Equation3-4:

$$\frac{1}{E_r} = \frac{1-v_i^2}{E_i} + \frac{1-v_s^2}{E_s} \qquad \textbf{Equation 3-4}$$

*v* and E represent Poisson ratio and Young's modulus, subscript $i$ and s refer to the indenter and the specimen respectively. The diamond indenter tip has $E_i$ and $\nu_i$ values of 1140 GPa and 0.07. Poisson's ratio of the specimen, $\nu_s$, is taken as 0.3.

Table 3-5 shows the hardness and modulus of the carbonized films in Ar. The highest hardness and modulus were obtained at 900 °C; the values are comparable and in some case, superior to the carbonized films obtained from other organic precursors [48, 127]. Heat treatment greatly improved the system's crosslinking process and greatly enhanced the hardness and Young's modulus when the temperature was raised from 300 °C to 700 °C. The mechanical properties continued to increase till 900 °C. It was expected that the uncarbonized RPh films show lower hardness and modulus because the polymer film was relatively softer. The improved mechanical properties were attributed to the improved crosslinking density and formation of carbon structures. Further heating at 1000 °C caused the hardness and modulus to drop. It was reported that porous structures are known to be detrimental to film mechanical properties [128] and void formation was observed in the treated films after 800 °C. At 1000 °C, the effects of porosity

overwhelmed the effects of high crosslinking density and dominated the mechanical performance and caused the drop.

**Table 3-4 Mechanical properties of RPh films carbonized in Argon gas.**

| Sample | Hardness (GPa) | Reduced Modulus (GPa) | Young's Modulus (GPa) |
|---|---|---|---|
| 300 °C | 0.973±0.02 | 6.25 | 5.7 |
| 700 °C | 2.99±0.03 | 23.49 | 21.4 |
| 800 °C | 3.87±0.09 | 30.68 | 27.9 |
| 900 °C | 5.06±0.03 | 48.13 | 43.8 |
| 1000 °C | 3.33±0.04 | 25.19 | 22.9 |

***Electrical Conductivity and Microstructures Evolution***

The electrical conductivity of the carbonized films was characterized using four point probe and presented in Table 3-5. The film was driven from insulating to conducting region and the greatest increment was observed at 800 °C before the bulk conductivity began to level off. The pyrolysis threshold of this material could be roughly estimated at 800 °C at which the conducting carbonaceous islands grew into a continuous network. The bulk conductivity obtained was 87.1 S/cm after heat treated at 1000 °C for 20 minutes. The voids do not show any negative impact on the electrical behavior. Although this value is a few orders of magnitude lower than carbon nanotubes or graphite [129], but it is comparable to some carbon film obtained from organic precursor [130-132]. Our carbon films should be suitable for certain electrical applications since some of the films mentioned in the literature were used as sensors or electrode materials.

The only study on the electrical property of phthalonitrile based polymer after heat treatment was reported by Walton et al in 1985 and they proposed that the conductivity

was contributed by the conjugate aromatic structures [133]. However, the author does not agree with the proposition because the high treatment temperature (> 700 °C) could have possibly destroyed the organic structures. In the literatures, the electrical conductivity gained through carbonization for polymeric were often credited to the graphitic species. Raman spectroscopy was used to further study the structural formation and changes for the carbonized RPh to elucidate the conduction mechanism. Figure 3-10 shows the Raman spectra of RPh films carbonized at temperature ranging from 600 – 1000 °C. Two bands centered at 1350 and 1590 $cm^{-1}$, characteristic graphitic structure was observed for all the carbonized films. The band centered at 1580 $cm^{-1}$ corresponds to G-band and was always observed with single crystal graphite, resulting from the in-plane vibration of the $sp^2$ crystallite carbon. The increasing density indicated the formation of more crystalline clusters from $sp^2$ carbon atoms since all carbons in the polymeric phthalocyanine and triazine structures are $sp^2$ hybridized. The band at 1360 $cm^{-1}$ indicates the presence of amorphous carbon arised from the $sp^2$ carbon in-plane vibration existing inside the structure imperfections and impurities [55, 134]. About 35 – 38 % of C≡N groups (Figures 3-6) were unreacted even after completing all the postcuring processes. The nitrogen rich regions later act as defects in the system and originated the formation of amorphous carbonaceous region denoted as D-band. Tuinstra and Keoning had explicitly demonstrated that $I_D/I_G$ ratio could be used for carbon domain size ($L_a$) in nm determination using Equation 3-4. This was made possible based on the facts that (a) G-band absorption can be used as an indication for the ordered graphite crystals and (b) D-band measurements are equivalent to the surface of carbons present at the graphitic plane edge.

$$\boldsymbol{L_a = 4.35 \times \frac{I_G}{I_D}} \text{ [nm]} \qquad \textbf{Equation 3-5}$$

The peak intensities were used to calculate band area ratio and the carbon cluster domain sizes were presented in Table 3-6. A slight increase was observed in the band area ratio from 600 – 700 °C before a consistent decrease was observed for both parameters. Further carbonization promoted the conversion of disordered $sp^2$ carbon into ordered crystallites and as a result, $L_a$ size increased. The growing crystallites contributed positively to the electrical conductivity of the film. Drastic increase would be observed when a continuous network was formed; in this case, this phenomenon happened at 800 °C. It can be expected that the RPh films reached critical percolation threshold at 800 °C, after which the increment levelled off.

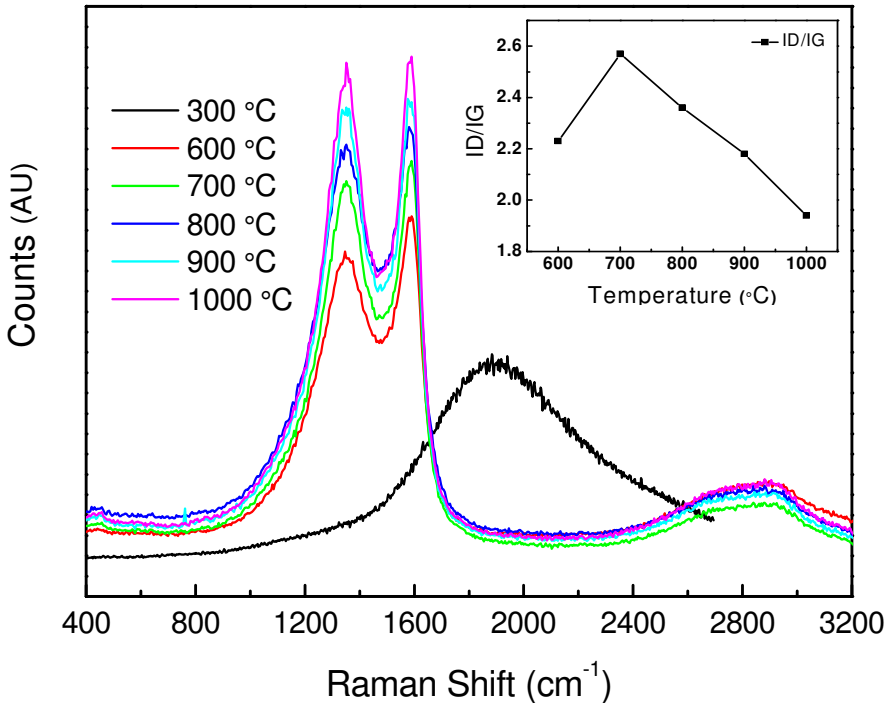


**Figure 3-10 Raman Spectra of RPh films carbonized at different temperature obtained at room temperature. Inset shows $I_D/I_G$ ratio.**

***The height intensities in this diagram were arbitrary because the spectrum intensity corresponding to the uncarbonized film due to fluorescence was 100 fold more than the carbonized film, hence was scaled down for illustration purpose.**

**Table 3-5 Conductivity, integrated area ratio of $I_D/I_G$ and the corresponding $L_a$ domain size.**

| Treatment Temp. (°C) | 300 | 600 | 700 | 800 | 900 | 1000 |
|---|---|---|---|---|---|---|
| Conductivity (S/cm) | - | 0.00085 | 0.0033 | 2.7 | 18.3 | 87.1 |
| $I_D/I_G$ | - | 2.23 | 2.57 | 2.36 | 2.18 | 1.94 |
| $L_a$ (nm) | - | -* | 1.76 | 1.92 | 2.08 | 2.34 |

*** $L_a$ at temperature below 600 °C was ignored, Equation 3-3 was inapplicable to the highly amorphous carbon film .**

Based on the evolution of electrical and microstructures, it is postulate that the final carbonized RPh film is made up of a continuous conductive network (crystalline $sp^2$) embedded in a disordered matrix consisting of amorphous $sp^2$ and $sp^3$ carbons. The conductive clusters grew with the increasing carbonization temperature and eventually joined to form a conducting network.

## 3.3 Summary

Insights to the understanding of the factors responsible for the superior thermal properties of phthalonitrile based resins were obtained using TGA, DSC an FTIR. Postcuring was essential to attain the high thermal properties, the on-set degradation was observed at temperature above 520 °C and no $T_g$ was detected up to 450 °C through proper postcuring treatments. Contrary to what has been reported by Keller, the thermal properties were independent of the APB curing additive. FTIR spectra postulated the formation of less thermally stable linear structure formation when APB content was increased to 25 wt%, a less thermally stable resin was expected, however, the results showed that APB did not cause significant change in the thermal properties. The observation was due to the formation of thermally stable macrostructures and the trapping of linear chains inside the cavities created by the aromatic heterocyclic macrostructures creating a densely packed

system. Kinetics of thermal decomposition and curing of the cured RPh/APB systems were studied and further supported the hypothesis.

The exceptionally high percentage of weight retention or char yield obtained in nitrogen (~90 % at 600 °C and ~80% at 800 °C) made the development of carbon based materials through carbonization of RPh precursor possible. Sophisticated apparatus, stringent fabrication conditions and complex carbons source were eliminated. The film produced on quartz substrate was smooth and maintained its mechanical integrity after carbonization, which was not often observed from most organic precursors. The hardness and modulus were comparable or even superior comparing to carbon films prepared by similar methods using organic precursors such as PAN, epoxy and pitch. Pyrolysis of RPh films produced conducting carbonaceous islands which eventually joined to form a continuous electrically conducting network with the conductivity being sufficient for electronic applications.

# 4 PREPRATATION AND PROPERTIES OF RPH FOAM

Polymer foams are attractive materials to both industry and academic research due to their chemical inertness, superior acoustic properties, strength-to-weight ratio, and ease of being fabricated into various forms. The growing needs in replacing traditional metal foams e.g. aluminium foams with polymeric foams drives the development of rigid and thermally stable polymeric foams. The HT foams, while matches the service temperature of aluminium foams (300 °C), aims to take advantage of the low density and chemical resistance. Nevertheless, the vision is hindered by deterioration of mechanical properties when exposed to heat. The stringent requirements eliminate the majority of the polymeric candidates due to their low service temperatures. So far, there were only several reports on HT polymer foams; each with their own shortcomings. For instance, foaming of polybenzimidazoles (PBI) required temperatures above 400 °C [11], rigid polyimide (PI) foam developed by the National Aeronautics and Space Administration required tedious fabrication procedures [12]. Foams made from epoxy, polyurea, polypyrrones, and phenolic resins were also developed, however still with limited service temperature [7-10].

Based on the study discussed in Chapter 3, RPh has demonstrated excellent thermal stability that matches or even surpasses that of PBI or PI [156,157], and was shortlisted as the polymer matrix for HT foam preparation due to its relatively lower processing temperature. All of the investigations carried out on phthalonitrile polymer so far focused on formulation and bulk properties as composites. RPh foam has never been reported. In terms of polymer foaming, especially for thermosets, establishing a system which

matches the polymer viscosity profile to the gas liberation process is critical for successful foam development. To the contrary of the past research which aimed to prolong the processing time, this new area requires gelation within minutes since most of the gas foaming agents liberate gas within a relatively short time frame. The long curing time, lack of understanding on rheological behaviour, curing mechanism and crosslinking kinetics of RPh matrix posed challenges for foam materials processing.

In this chapter, the focus was placed on the establishment of an effective foaming method through synchronization of polymer viscosity profile and gas liberation from CBA. The viscosity profile of RPh was systematically investigated as a function of resin formulation and processing conditions. Gelation time was reduced from tens of minutes to minutes through proper curing additive and temperature selection. To further justify the HT performance, the thermal and mechanical properties were determined after thermal aging. The methodology and understandings gained in this part of the work are used as a prerequisite for the development of nanocomposite foam as discussed in Chapter 5.

## 4.1 Experimental Procedures

### 4.1.1 Chemical Blowing Agents (CBA) Studies

A laboratory-built set-up as illustrated in Figure 4-1 was used to study the gas liberation number. Gas liberation number was defined as the amount of gas liberated from 1 g of CBA at a fixed temperature, unit, $cm^3/g$. 1 g of CBA was sealed in glass container and immersed in pre-heated silicone oil bath. Gas liberated due to thermal decomposition under isothermal heating was collected and measured in the measuring cylinder. TGA was used to study the decomposition process at heating rates of 5, 10, 15 and 20 °C/min in air at 190, 200, 210 and 220 °C respectively.

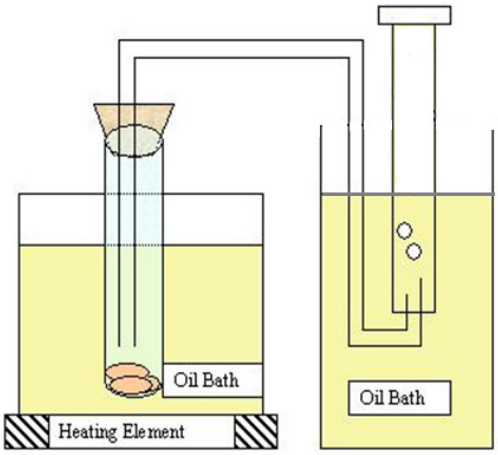


**Figure 4-1 Schematic showing the experimental set up for determination of gas liberation number of gas forming agents.**

### 4.1.2 Viscosity of Polymer Melt

Viscosity of the polymer melt was obtained using Anton Paar Physica MCR501 equipped with precision heat control chamber. Cone and plate with diameter 50 mm was used. The viscosity was obtained as a function of temperature at steady shear rate of 1/s.

### 4.1.3 Theoretical Calculations

***The amount of CBA to be used:*** The amount of CBA to be used for foaming was determined based on the gas liberation number. $N_2$ and $NH_3$ released during thermal decomposition would be first dissolved in the monomer melt and later on initiated the growth of bubble or foam cells. Theoretical calculation was carried out before the actual foaming process.

$$\text{Volume of gas required } (V_g) = \text{Mold volume} - M_f/\rho_f \qquad \textbf{Equation 4-1}$$

$$\text{CBA required} = V_g/\ (\text{Gas liberation Number}) \qquad \textbf{Equation 4-2}$$

$M_f$ and $\rho_f$ are mass and density of the foam in the mold respectively.

***Average cell diameter (D)***: The average cell diameter is larger than the circular segment observed from scanning electron microscope (SEM), because the cells are randomly

truncated at the plane of the specimen fracture surface. D was determined according to Equation 4-3, by assuming that the foam consists of randomly distributed cells.

$$\mathbf{D} = \frac{\mathbf{d}}{\pi/4} \qquad \textbf{Equation 4-3}$$

d is the measured diameter in the micrographs obtained by SEM, 150 – 200 cells were used to obtain average D.

***Bubble nucleation number/Cell density ($N_o$):*** the number of bubbles nucleated per cubic centimetre of the foams is given by:

$$N_o = \frac{N_f}{1 - V_f} \qquad \textbf{Equation 4-4}$$

where $V_f$ is the void fraction and can be estimated by

$$\mathbf{V_f} = \mathbf{1} - \frac{\rho_f}{\rho_p} \qquad \textbf{Equation 4-5}$$

The bubble count obtained from SEM micrograph is used to calculate $N_f$:

$$\mathbf{N_f} = \left(\frac{\mathbf{nM^2}}{\mathbf{A}}\right)^{3/2} \qquad \textbf{Equation 4-6}$$

where n is the number of bubbles in the micrograph, A is the area of the micrograph, and M is the magnification factor.

***Foaming grade ($F_G$)*** is determined by the foam density.

$$\mathbf{F_g} = \frac{1-\rho_f}{\rho_p} \cdot \mathbf{100\%} \qquad \textbf{Equation 4-7}$$

$\rho_f$ and $\rho_p$ are densities of the foam and bulk polymer respectively.

### 4.1.4 Foaming Process

RPh foams were developed by a one-step foaming process as illustrated by Scheme 4-1. CBA was mixed with the prepolymer and sealed in aluminium mold. The mold was heated for foam formation. The gas released from thermal decomposition would dissolve in the polymer melt and initiate bubble formation once the saturation concentration for

self nucleation has reached. The bubbles then grew by gas diffusion, coalescence and eventually stabilized by the crosslinking polymer.

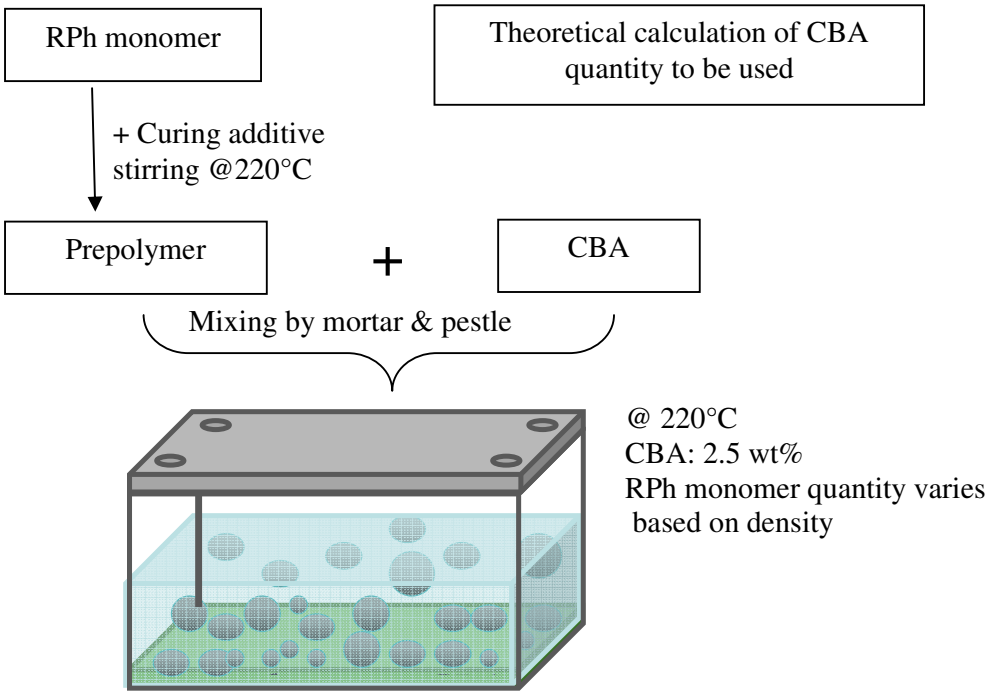


**Scheme 4-1 Diagram illustrating the one-step foaming process.**

### 4.1.5 Characterizations

***Morphology***: The porous structure was examined using JEOL 6360 SEM. Cross sections of the rigid foams were fractured perpendicular to the foaming direction. The specimens were coated with gold before observation.

***Thermal properties:*** Thermal properties were studied using TGA Q500, TA Instruments. Dynamic heating from 50 to 850°C at heating rate of 10 °C/min was performed in flowing nitrogen or air at flow rate of 40 ml/min. The sample size was typically of 10 to 15 mg.

***Mechanical properties:*** Compression strength was obtained by Instron 5567. Samples were cut into dimensions of 25 x 25 x 12.5 $mm^3$ using a precision diamond cutter.

Compression was done with 30 kN load cell with a cross head speed of 0.5 mm/min till 80% strain. All mechanical tests in this report were performed in the rise direction of the foam.

## 4.2 Results and Discussion

### 4.2.1 RPh Foam Preparation

A balance between viscosity and gas evolution is necessary to obtain stable foam with the highest possible foam volume. This is particularly important in thermoset systems which involve simultaneous polymerization of the liquid component and gas liberation from CBA. For a system with rapid viscosity increase from fast polymerization, the gas evolution may cease before the desired foam volume is reached, especially for low-density foams. On the other hand, if the increase in viscosity is too slow, foam stabilization may take longer time than desired and result in foam collapse.

#### *4.2.1.1 Foaming Condition Determination*

An ideal foaming system consists of a polymer with gelation time that coincides with the time when rapid gas liberation occurs; hence the solidifying polymer will be able to 'trap' the gas bubbles inside the matrix. CBA characterization was carried out and established the viscosity profile of RPh polymer melt at different temperature. The two parameters were then correlated to achieve a balanced system for proper foam fabrication.

A suitable CBA was shortlisted among the potential physical and chemical blowing agents chosen for foam development in this study. Further characterizations were carried out to better understand the thermal decomposition. Figure 4-2 shows the amount of gas liberated from CBA is temperature dependant. Below 200 °C, incomplete degradation of CBA liberated insufficient amount of gas to be dissolved in the polymer melt. This

reduced the gas concentration in the polymer melt and hindered bubble formation. Lower gas concentration also slowed down bubble growth because of the small pressure difference. Figure 4-3 shows that under isothermal heating, low heating rate delayed the decomposition process and would lead to foaming failure if the delay was longer than the gelation time of the polymer melt.

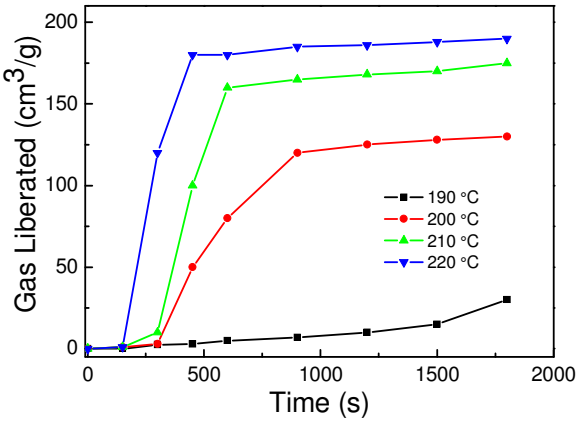


**Figure 4-2 TGA thermographs showing CBA thermal decomposition under isothermal heating.**

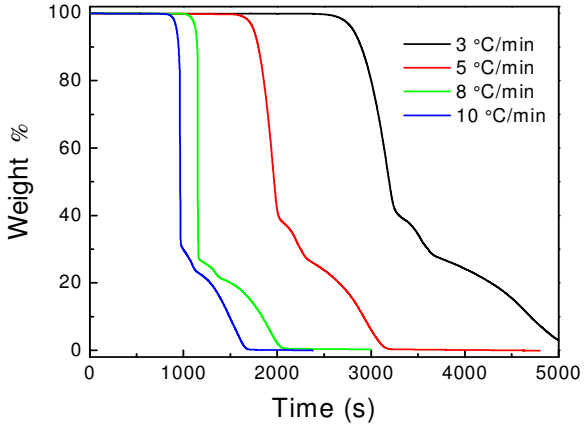


**Figure 4-3 TGA thermographs showing CBA decomposition at 220 °C under different heating rate.**

As clearly shown in Figure 4-3, CBA decomposed at a relatively narrow time frame at 220 °C, it is crucial to obtain a RPh system which gels within the time frame in order to match the rapid gas liberation rate. RPh needs to gain sufficient melt strength to stabilize the bubbles before gas liberation ceases so as to provide resistance for the cellular structures from collapse. To the contrary of all the past research which focused on the development of phthalonitrile based polymer with long pot life to facilitate composite processing, a fast gelling system need to be developed in this case. Table 4-1 lists the gelation time at temperature from 190 – 220 °C for some of the additives used in phthalonitrile polymer development, 1, 4-bis-aminophenoxy (APB) was found to be the most appropriate additive. In this study, we define gelation as the state when drastic viscosity increase was observed from the viscosity versus time graph.

**Table 4-1 Gelation time for RPh/curing additive at different temperature.**

| Curing Additive | Hydro-quinone | Copper salt | Zinc Salt | APB | 1,3-bis4-amino phenoxy | Copper powder |
|---|---|---|---|---|---|---|
| | Gelation time (min) | | | | | |
| 190 °C | > 30 | > 30 | > 30 | > 30 | > 30 | > 30 |
| 200 °C | > 30 | > 30 | > 30 | ~13 | > 30 | > 30 |
| 210 °C | > 30 | > 30 | > 30 | ~10 | ~20 | > 30 |
| 220 °C | > 30 | > 30 | > 30 | ~7 | ~20 | > 30 |

The gelation time was successfully reduced to within 10 minutes through proper additive selection, temperature adjustment, and prepolymer preparation. Figure 4-4 shows the viscosity profiles obtained for RPh/APB at different temperature under steady shear rate of 1/s. Results from Figure 4-2 and Figure 4-4 were overlaid and presented in Figure 4-5. At 190 °C, no gelation was observed after 20 min of heating, and CBA liberated limited

amount of gas for foaming. At 220 °C, the gelation time coincided with the time when rapid gas liberation was occurring, this system was expected to gain sufficient gel strength to enclose the gas within the matrix, leading to stable foam formation.

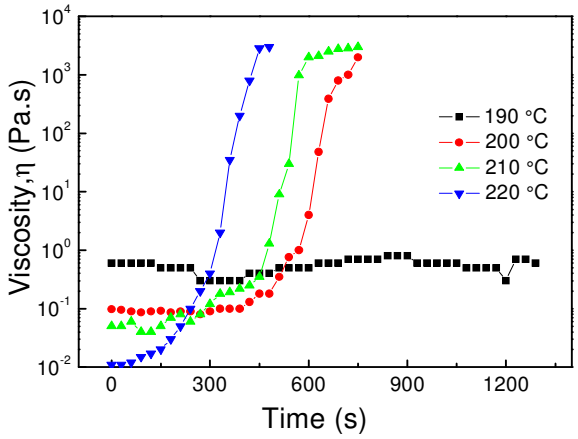


**Figure 4-4 Viscosity of RPh/APB at different temperature**

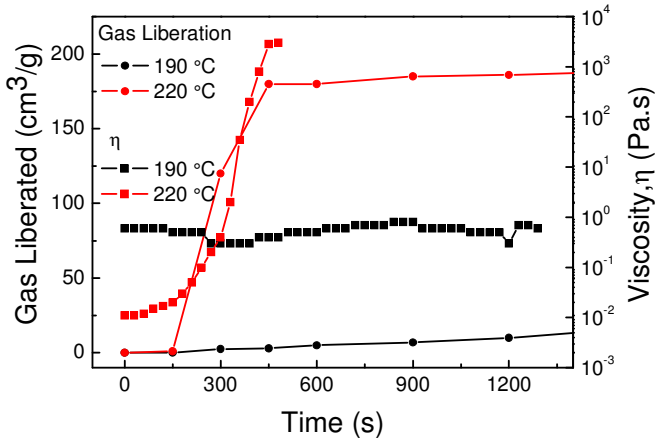


**Figure 4-5 Diagram showing the relationship between gas liberation and viscosity change at 190 °C and 220 °C.**

### *4.2.1.2 Effects of Temperature on Foam Development*

To study the effects of temperature on foaming, CBA was fixed at 2.5 wt% and the amount of polymer used was also kept constant. When being foamed at 200 °C, foams with higher than expected density were observed, consisting of non-spherical closed cells

well-separated by thick struts as shown in Figure 4-6(a), This morphology denotes unsuccessful foaming when the foaming temperature was too low. Firstly, the amount of gas generated was unable to fill up the entire foaming mold. Secondly, the gas was insufficient to generate enough pressure difference to overcome the high resistance for bubble growth imposed by the high melt viscosity at low temperature.

On the other hand, the desired foam density was achieved when the temperature was increased to 280 °C, but irregular cell structure and indefinable cell shape (Figure 4-6(b)) was observed due to the unsynchronized polymerization-gas liberation process. Increasing the foaming temperature did not only reduce the melt viscosity and accelerate the cell growth process, it also increased the pressure difference and provided additional driving force for bubble growth through diffusion. However, the polymer melt with much reduced viscosity was unable to solidify quickly enough to stop cell coalescence during the rapid cell growth. As a result, irregular porous structure was formed. The structure irregularity was also attributed to the accelerated thermal decomposition process of CBA which occurred before gelation.

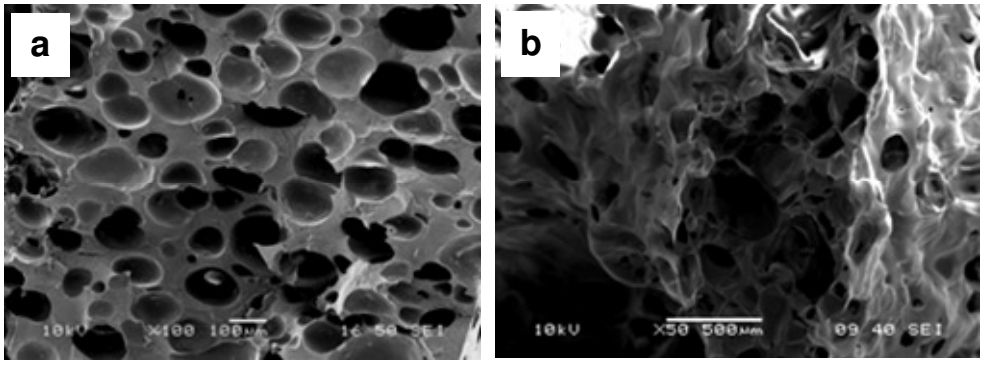


**Figure 4-6 SEI images showing foam morphologies of RPh foams foamed at (a) 200 °C and (b) 280 °C.**

#### *4.2.1.3 Effects of CBA Content on Foam Quality*

Table 4-2 summarized the foam density, foaming grade, average cell diameter and cell density calculated based on Equation 4-3 to Equation 4-8 at different CBA content with fixed amount of polymer. Foaming grade is a parameter determined by the foam density and is directly related to the concentration of CBA. The foaming grade increased with CBA wt% and reached the plateau at 2.5 wt%; when the amount of gas liberated was enough to fill up the entire closed mold. Further increase in CBA would affect the foaming grade because the foam density was fixed by the mold volume and the polymer mass. The effectiveness of CBA reached the threshold at about 2.8 wt%, after which the cell density dropped about 1 order of magnitude and the cell shape became irregular which measurement impossible. Excessive CBA content increased the amount of gas dissolved inside the polymer melt and reduced the melt viscosity through plasticizing effect and led to rapid bubble growth. Bubbles in close vicinity coalesced to achieve energy minimization in order to ease the pressure difference caused by the excess amount of gas, resulting in porous structure with fewer but larger cells as shown in Figure 4-7(c).

**Table 4-2 Relationship of CBA content in wt% to foam density, foaming grade, average cell diameter, and cell density.**

| CBA Content wt% | Density $g/cm^3$ | Foaming Grade (%) | Average cell diameter/cm | Cell Density $cell/cm^3$ X $10^5$ |
|---|---|---|---|---|
| 0.9 | 0.35±0.01 | 54.2 | 0.29 | 0.86 |
| 1.2 | 0.21±0.01 | 65.8 | 0.37 | 1.24 |
| 1.6 | 0.18±0.01 | 68.3 | 0.65 | 4.17 |
| 2.5 | 0.15±0.01 | 70.8 | 0.77 | 3.50 |
| 2.8 | 0.15±0.01 | 70.8 | 0.82 | 3.76 |
| 3.0 | 0.15±0.02 | 70.8 | 1.05 | 0.41 |
| 3.5 | 0.15±0.02 | 70.8 | -* | -* |

*** Measurement was impossible due to the indefinable cell morphology.**

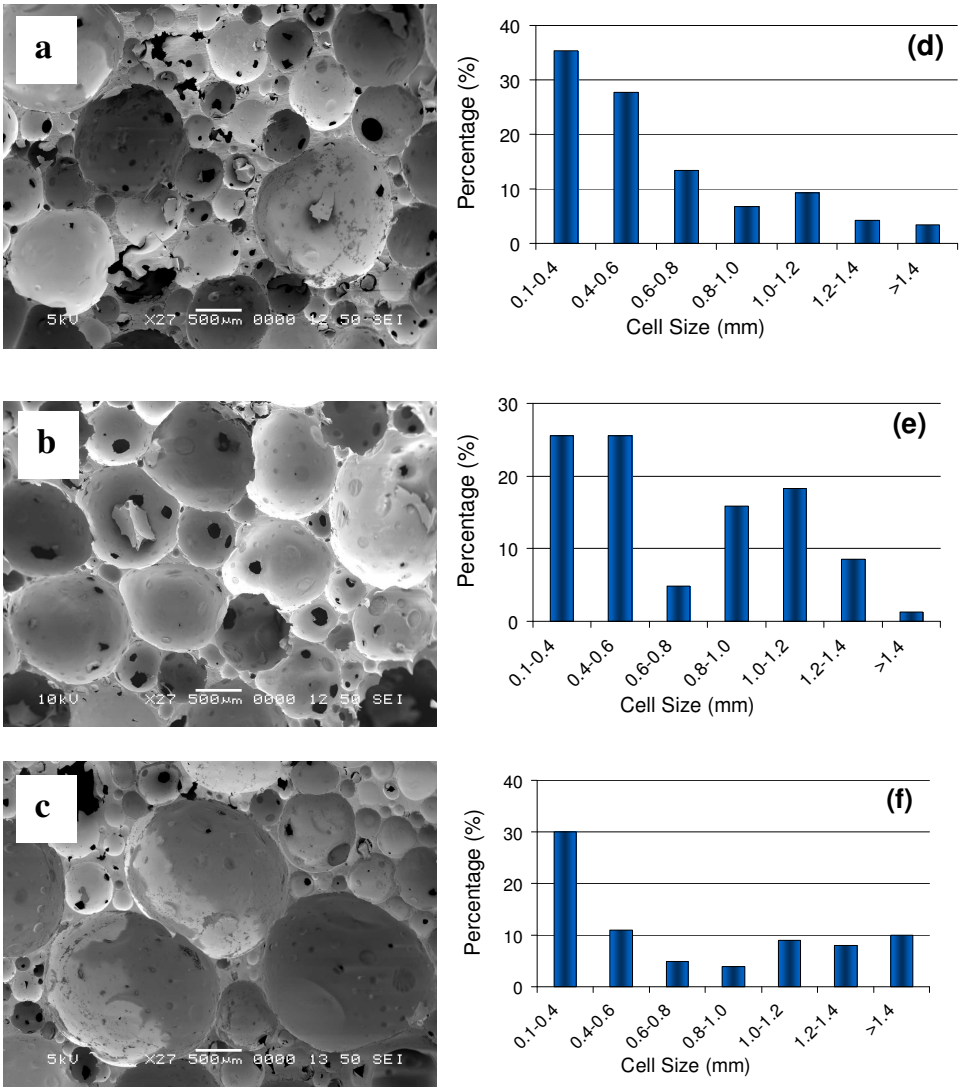


**Figure 4-7 SEI images showing morphologies for foams with (a) 1.5, (b) 2.5 and (c) 3.0 wt% of CBA, all foams have the density of 0.15g/cm$^3$, and foamed under 220 °C. (d), (e) and (f), present the cell size distribution in terms of percentage.**

Figure 4-7 provides direct evidence for the effects of CBA through morphological observation using SEM. When CBA content was low, the limited amount of gas liberated slowed down bubble growth and inhibited cell coalescence. The bubbles were spherical, closed cells, and well-separated by thick struts. A hierarchical distribution of cells was observed and was further illustrated by the histogram of cell size distribution. 2.5 wt% of

CBA resulted in foam with bimodal cell distribution (Figure 4-7(b)). Cell walls of thickness about 2-5 μm were spherical and of closed cells. Excessive CBA led to fewer but bigger cells as shown in Figure 4-8(c and f) as explained earlier.

#### *4.2.1.4 RPh Foam Formation*

RPh foam was fabricated for the first time through proper synchronization of polymerization and gas liberation. The nomenclature used to describe polymer foam and the steps in RPh foam with bimodal cell distribution development were shown in Figure 4-8. Upon heating, two processes occurred simultaneously: $N_2$ and $NH_3$ were released via thermal decomposition of CBA, molten polymer started to solidify by crosslinking. Gas bubbles were initiated when the gas concentration in the polymer melt exceeded the critical concentration. Bubbles were spherical when first being initiated and grew due to (i) the pressure difference between bubble and the polymer melt and (ii) the pressure difference between adjacent bubbles. Equalization of the pressure difference occurred through by growth or coalescence of smaller bubbles. Unlike typical low density polymeric foams, polygonal cell structure was not observed in any of our foam systems. Even at density as low as 0.15 g/cm$^3$, the cells remained spherical with adjacent cell walls touching like those in liquid foam (Figure 4-7 a,b,c). It was generally accepted that bubbles remain spherical because the interfacial area and the capillary pressure are at the minimum. However, in this case, it was believed that the cells remained spherical not because of the ideal mathematical principle. The high resistance force from the increasing viscosity made further cell growth impossible.

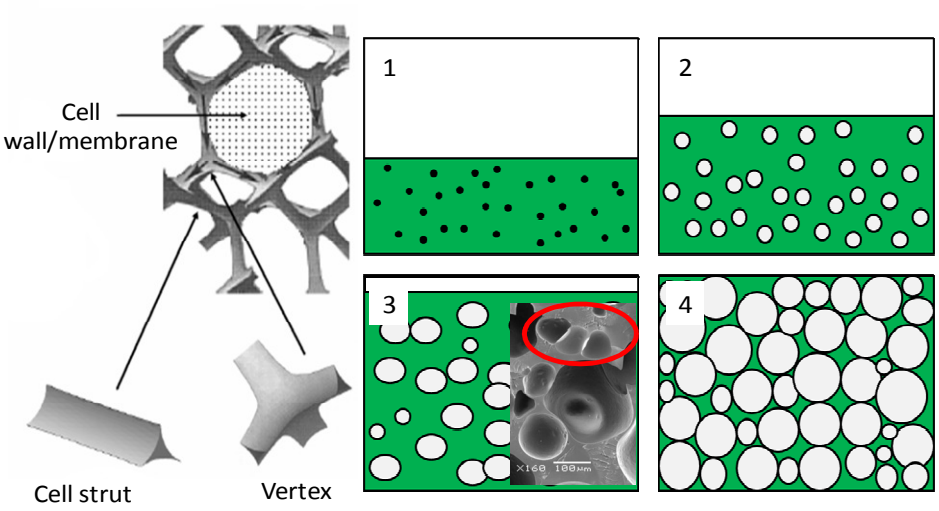


**Figure 4-8 Nomenclature of a typical cell structure and the development stages of rigid RPh foam. Step 1 shows foaming mixture, Step 2 shows bubble growth, Step 3 shows cell coalescence during cell growth and step 4 shows the final bimodal foam structure.**

### 4.2.2 Thermal Stabilities of RPh Foams

Table 4-3 summarized the thermal oxidative parameters of RPh foam. Char yield of the 0.2 g/cm$^3$ foams were found to be 82.3 and 68.5 wt% in $N_2$ and air respectively. The values were comparable to its void free samples and unattainable by most thermoset foams. Even at density as low as 0.08 g/cm$^3$, the char yield at 800 °C in $N_2$ was maintained at 63.5%. The high thermal stability was attributed by the high crosslinking density and the thermally stable structures formed during crosslinking as explained in Chapter 3. However, the porous foam structure failed to maintain the high char yield exhibited by the void free RPh (presented in Chapter 3) when subjected to severe oxidative conditions in air. To further understand the factors affecting the thermal stabilities, separate experiments were conducted to investigate the thermal properties as a function of postcuring and foam density.

**Table 4-3 Thermal oxidative parameters of RPh foams obtained by TGA.**

| Density | Onset Degradation °C (5 wt% Loss) | | Char Yield at 600 °C (wt %) | | Char Yield at 800 °C (wt %) | |
|---|---|---|---|---|---|---|
| | $N_2$ | Air | $N_2$ | Air | $N_2$ | Air |
| 0.08 | 496 | 483 | 75.3 | 62.3 | 62.9 | 13.5 |
| 0.12 | 478 | 465 | 77.1 | 70.5 | 63.9 | 13.6 |
| 0.15 | 490 | 481 | 78.9 | 73.6 | 65.6 | 14.6 |
| 0.20 | 511 | 500 | 82.3 | 77.7 | 68.2 | 17.8 |

#### *4.2.2.1 Effects of Postcuring on the Thermal Properties*

Previous studies on void free RPh has shown that the superior thermal stability was mainly attributed by the high crosslinking density obtained through postcuring. This phenomenon should be applicable to the foamed products as well. Figure 4-9(a) shows that postcuring had indeed enhanced the thermal stability of RPh foams. Two-step degradation was observed from the curves of the derivative weight change (DTGA) presented in Figure 4-9(b). Degradation at 440 °C was mainly due to the decomposition of incomplete network formation and unreacted CBA. Further postcuring eliminated the unreacted CBA which could reduce the thermal stability due to plasticizing effects. The char yield increased gradually as more nitrile groups (C≡N) were converted to high temperature resistant macrostructure of pthalocyanine and triazine, which are known for their high thermal stabilities. The highly crosslinked system obtained through progressive postcuring also contributed to the extremely high char yield.

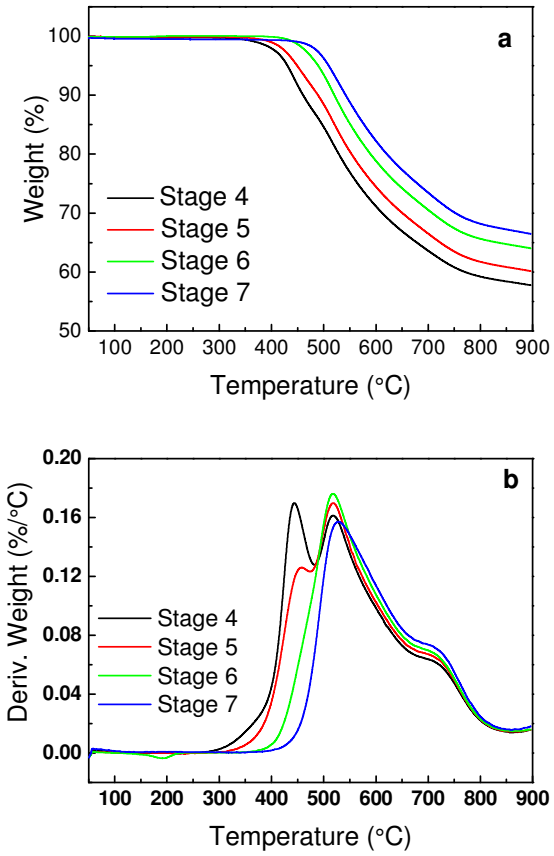


**Figure 4-9 (a) TGA and (b) DTGA graphs showing effects of postcuring on thermal stability in nitrogen. (Foam used: density 0.15 g/cm$^3$, 2.5 wt% CBA).**

### *4.2.2.2 Effects of Density on the Thermal Properties*

Density is another factor affecting the thermal stability of foam. Figure 4-10 shows TGA graphs for foams with different density. For higher density foams, the thermal stability was slightly increased because less surface area was exposed to direct heat and the thicker struts were able to withstand thermal decomposition more than the thin cell struts. Another contributing factor is the type of cell existing within the matrix. Low density foam contained thin cell membranes which were more prone to breakage, and caused voids appearing on the cell membranes. These voids provided air passage to the inner cells which were originally protected by the outer layer of closed cells.

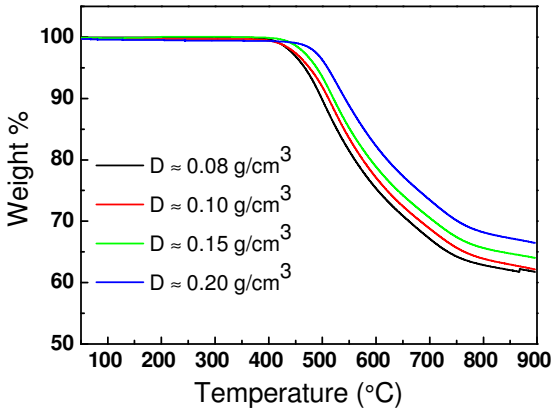


**Figure 4-10 TGA graphs showing effect of density thermal stability in $N_2$.**

### 4.2.3 Mechanical Properties of RPh Foams

All samples tested under compression exhibited elastic-plastic characteristics of typical rigid foams, as shown in Figure 4-11. The data was further condensed to show the peak stress ($\sigma_y$) and stress at 50% strain ($\sigma_{50}$) presented in Figure 4-12. All stress-stain curves, except for 0.04 g/cm$^3$ in which peak stress ($\sigma_y$) was absent, exhibited four stages of deformation: elastic behaviour, post-peak softening, plateau, and densification. The absence of $\sigma_y$ for 0.04 g/cm$^3$ could be due to the highly porous structure and large degree of inhomogeneous cells; causing the foam to deviate from rigid foam behaviour. Substantial progress in identifying the mechanism of deformation and failure in polymeric and metallic foams were made [10, 135-138] and the mechanism was used to explain the compression failure of the rigid, brittle RPh foam.

It was reported that for ideal closed cell foam of low relative density (< 0.2 g/cm$^3$), when the foam is being loaded, cell membrane stretching dominates and the stress is linearly dependant on the relative density [62, 135]. The same phenomenon was observed for RPh foams and confirmed by the almost linear increase in $\sigma_y$ and $\sigma_{50}$ values as density

increased from 0.04 to 0.20 g/cm$^3$. Further compression caused the struts and membrane to bend plastically and was defined as the post-peak softening. Rupture of the cell membranes and struts were initiated after plastic deformation and resulted in the appearance of the serrated plateau which confirmed the brittle nature of the RPh foams. Once all the cells have collapsed, further deformation pressed the opposing cells against each other and increased the stress sharply lead to densification[62]. It was expected that for the thicker struts and closed cells of high density foams would increase the compression modulus. This phenomenon was confirmed by the steeper gradient of the linear elastic region of the stress-strain curves (illustrated in inset of Figure 4-11).

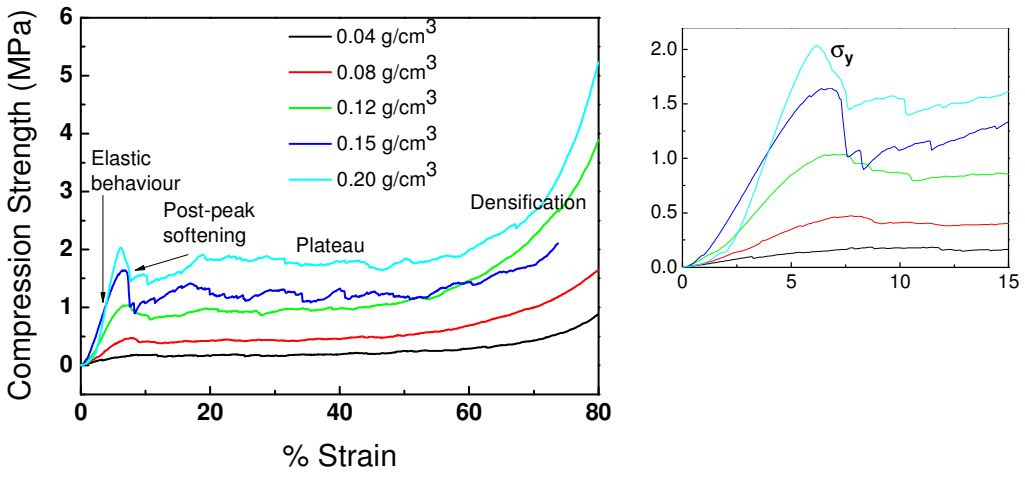


**Figure 4-11 Stress-strain curves of foam samples up to densification, insert showing the stress-strain curve for strain range of 0-15 %.**

Figure 4-12 also shows the percentage of compression stress retention after thermal aging at 280 ℃ for 100 hours. Foams with density larger than 0.12 g/cm$^3$ achieved 95% properties retention. The results have further proved the potential of RPh foams to be used for HT applications for extended period of time.

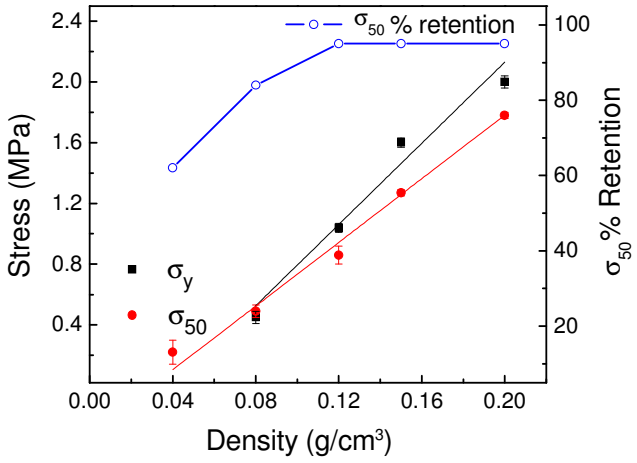


**Figure 4-12 $\sigma_y$, $\sigma_{50}$ (fully filled symbol) as a function of foam density, and , $\sigma_{50}$ retention (hollow symbol) for foams subjected to thermal aging at 280 °C for 100 hours in air.**

## 4.3 Summary

This chapter highlights the importance of the establishment of a balanced relationship between polymer gelation and CBA gas liberation for foam fabrication. RPh thermoset foams were successfully fabricated for the first time through a synchronized gelation-gas liberation process. It is demonstrated that the gelation time for RPh can be significantly reduced from hours to within minutes through proper additive and temperature selection in order to match the rapid gas liberation time for CBA. The final foam morphologies were affected by the CBA content and the foaming temperature used. Excessive CBA increased the cell size and the cell size distribution due to plasticizing effect on the polymer melt. Increased foaming temperature would accelerate cell growth through reducing the polymer melt strength.

Studies on thermal properties showed that postcuring was essential to increase the crosslinking density and to promote the formation of thermally resistant structures to enhance the thermal properties of the porous structure. The properly cured RPh foams showed superior thermal properties which were unattainable by other reported thermoset foams. The >95% compression stress retention after thermal aging at 280 °C for 100 hours further justified the superior thermal property and the suitability of RPh foams to be used under high temperature for extended period of time.

The RPh foams demonstrated typical rigid foam stress-strain behaviour under compression. The linear relationship of $\sigma_{y,}$ and $\sigma_{50}$ versus density provided direct evidence for the main deformation mechanism during elastic deformation stage. Further research is needed to develop methodologies to produce foams with uniform cell size distribution and enhanced foam properties.

# 5 NANOCOMPOSITE RPH FOAMS

Incorporating nanofillers into polymer matrix for material performance enhancement has been well recognized and were extensively reviewed in Chapter 2. Comparing to the amount of works on void free nanocomposites, little was done on nanocomposite foams, especially on thermoset foams. The limited studies could be due to the lack of knowledge on the complex crosslinking system which poses challenges in designing a suitable system for foam preparation. The detailed rheological studies in chapter 3 enabled the fabrication of rigid RPh foam through a synchronized single-step polymerization foaming process; exhibiting excellent short and long term thermal properties. This part of the work aims to further improve the foam through incorporation of nanofillers.

The nano-scale fillers are especially beneficial for microscale reinforcement primarily because the bubble cell wall thickness is within the micron and submicron size regime. Improvements in thermal, electrical, and mechanical properties could be achieve by synergistically combining the properties of the matrix and the fillers without altering the desired density [104, 114, 139-142]. Besides performance enhancement, nanofillers played multiple roles during foam development. Well dispersed nanofillers may (i) serve as heterogeneous nucleation centres facilitating the formation of bubbles, improving the cell density, and homogenizing the cell size; (ii) modify the rheological behaviour of the polymer; and (iii) regulate the bubble stability based the combination of *Gibbs* and *Marangoni* effects.

Nucleation mechanism due to nanofillers addition for foaming is a complex issue and remains a research topic to date; but it is generally agreed that filler size, shape, dispersion and surface treatment are the main factors affecting the nucleation process [79,

143-145]. In this chapter, three types of nanofillers with distinctly different aspect ratio were selected for study, i.e. 0D particles, 1D nanotubes, and 2D nanosheets, to understand of the shape effects on nucleation, rheological behaviour, and foam properties. Direct proof was obtained for the formation of nascent bubble at nanofiller-rich regions. Most of the studies discussed the bubble stabilization process due to the addition of nanofillers were done on liquid foams and few were targeted at crosslinking systems [82, 146-148]. This study focused on the details of bubble stabilization due to nanofiller addition for thermoset system with high crosslinking density, an area which was less addressed. Complex reinforcement mechanisms for each porous structure were also proposed.

## 5.1 Experimental

### 5.1.1 Materials

RPh was in-house synthesized using the method described in Chapter 3. Three types of nanofillers with distinctly different aspect ratio were chosen for this study. Fumed silica (FS) from Aerosol was used as received. Hydrophilic FS was selected since hydrophobic particles are generally confined at the polymer melt-particle interface and lead to bubble rupture. MWNT was obtained from Tsinghua University, Beijing, China. The MWNT was synthesized using gas phase floating bed reactor, with purity of > 90%, contained trace of residual Ni and Co catalysts as impurities. The average nominal diameter is about 20-50 nm. Naturally flake graphite with an average diameter of 500 μm, supplied by Shandong Qingdao Company (China) was used for preparing exfoliated graphite. MWNT and GH were chemically treated to enhance filler dispersion. (Detailed chemical treatments refer to appendix III).

### 5.1.2 Viscosity Profile of Nanofiller Filled Polymer Melt

Viscosity of the nanofiller filler polymer melt was obtained using Anton Paar Physica MCR501 equipped with precision heat control chamber. Cone and plate with diameter 50 mm was used. The complex viscosity was determined as a function of time at constant angular frequency of 1 rad/s.

### 5.1.3 Nanocomposite Foam Preparation

Nanocomposite foam development process was extended from the process presented in Chapter 4, session 4.1.4. The prepolymer was prepared from nanofillers/RPh mixture as described in Chapter 3.

### 5.1.4 Foam Characterizations

***Morphology:*** refer to Chapter 4, session 4.1.5.

***Thermal properties:*** refer to Chapter 4, session 4.1.5

***Mechanical properties:*** refer to Chapter 4, session 4.1.5.

***Thermomechanical properties:*** The thermomechanical properties were studied using Dynamic Mechanical Analyzer Q500, TA Instrument. Samples were cut into dimensions of 17.5 x 1.5 x 3 $mm^3$. Single cantilever clamp setup was used. Temperature sweep was carried out from room temperature to 400 ℃ in air at frequency of 1 Hz.

***Transmission Electron Microscopy (TEM):*** Polymer thin films were prepared using Leica Ultracut microtome equipped with diamond knife and collected on 400 mesh carbon film coated copper grids. Samples were analyzed with JEOL 2010 TEM with accelerating voltage of 200 kV.

## 5.2 Results and Discussion

### 5.2.1 Nanocomposite Foams Fabrication

Nanocomposite foams of RPh were prepared successfully based on a modified method described in Chapter 4. Nanofillers were added aiming to (i) reduce the foam cell size, (ii) increase the cell density and (iii) improve the foam properties. Scheme 5-1 illustrates the processing steps used for nanocomposite foam fabrication. Nanofillers were firstly mixed with RPh monomer by sonication and solution mixing. The solvent was removed from the mixture, followed by melt blending with curing additive to produce prepolymer with the right viscosity for foam development. Pre-calculated amount of CBA was added to the nanofillers/prepolymer mixture before the mixture was sealed in closed mold for the synchronized polymerization-gas liberation foaming process.

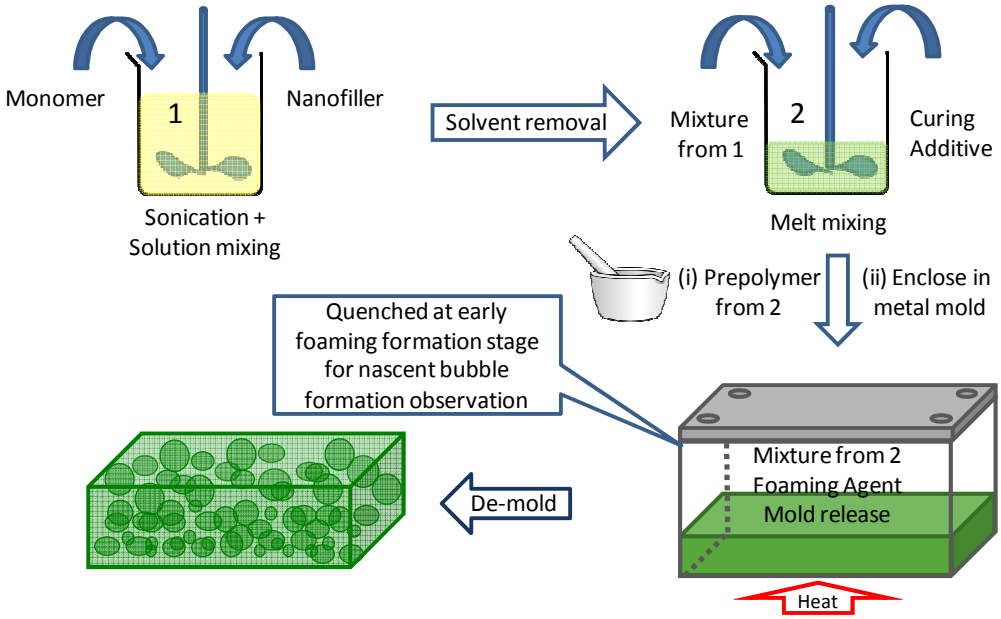


**Scheme 5-1 Schematic illustration of nanocomposite foaming process.**

Figure 5-1 shows the morphologies of neat RPh foam and its nanocomposite foams. Smaller cells were obtained for the nanocomposite foams; however, there was a

significant increase in the number of microvoids on the cell membranes from all the nanocomposite foams. Unique 'cage-like' structure was observed from FS and GH containing foams. The cells represented neither closed nor open cell structure. Each cell appeared as well-separated individual cell interconnected to the neighbouring cells through the microvoids on the cell wall. RPh/MWNT foam shows similar morphology as the RPh foam, but with much reduced cell size. The formation of the new morphologies was studied from two aspects: the rheological changes and the presence of nanofillers.

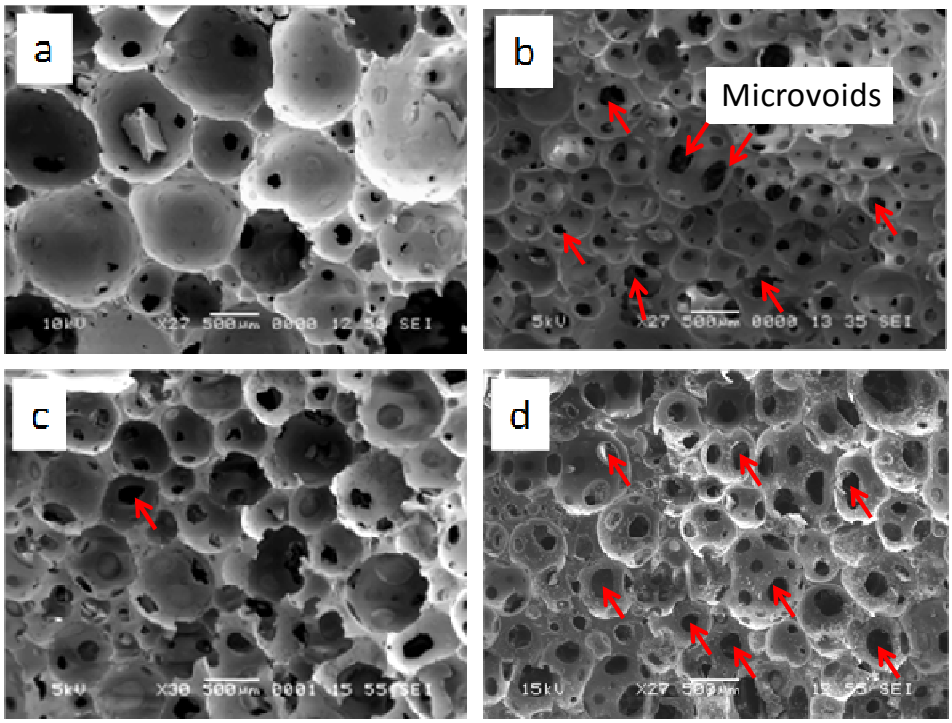


**Figure 5-1 SEI images of foam morphologies for (a) RPh foams (b) RPh/FS foam, (c) RPh/MWNT foam, and (d) RPh/GH foam.**

### *5.2.1.1 Effects of Rheology on Nanocomposite Foam Fabrication*

Viscosity played an important role in the process of bubble drainage, growth and stability leading to different morphologies. Previous attempts to relate the viscosity changes caused by filler additions to foam drainage and stability were limited to liquid foam

systems [149-151]. This part of the work attempted to establish a viscosity-foaming relationship for crosslinking systems and discuss the effects of rheology on foam morphologies.

Increases in complex viscosity and extended gelation time were observed from Figure 5-2 for different nanofillers at fixed loading content under constant shear rate of 1/s. (Detailed Figures are included in appendix Figure VI-1). MWNT and GH increased the magnitude of the complex viscosity by 3 and 4 orders of magnitude respectively while only 100 times of increase was observed for FS, all at 1 wt%. The drastic increase imparted by MWNT and GH was resulted from the π-π interaction between the aromatic heterocyclic structure formed during crosslinking and the graphene sheets from MWNT and GH. The slightly increased complex viscosity in RPh/FS system was purely due to physical interactions. The nanofillers also acted as physical barriers which increased the viscosity and slowed down the gelation process of RPh resin. MWNT, with its highest aspect ratio, interfered the crosslinking process and no gelation was observed after 25 min of reaction.

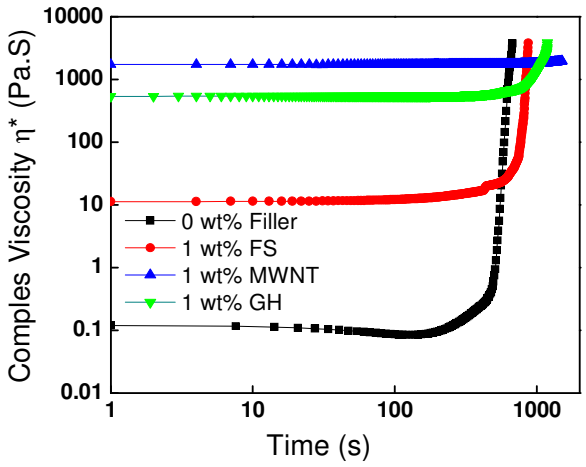


**Figure 5-2 Complex viscosity of RPh/nanofillers systems as a function of time at constant angular frequency of 1 rad/s.**

Contradicting behaviours were observed during foaming due to the rheology changes. Bubble growth was slowed down due to the greater amount of energy required to overcome the gel strength from the highly viscous polymer melt. Thinning of membranes by draining process was significantly retarded when liquid flow became difficult. The high gel strength also provided resilience to the cells from rupture. As a result, smaller bubbles were preserved. On the other hand, foam stabilization by crosslinking was unable to take place as long as the foaming system remained as liquid. Liquid cell drainage and local movement of the nanofillers continued to occur during the extended gelation time frame which caused cell coalescence and microvoids formation. Hence, reduced cell size and microvoids on cell wall were resulted as shown by Figure 5-1.

The RPh/MWNT system resembles foam formation in a highly viscous liquid rather than in a fast crosslinking thermoset because no gelation was observed after 25 min of reaction. Liquid foam is intrinsically in the non-equilibrium states, characterized by the continuous liquid cell rearrangement till the gas phase is completely separated from the liquid phase and vanish. The absence of gelation within the gas liberation time frame was expected to result in foam failure due the absence of foam stabilization. However, excessive cell movement was prevented by the formation of a physical gel, demonstrated by the higher dynamic elastic modulus (G′) values over the dynamic viscous modulus (G″). The high melt resilience of the physical gel combated cell movement and prevented the cell struts and vertices from collapse before chemical crosslinking occurred. As a result, well defined spherical cells were obtained (Figure 5-1(c)). Foaming through physical gel demonstrated here provided an alternative mean of foam fabrication when synchronization of gas liberation and gelation cannot be achieved.

#### *5.2.1.2 Roles of Nanofillers in Foaming Process*

***Nanofillers as nucleating agent:*** The role of nanofillers as nucleating agents was verified by quenching the foaming process at the very early bubble formation stage and observed the morphology using TEM. It is evident from Figure 5-3 that bubbles were initiated at the nanofillers-rich regions. During foaming process, the dispersed nanofillers became the 'hot spot' and reduced the surface tension ($\gamma$) at the liquid-solid interface and locally lowered the free energy ($\Delta F$) required for new phase initiation (in this case, the gas bubbles). As a result, these sites with reduced free energy barrier promoted simultaneous bubble formation.

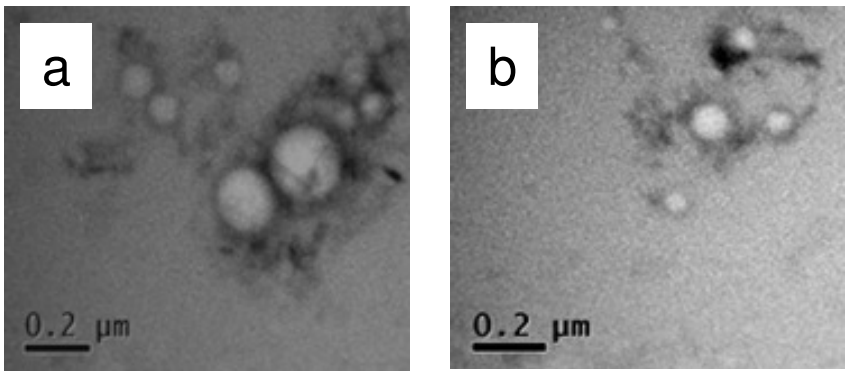


**Figure 5-3 TEM images showing bubbles formation at nanofiller-rich regions. (a) RPh/FS foam, and (b) RPh/MWNT foam.**

The cell density calculated based on Equations 4-4 to 4-6 and the average cell diameters calculated based on Equation 4-3 were presented in Table 5-1. The cell density was generally increased by about 3 orders of magnitude at fixed density. The histogram in Figure 5-4 shows that nanofillers additions effectively narrowed down the cell size distribution, among which all the cells were below 1 mm for RPh/GH foam. When excess fillers were added, (> 3 wt% FS, > 2 wt% MWNT, and >2 wt% GH), the mismatched

viscosity and gas liberation caused the cell morphologies to become irregular. None of the fillers chosen has exhibited clear advantage in term of nucleation effectiveness. However, the observation did not contradict the reports on the shape effects on nucleation. The insignificance difference is believed to be due to the poor dispersion. As observed from the SEI micrographs in Figure 5-5, the effective surface area available for heterogeneous nucleation was severely reduced by the agglomerated nanofillers.

**Table 5-1 Foam density, cell density and average cell diameter of pure and nanocomposite RPh foams.**

| Foam Type | Foam Density $g/cm^3$ | Cell Density ($N_o$) $x10^{8}/cm^3$ | Average cell Diameter (μm) |
|---|---|---|---|
| Pure RPh | 0.15 ± 0.01 | 0.0035 | 750 |
| 2 wt%-FS/RPh | 0.15 ± 0.01 | 9.3 | 510 |
| 1 wt%-MWNT/RPh | 0.15 ± 0.01 | 8.1 | 570 |
| 1 wt%-GH/RPh | 0.15 ± 0.01 | 5.4 | 640 |

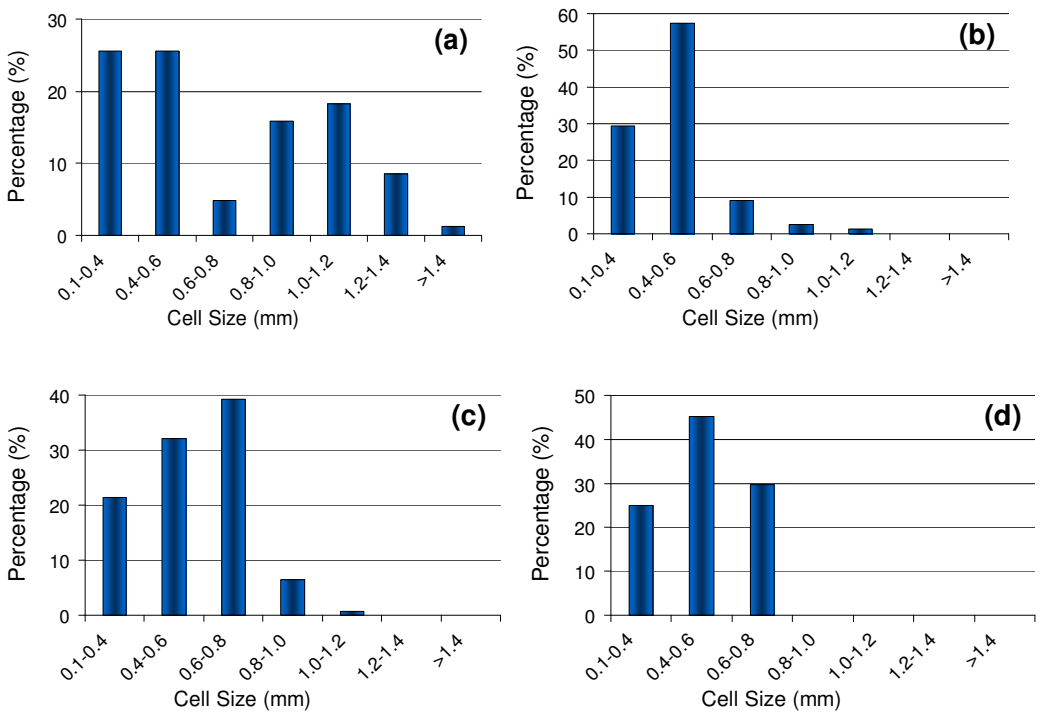


**Figure 5-4 Cell size distribution of (a) RPh foam, (b) FS/RPh foam, (c) MWNT/RPh foam, and (d) GH/RPh foam.**

***Bubble stabilization due to nanofillers additions:*** The extended gelation time provided more time for nanofillers movements in the liquid cell and eventually affected the bubble stabilization process. The growing bubble disturbed the concentration of the evenly dispersion nanofillers cluster in RPh resin (Figure 5-5) and caused local movement of the nanofillers in order to restore the concentration difference. The surrounding molten polymer was dragged along when nanofillers diffused from high to low concentration causing thinning of the cell membrane. According to Gibbs, cell breakage occurred when the underlying polymer was unable to restore the cell membrane thickness. Figure 5-6 illustrates the concentration restoration process and direct visual evidence of a microvoid being initiated at FS cluster.

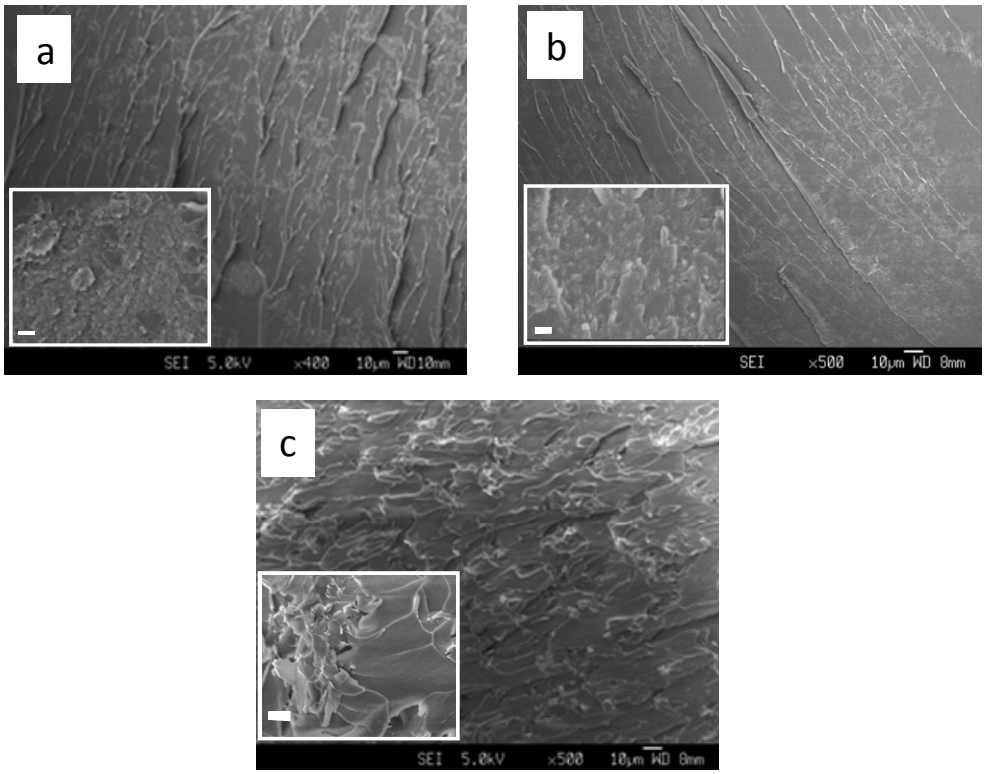


**Figure 5-5 SEI images showing dispersion state of (a) 2 wt% FS, (b) 2 wt% MWNT and (c) 2 wt% GH in RPh matrix, and (d) (e) and (f) are respective images showing the filler rich sites under higher magnifications. Insert scale bar represents 100 nm.**

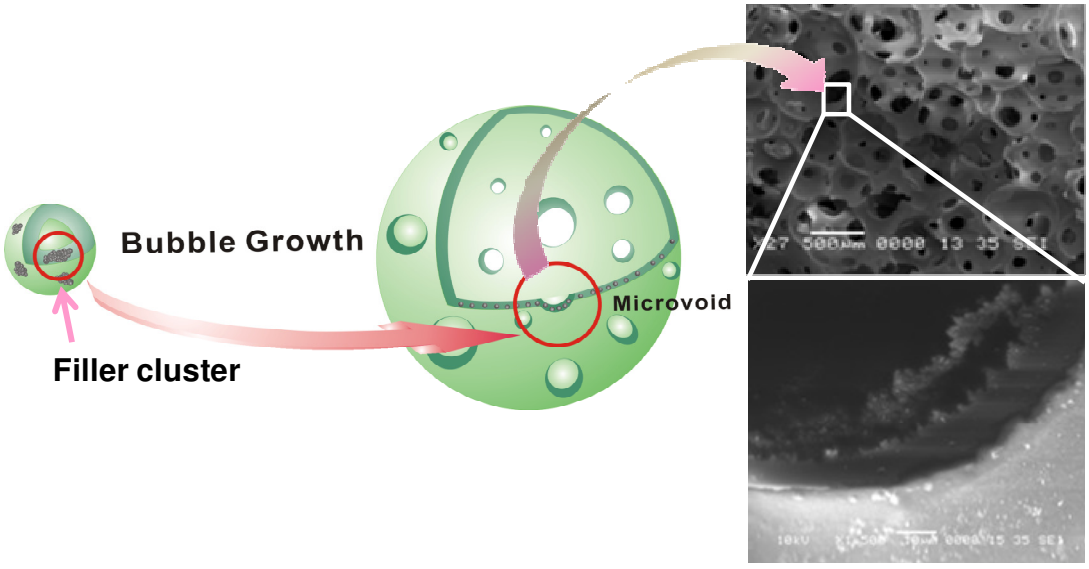


**Figure 5-6 Schematics illustrating concentration restoration of nanofiller cluster in the cell wall, the polymer melt was dragged along with the nanofillers, led to cell thinning and eventually rupture when the underlying polymer failed to restore the thinned cell membrane. SEI images showing microvoid being initiated at FS cluster.**

Besides concentration restoration, dewetting of liquid polymer from nanofiller aggregates might also cause bubble instability. As illustrated in Figure 5-7, before crosslinking occurs, the liquid polymer which defines the cell membrane and surrounds the nanofiller aggregate flows around the aggregate by dewetting. When the aggregate is totally isolated from the surrounding polymer melt, cell rupture is initiated.

Both mechanisms mentioned above disturbed the bubble stability and caused the formation of microvoids on the cell membrane. A well dispersed nanofiller/RPh system may help to improve the bubble stabilization process.

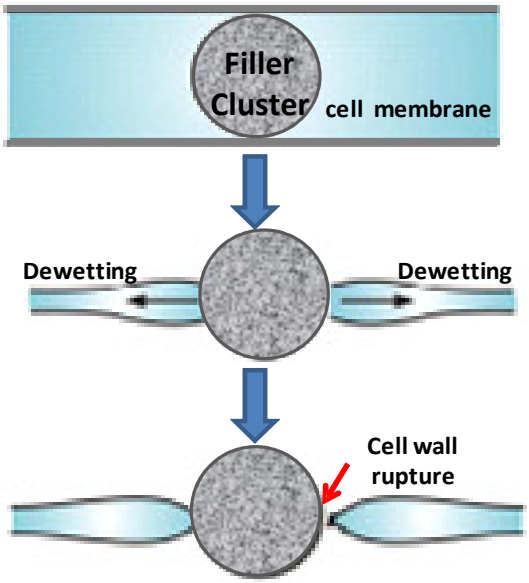


**Figure 5-7 Schematics illustrating cell wall rupture initiated by particle existing in the cell wall due to dewetting.**

### 5.2.2 Effects of Nanofillers on Thermomechanical Properties of Nanocomposite Foams

Figure 5-8 shows the storage moduli (E′) and loss moduli (E″) of RPh/FS foam obtained from room temperature to 400 °C at different filler content (Refer to appendix Figure VI-2 for RPh/MWNT and RPh/GH foams). E′ increment was achieved when an appropriate amount of nanofillers were added. The well dispersed nanofiller clusters acted as physical crosslinking sites prevented the movement of the polymer segments at temperature below $T_g$. As temperature approached $T_g$, polymer chain motions increased in amplitude and start to destroy the nanofillers domains, causing rapid chain relaxation to occur. This was supported by the increased loss moduli E″ shown in Figure 5-8 (b). Further increasing the filler contents however led to drastic drop in the glassy E′ because excessive amount of fillers act as barriers, decreasing the crosslinking density and caused E′ to drop. The loss moduli E″ increased with the filler concentration up to a weight fraction of 0.03, 0.01 and

0.01 for FS, MWNT and GH before a decrease was observed. The decrease could be due to dewetting of the excessive amount of fillers present inside the matrix.

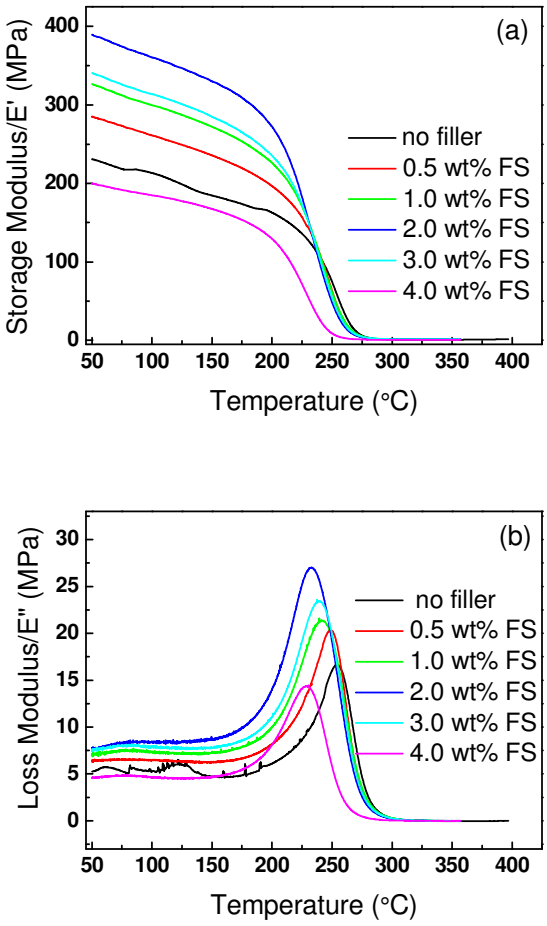


**Figure 5-8 Storage modulus and loss modulus of RPh/FS foams.**

E′ at 50 °C for all the samples was summarized in Figure 5-9 for easy comparisons. A large improvement was observed by adding merely 0.1 wt% of MWNT and GH with GH being the more effective reinforcement. FS appeared to be less effective judging from the more gradual increase. Marked improvement of 90 % was observed with 1 wt% addition of GH. Considering the low nanofillers content, the stress transfer between the matrix and MWNT and GH is fairly effective. The stress transfer probably benefits from the π-π interaction, and this is especially prominent for the case of GH as both the aromatic

heterocyclic structure and GH present in the form of 2D sheet, which promotes parallel π-π stacking of the species. Moreover, the acid treatment for MWNT and GH introduced COOH functional groups onto the filler surface that react with the amine curing additive and introduced additional crosslinks into the system. However, E′ started to drop after reaching the maximum values. This could be due to the inhibited crosslinking process by the nanofillers. As the concentration of nanofiller increased, aggregation became more severe which in turn increased the free volume in the system and reduced the aspect ratios, both factors contributed to the decreased E′ values.

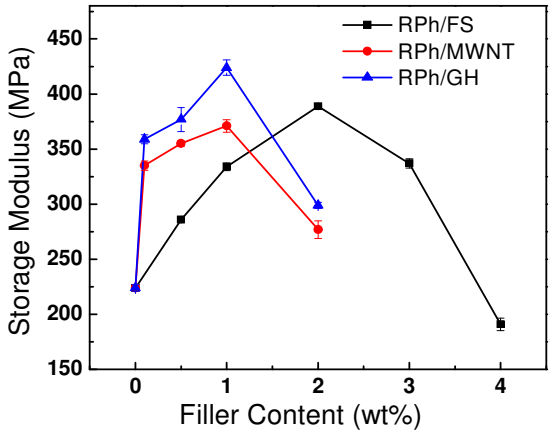


**Figure 5-9 Storage modulus for different nanocomposite foams as a function of filler content.**

### 5.2.3 Effects of Nanofillers on Compression Properties of Nanocomposite Foams

The rigid nanocomposite foams exhibited similar stress-strain behaviour (Figure 5-10) during compression. The compression stress were further converted to specific compressive stress and presented in Figure 5-11. The microvoids on the cell membrane of the 'cage-like' structure in FS nanocomposite foams weakened the load bearing capacity and decreased the compression stress compared to the close cell structure of RPh foam. MWNT and GH generally increased the compressive stress.

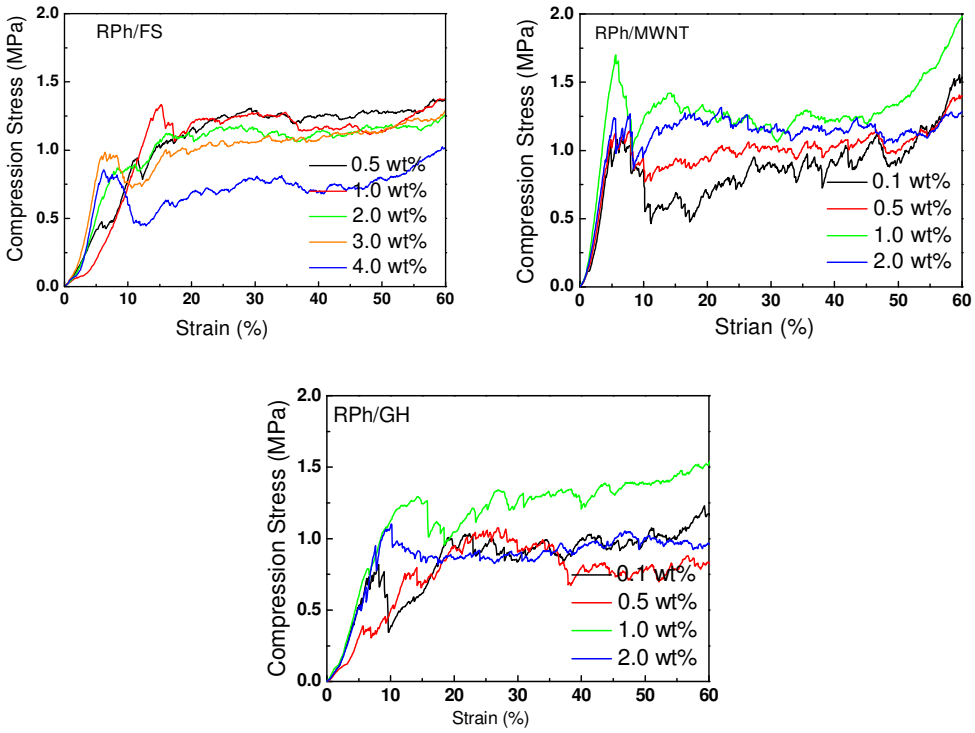


**Figure 5-10 Compression stress-strain curves for nanocomposite foams at density of 0.12 g/cm$^3$ at room temperature.**

At a given density, close-cell foam tends to show higher plateau stress than open-cell foams during compression through the compression of gases trapped inside the closed cells [69]. However, we observed higher plateau stress for MWNT and GH filled foams despite the presence of the interconnecting microvoids on the cell wall. Plateau stress increments of 33% (MWNT) and 51% (GH) were obtained with addition of 1 wt% of the fillers respectively. The biaxial bubble extension during the growth aligned MWNT and GH in the direction parallel to the cell membranes. TEM micrographs in Figure 5-12 show that MWNT and GH appeared to be 'wrapped" around and reinforced the cell membrane, whereas FS being much smaller in size and aspect ratio appeared as clusters. Figure 5-13(b) shows a microscopic view of a cell surface entirely covered by GH forming an 'amour' on the cell surface which significantly improved the loading bearing

capacity. GH dispersed in the cell strut (Figure 5-13(a)) improved the struts during compression like reinforcement in bulk nanocompsites.

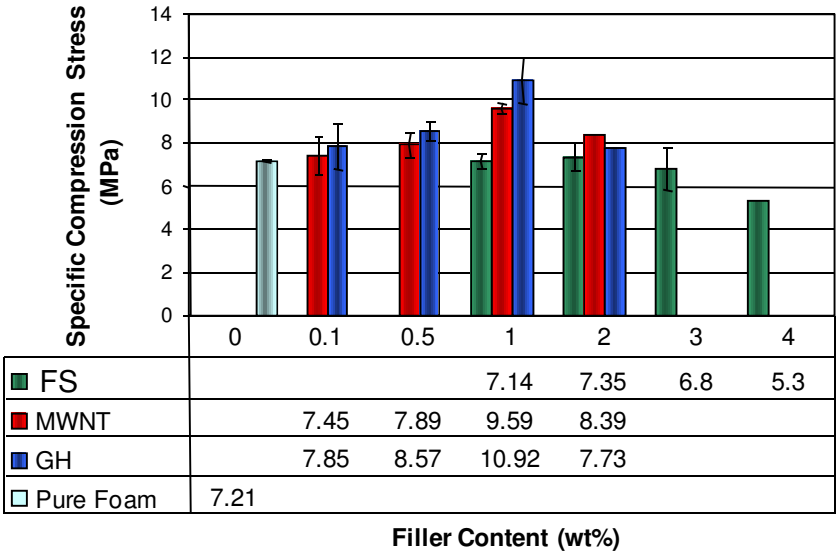


**Figure 5-11 Specific compression stress as a function of nanofiller content at foam density of 0.12 g/cm$^3$.**

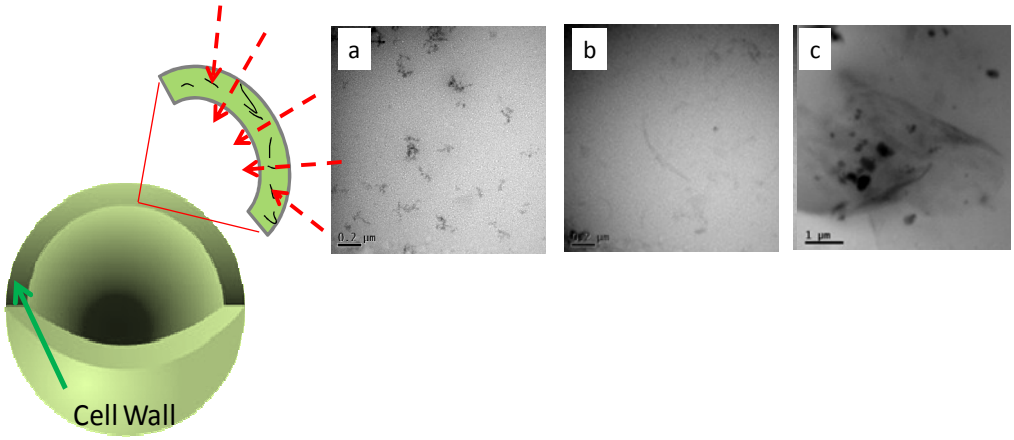


**Figure 5-12 Schematic illustration of a cell and the cell wall. TEM miages showing the nanofillers dispersion state in the cell walls of (a) FS, (b) MWNT and (c) GH. The micrographs were taken in the direction perpendicular to the cell wall thickness direction.**

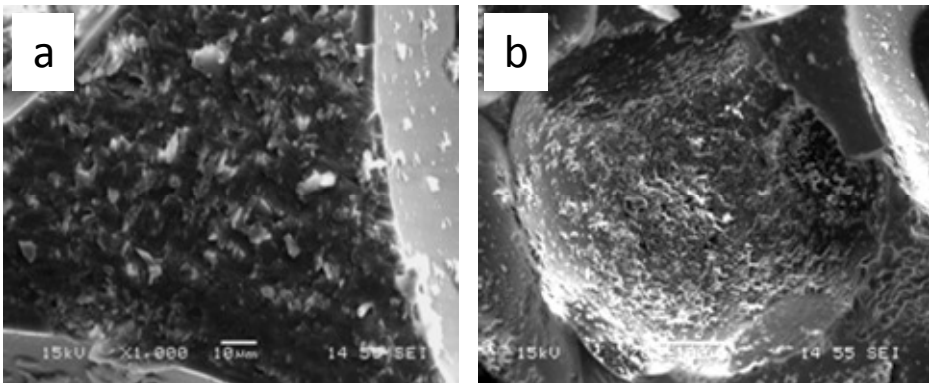


**Figure 5-13 SEI images of GH enhanced RPh foam (a) on cell strut and (b) 'Armoured' cell.**

### 5.2.4 Effects of Nanofillers on Thermal Properties of Nanocomposite Foams

FS caused negative effects in thermal properties (Table 5-2). The openings from the "cage-like" structures provided passage for heat transfer, the originally thermally insulated inner cells were subjected to thermal oxidative attack and exhibited poorer thermal stability compared to the neat RPh foams.

**Table 5-2 Thermal properties of RPh/FS foams.**

| Filler Content (wt%) | Onset Degradation °C (5 wt % Loss) | | Chat Yield at 600°C (wt %) | | Char Yield at 800°C (wt %) | |
|---|---|---|---|---|---|---|
| | N2 | Air | N2 | Air | N2 | Air |
| **0** | **490** | **481** | **80** | **74** | **66** | **15** |
| 1.0 | 485 | 474 | 64 | 54 | 46 | 12 |
| 2.0 | 486 | 474 | 66 | 55 | 49 | 11 |
| 3.0 | 485 | 470 | 64 | 53 | 45 | 12 |
| 4.0 | 453 | 421 | 58 | 44 | 34 | 8 |

Both MWNT and GH improved the thermal stability of the foams. $T_{5wt\%}$ and char yield at 800 °C in $N_2$ was increased by 20 °C and 7% by adding 1 wt% GH. The platelet shape provided more effective shielding effects when foams were subjected to thermal

decomposition (Table 5-3 and Table 5-4). The shielding effect combated the open passage caused by the microvoids and increased the thermal stability eventually. Again, high filler loading failed to give improvements due to the poor foam morphologies.

**Table 5-3 Thermal properties of RPh/MWNT foams.**

| Filler Content (wt%) | Onset Degradation °C (5 wt % Loss) | | Char Yield at 600°C (wt %) | | Char Yield at 800°C (wt %) | |
|---|---|---|---|---|---|---|
| | N2 | Air | N2 | Air | N2 | Air |
| 0.1 | 492 | 483 | 81 | 75 | 68 | 16 |
| 0.5 | 494 | 482 | 81 | 75 | 70 | 16 |
| 1.0 | 495 | 484 | 83 | 76 | 70 | 16 |
| 2.0 | 487 | 478 | 77 | 69 | 66 | 13 |

**Table 5-4 Thermal properties of RPh/GH foams.**

| Filler Content (wt%) | Onset Degradation °C (5 wt % Loss) | | Chat Yield at 600°C (wt %) | | Char Yield at 800°C (wt %) | |
|---|---|---|---|---|---|---|
| | N2 | Air | N2 | Air | N2 | Air |
| 0.1 | 498 | 490 | 82 | 78 | 70 | 16 |
| 0.5 | 507 | 494 | 83 | 77 | 70 | 17 |
| 1.0 | 510 | 499 | 85 | 79 | 73 | 18 |
| 2.0 | 492 | 482 | 77 | 70 | 69 | 15 |

## 5.3 Summary

RPh nanocomposite foams with precisely controlled density were fabricated by a one step foaming method. Unique ‘cage-like’ porous structures were resulted due to the interplay of heterogeneous nucleation and rheological changes brought by FS and GH addition. RPh/MWNT foams showed similar morphology to the neat RPh foam, but with cell density increased by more than 2000 times. The TEM images showing the formation of nascent bubbles at nanofiller-rich regions, the narrowed cell size distribution and

increased cell density provided evidences for nanofillers functioning as effective heterogeneous nucleation agents.

All RPh/nanofiller systems showed increased complex viscosity and extended gelation time which acted as double-edged sword on foam development. The increased viscosity slowed down cell growth process and prevented rapid cell coalscence and rupture. On the other hand, the prolonged gelation time allowed excessive nanofiller movements which jeopadized bubble stabilization and caused the formation of microvoids on the cell walls. No gelation was observed for RPh/MWNT system, however the formation of physical gel due to physical entanglement and π-π interactions made foaming possible even under the mismatched crosslinking and gas liberation profiles. Foam fabrication through physical gel provides an effective solution when synchonization of gas liberation and gelation cannot be avhieved.

FS improved the modulus of the nanocomposite foam through physical interaction but reduced the compression stress because the ruptured cell wall reduced the load bearing capacity. MWNT and GH improved both the modulus and compression stress despite the presence of microvoids through reinforcement arising from the effective π-π interaction. GH was the most effective reinforcement in this study due to the larger surface area subjected to π-π interaction. The nanofillers being dispersed in the cell wall increased the cell load bearing capacity by forming a ‘armour’ on the cell wall. Excessive nanofiller addition showed detrimental effects on every aspect of the nanocomposite foams because of the undesirable cell morphology and inhomogeneous nanofiller distributions.

# 6 CONCLUSIONS AND RECOMMENDATIONS FOR FUTURE WORK

## 6.1 Conclusions

The purpose of this research is to identify the structural formation of RPh resin during curing process to gain insights to the factors responsible for the superior thermal stability and to expand its applications to carbon materials fabrication and low density foams development for operating temperature > 250 °C. The important findings and main contributions of this thesis are summarized below:

### 6.1.1 Structural formation and carbonization studies of RPh resin

Insights to the understanding of the structural formation and intrinsic factors responsible for the superior thermal properties of RPh resin were obtained. It was found that at high curing additive content, besides the highly thermal stable aromatic heterocyclic structures, less thermally stable linear chains was observed, however, the thermal stabilities were not altered to a great extend. The highly crosslinked system obtained through postcuring were found to be responsible for the insignificant difference. The hypothesis was further supported by kinetics studies of curing and degradation.

The carbon film produced based on RPh were smooth and maintained the mechanical integrity upon carbonization. The increased crosslinkage and voids formation determined the final mechanical properties of the carbonized films. Pyrolysis of RPh films at different temperatures produced electrically conducting carbonaceous islands which eventually joined to form a continuous network with conductivity sufficient for electronic related applications. The good mechanical properties and electrical conductivity gained through

pyrolysis make it worthwhile to look into ultra thin carbon film and nano-scaled carbon structure, such as nanotubes, nanorod and nanorod array fabrication.

### 6.1.2 Foaming strategy for RPh Foam Fabrication

The challenges posed by the high processing temperature on foam fabrication of phthalonitrile based thermosets were overcome by synchronization between gas liberation of the CBA and gelation of the polymer melt. RPh was shortlisted from various phthalonitrile based resins due to the compatible crosslinking temperature with CBA decomposition. The right resin formulation was formulated based on (i) the systematically studied crosslinking kinetics of RPh resin and, (ii) the precisely controlled gelation time through curing additive selection and curing conditions optimization. Foaming temperatures and CBA contents were shown to be important parameters controlling the foam morphologies and qualities, hence should be taken into consideration for effective foaming strategy development.

Rigid RPh foams with precisely controlled density targeted for HT applications were fabricated for the first time. The foam morphology was mainly closed cell with the lowest attainable density of 0.04 g/cm$^3$. The compression stress obtained was comparable to rigid PI foams produced by NASA. The cured RPh foams showed superior thermally properties, > 80% char yield in $N_2$ at 800 °C, and > 95% compression stress retention after thermal aging at 280 °C for 100 hours, which were unattainable by any thermoset foams reported.

### 6.1.3 Nanofillers for Foam Morphology and Properties Enhancement

The nanocomposite foam fabrication demonstrated the multiple roles played by the nanofillers during foaming process. Different morphologies were resulted from nanofillers addition due to the interplay of heterogeneous nucleation and rheological changes. The nanofillers were proven to function as nucleation agents through the direct evidence obtained showing the formation of nascent bubbles at nanofiller-rich regions. The morphologies obtained showed high viscosity slowed down cell growth and reduced cell size while extended gelation jeopardized bubble stabilization causing microvoids formation. The bubble stabilization process for crosslinking system was discussed based on liquid cell stabilization and the mechanisms for microvoid formation were proposed. Moreover, this work showed that foams can be obtained through physical gel formation when chemical crosslinking and gas liberation synchronization cannot be established as demonstrated by the RPh/MWNT nanocomposite foams.

MWNT and GH were identified as better reinforcement fillers for phthalonitrile based resin comparing to FS due to the π-π interaction between the aromatic heterocyclic structures in the RPh resin and the graphene sheet from MWNT and GH. The storage moduli were increased by 50% and 60% by adding merely 0.1 wt% of MWNT and GH respectively. The GH sheets “wrapped” around the cell membrane and further improved the mechanical properties, making it the most effective filler among the three chosen for this study. However, excessive nanofiller content caused detrimental effects on every aspect of the nanocomposite foams because of the poor cell morphology and inhomogeneous nanofiller distribution.

## 6.2 Recommendations for Future Studies

The following works are recommended for future studies:

- ***Development of nanostructures with graphitic-like structure***

It was proven in chapter 3 that the superior thermal stability of RPh made it possible to obtain graphite-like structure upon pyrolysis. The films of thickness 1-2 μm exhibited good electrical and mechanical properties which are comparable to the carbon materials obtained through commonly used precursors. It will be of great interest to investigate the possibility of obtaining continuous, ultra-thin continuous graphite-like films on substrates using RPh as precursor. Several approaches are proposed:

(i) Spinning coating of dilute RPh solution

(ii) Thermal evaporation of RPh precursor

(iii) Film formation through Langmuir–Blodgett method

The good mechanical integrity showed by the carbon film makes it worthwhile to explore the potential of fabricating carbon nanostructures such as nanotubes and nanorod array through templating method.

- ***Dielectric properties of RPh foams***

To be used as dielectric material is one of the main applications of polymeric materials and is not investigated on this study as the focus was places on foam fabrication and the thermal and mechanical properties studies. It is known that the cell structure, distribution, and foam density are some of the parameters which will affect the dielectric properties of the foams. Cell structural control was obtained through nanofiller addition as shown in chapter 5. Investigation on the cell structure-property relationship will assist in widening of potential applications of the foam systems.

- ***Carbon Foams derived from RPh foams***

Carbon foam derived from various precursors such as phenolic, coal or pitch [152-155] have been studies for decades and are still popular in the area of carbon materials, especially carbon foams with high thermal conductivities due to the various applications. The thermally stable RPh foams are an ideal foam precursor to be used for carbon foam development. The highly crosslinked system with exceptional high char yield can be advantageous when comes preventing cell coalescence and collapse during heat treatment process. By choosing appropriate nanofillers such as CNT and graphite with extremely high thermal conductivity will further enhance the properties of the carbonized nanocomposite foams. The following aspects are worth looking into:

(i) Cell structure evolution up on carbonization

(ii) Electrical and mechanical properties of the carbonized foams

(iii) Effects of nanofillers on the final properties of the carbonized nanocomposite foams

(iv) Possibility of developing carbon-carbon nanocomposite foams

- ***RPh foam systems for bio-related application***

The unique 'cage-like' structure consisting of bubbles in hierarchical distribution is similar to the structure of the bone; this makes the foam material to be a suitable structure to be used in the biomedical application, especially for bone replacement. The well separated bubbles provide mechanical properties to the porous structure, at the same time, the microvoids on the bubble membrane provides pathways for living cell or tissue to grow within the entire foam. The compression strength lies in between that of polymeric foams and metallic foams and is suitable for bone implants where too low or too high

mechanical properties are not desirable. Preliminary experiments are being carried out at the moment and have shown promising results.

# LIST OF PUBLICATIONS

**Technology disclosure:** "Method to develop phthalonitrile based and its nanocomposite foams for ultra high temperature applications"

- Filing in progress

**Manuscript:** "Aromatic heterocyclic polymer as precursor for carbon materials"

- In preparation

**Manuscript:** "Development of polymeric foams for high temperature applications"

- In preparation

**Conferences:**

ICMAT 2007, Singapore

Paper presented: "Effects of CNT on the curing and thermal properties of phthalonitrile based thermoset polymer"

Eurofiller 2009, Alessandria, Italy

Paper presented: "Effects of nanofillers on the morphology and properties of rigid foams based on an aromatic heterocyclic polymer"

Engineering Plastic 2009, Dalian, China

Poster presented: "Morphology and properties control of nanocomposite foams"

IUPAC 43$^{rd}$ World Polymer Congress, 2010, Glasgow, UK

Paper presented: "Development of porous carbon film from aromatic-heterocyclic polymer through pyrolysis"

Engineering Plastic 2011, Kunming, China

Poster presented: "Aromatic heterocyclic polymer as precursor for carbon materials"

# REFERENCES


1. Keller, T. M. and Price, T. R., *Amine-cured bisphenol-linked phthalonitrile resins.* Journal of macromolecular science. Chemistry, 1982. **A18**(6): p. 931-937.
2. keller, T. M., *Synthesis and polymerization of phthalonitrile monomers containing multiple phenoxy and sulfone linkages* 1983, The United States of America as represented by the Secretary of the Navy: USA.
3. Keller, T. M., *Imide-containing phthalonitrile resin.* Polymer, 1993. **34**(5): p. 952-955.
4. Keller, T. M., *Synthesis and polymerization of multiple aromatic ether phthalonitriles.* Chemistry of Materials, 1994. **6**(3): p. 302-305.
5. Keller, T. M. and Dominguez, D. D., *High temperature resorcinol-based phthalonitrile polymer.* Polymer, 2005. **46**(13): p. 4614-4618.
6. Keller, T. M. and Moonay, D. J. *Bisphenol A6F-based phthalonitrile polymer for high temperature applications*. 1989. Dallas, TX, USA: Publ by ACS.
7. Rodeheaver, B. A. and Colton, J. S., *Open-celled microcellular thermoplastic foam.* Polymer Engineering and Science, 2001. **41**(3): p. 380-400.
8. Huang, Q., Klötzer, R., Seibig, B., and Paul, D., *Extrusion of microcellular polysulfone using chemical blowing agents.* Journal of Applied Polymer Science, 1998. **69**(9): p. 1753-1760.
9. Matuana, L. M., Park, C. B., and Balatinecz, J. J., *Processing and cell morphology relationships for microcellular foamed PVC/wood-fiber composites.* Polymer Engineering and Science, 1997. **37**(7): p. 1137-1147.
10. Zenkert, D. and Burman, M., *Tension, compression and shear fatigue of a closed cell polymer foam.* Composites Science and Technology, 2009. **69**(6): p. 785-792.
11. Bikerman, J. J., ed. *Foams*. 1973, Springer-Verlag: New York.
12. Weiser, E. S., Grimsley, B. W., Pipes, R. B., and Williams, M. K. *Polyimide foams from friable balloons*. 2002. Long Beach, CA.
13. Marvel, C. S. and Martin, M. M., *Polymeric phthalocyanines. II.* Journal of the American Chemical Society, 1959. **80**(24): p. 6600-6604.
14. Snow, A. W., Griffith, J. R., and Marullo, N. P., *Syntheses and characterization of heteroatom-bridged metal-free phthalocyanine network polymers and model compounds.* Macromolecules, 1984. **17**(8): p. 1614-1624.
15. Sastri, S. B. and Keller, T. M., *Phthalonitrile cure reaction with aromatic diamines.* Journal of Polymer Science, Part A: Polymer Chemistry, 1998. **36**(11): p. 1885-1890.
16. Sastri, S. B. and Keller, T. M. *Phthalonitrile polymer for high temperature applications*. 1998. Boston, MA, USA: ACS.
17. Laskoski, M., Dominguez, D. D., and Keller, T. M., *Synthesis and properties of a bisphenol a based phthalonitrile resin.* Journal of Polymer Science, Part A: Polymer Chemistry, 2005. **43**(18): p. 4136-4143.

18. Achar, B. N., Fohlen, G. M., and Parker, J. A., *Studies on heat-resistant thermosetting phthalocyanine polymers.* Journal of Applied Polymer Science, 1984. **29**(1): p. 353-359.

19. Boston, D. R. and Bailar Jr, J. C., *Phthalocyanine derivatives from 1,2,4,5-tetracyanobenzene or pyromellitic dianhydride and metal salts.* Inorganic Chemistry, 1972. **11**(7): p. 1578-1583.

20. Wöhrle, D. and Preußner, E., *Synthesis and Analytical Characterization of Polymers from Benzene-1,2,4,5-tetracarboxylic Acid Derivatives.* Makromolekulare Chemie, 1985. **186**: p. 2189-2207.

21. Laskoski, M. and Keller, T. M., *Phosphine oxide containing phthalonitriles*, 2008, The Government of the US, as represented by the Secrectary of the Navy US.

22. Laskoski, M., Dominguez, D. D., and Keller, T. M., *Synthesis and properties of aromatic ether phosphine oxide containing oligomeric phthalonitrile resins with improved oxidative stability.* Polymer, 2007. **48**(21): p. 6234-6240.

23. Dominguez, D. D. and Keller, T. M., *Low-melting phthalonitrile oligomers: Preparation, polymerization and polymer properties.* High Performance Polymers, 2006. **18**(3): p. 283-304.

24. Brunovska, Z., Lyon, R., and Ishida, H., *Thermal properties of phthalonitrile functional polybenzoxazines.* Thermochimica Acta, 2000. **357-358**: p. 195-203.

25. Brunovska, Z. and Ishida, H., *Thermal study on the copolymers of phthalonitrile and phenylnitrile-functional benzoxazines.* Journal of Applied Polymer Science, 1999. **73**(14): p. 2937-2949.

26. Pascal, T., Malinge, J., and Sillion, B., *Synthesis of polyphthalocyanines by an oxido-reduction reaction initiated by the benzhydrol functional group. II. Polymer study.* Journal of Polymer Science, Part A: Polymer Chemistry, 1989. **27**(8): p. 2777-2791.

27. Warzel, M. L. and Keller, T. M., *Tensile and fracture properties of a phthalonitrile polymer.* Polymer, 1993. **34**(3): p. 663-666.

28. Ting, R. Y., Keller, T. M., Price, T. R., and Poranski Jr, C. F. *Characterization of the cure of diether-linked phthalonitrile resins*. 1982. Atlanta, Ga, USA: ACS.

29. Keller, T. M. and Griffith, J. R., *The synthesis of highly fluorinated phthalonitrile resins and cure studies.* Journal of Fluorine Chemistry, 1979. **13**: p. 315-324.

30. Tomoda, H., Saito, S., Ogawa, S., and Shiraishi, S., *Synthesis of phthalocyanine from phthalonitrile with organic bases.* Chemistry Letters, 1980: p. 1277-1280.

31. Burchill, P. J., *On the formation and properties of a high-temperature resin from a bisphthalonitrile.* Journal of Polymer Science, Part A: Polymer Chemistry, 1994. **32**(1): p. 1-8.

32. Zaharia, T., Sullivan, J. L., Saied, S. O., Bosch, R. C. M., and Bijker, M. D., *Fast deposition of diamond-like hydrogenated carbon films.* Diamond and Related Materials, 2007. **16**(3): p. 623-629.

33. Lin, H. C., Shiue, S. T., Cheng, Y. H., Yang, T. J., Wu, T. C., and Lin, H. Y., *Characteristics of carbon coatings on optical fibers prepared by plasma enhanced chemical vapor deposition using different argon/methane ratios.* Carbon, 2007. **45**(10): p. 2004-2010.

34. Eryilmaz, O. L., Johnson, J. A., Ajayi, O. O., and Erdemir, A., *Deposition, characterization, and tribological applications of near-frictionless carbon films on glass and ceramic substrates.* Journal of Physics Condensed Matter, 2006. **18**(32): p. S1751-S1762.

35. Cappelli, E., Orlando, S., Mattei, G., Scilletta, C., Corticelli, F., and Ascarelli, P., *Nano-structured oriented carbon films grown by PLD and CVD methods.* Applied Physics A: Materials Science and Processing, 2004. **79**(8): p. 2063-2068.

36. Taylor, C. A. and Chiu, W. K. S., *Characterization of CVD carbon films for hermetic optical fiber coatings.* Surface and Coatings Technology, 2003. **168**(1): p. 1-11.

37. Ray, S. C., Fanchini, G., Tagliaferro, A., Bose, B., and Dasgupta, D., *Amorphous carbon films prepared by the "dip" technique: Deposition and film characterization.* Journal of Applied Physics, 2003. **94**(2): p. 870-878.

38. Di, C. A., Wei, D., Yu, G., Liu, Y., Guo, Y., and Zhu, D., *Patterned graphene as source/drain electrodes for bottom-contact organic field-effect transistors.* Advanced Materials, 2008. **20**(17): p. 3289-3293.

39. Li, N., Wang, Z., Zhao, K., Shi, Z., Gu, Z., and Xu, S., *Large scale synthesis of N-doped multi-layered graphene sheets by simple arc-discharge method.* Carbon, 2010. **48**(1): p. 255-259.

40. Sun, J., Lindvall, N., Cole, M. T., Teo, K. B. K., and Yurgens, A., *Large-area uniform graphene-like thin films grown by chemical vapor deposition directly on silicon nitride.* Applied Physics Letters, 2011. **98**(25).

41. Sutter, P. W., Flege, J. I., and Sutter, E. A., *Epitaxial graphene on ruthenium.* Nature Materials, 2008. **7**(5): p. 406-411.

42. Novoselov, K. S., Geim, A. K., Morozov, S. V., Jiang, D., Zhang, Y., Dubonos, S. V., Grigorieva, I. V., and Firsov, A. A., *Electric field in atomically thin carbon films.* Science, 2004. **306**(5696): p. 666-669.

43. Choucair, M., Thordarson, P., and Stride, J. A., *Gram-scale production of graphene based on solvothermal synthesis and sonication.* Nature Nanotechnology, 2009. **4**(1): p. 30-33.

44. Behabtu, N., Lomeda, J. R., Green, M. J., Higginbotham, A. L., Sinitskii, A., Kosynkin, D. V., Tsentalovich, D., Parra-Vasquez, A. N. G., Schmidt, J., Kesselman, E., Cohen, Y., Talmon, Y., Tour, J. M., and Pasquali, M., *Spontaneous high-concentration dispersions and liquid crystals of graphene.* Nature Nanotechnology, 2010. **5**(6): p. 406-411.

45. Harnisch, J. A., Gazda, D. B., Anderegg, J. W., and Porter, M. D., *Chemical Modification of Carbonaceous Stationary Phases by the Reduction of Diazonium Salts.* Analytical Chemistry, 2001. **73**(16): p. 3954-3959.

46. Lomeda, J., Doyle, C., Kosynkin, D., Hwang, W., and Tour, J., *Diazonium Functionalization of Surfactant-Wrapped Chemically Converted Graphene Sheets.* Journal of the American Chemical Society, 2008. **130**(48): p. 16201-16206.

47. Liu, C. L., Dong, W. S., Song, J. R., and Liu, L., *Evolution of microstructure and properties of phenolic fibers during carbonization.* Materials Science and Engineering A, 2007. **459**(1-2): p. 347-354.

48. Li, X., Larson, A. B., Jiang, L., Song, L., Prichard, T., Chawla, N., and Vogt, B. D., *Evolution of mechanical, optical and electrical properties of self-assembled mesostructured phenolic resins during carbonization.* Microporous and Mesoporous Materials, 2011. **138**(1-3): p. 86-93.

49. Tzeng, S. S. and Chr, Y. G., *Evolution of microstructure and properties of phenolic resin-based carbon/carbon composites during pyrolysis.* Materials Chemistry and Physics, 2002. **73**(2-3): p. 162-169.

50. Rhim, Y. R., Zhang, D., Fairbrother, D. H., Wepasnick, K. A., Livi, K. J., Bodnar, R. J., and Nagle, D. C., *Changes in electrical and microstructural properties of microcrystalline cellulose as function of carbonization temperature.* Carbon, 2010. **48**(4): p. 1012-1024.

51. Bourlinos, A. B., Georgakilas, V., and Zboril, R., *Easy deposition of amorphous carbon films on glass substrates.* Carbon, 2008. **46**(13): p. 1801-1804.

52. Nakano, Y. and Matsuo, M., *Carbonized properties of iodine-incorporated poly(vinyl alcohol) composite films prepared by gelation/crystallization from solution.* Langmuir, 2010. **26**(4): p. 2857-2863.

53. Castro-Muñiz, A., Martínez-Alonso, A., and Tascón, J. M. D., *Porosity development in chars from thermal decomposition of poly(p-phenylene terephthalamide).* Polymer Degradation and Stability, 2009. **94**(10): p. 1890-1894.

54. Donnet, C. and Erdemir, A., eds. *Tribology of diamond-like carbon films: fundamentals and applications*. 2008, Springer New York.

55. Tuinstra, F. and Koenig, J. L., *Raman spectrum of garphite.* Journal of Chemical Physics, 1970. **53**(3): p. 1126-1130.

56. Wang, Y., Alsmeyer, D. C., and McCreery, R. L., *Raman spectroscopy of carbon materials: Structural basis of observed spectra.* Chemistry of Materials, 1990. **2**(5): p. 557-563.

57. Li, X., Hayashi, J. i., and Li, C. Z., *FT-Raman spectroscopic study of the evolution of char structure during the pyrolysis of a Victorian brown coal.* Fuel, 2006. **85**(12-13): p. 1700-1707.

58. Hafeman, A. E., Zienkiewicz, K. J., Zachman, A. L., Sung, H. J., Nanney, L. B., Davidson, J. M., and Guelcher, S. A., *Characterization of the degradation mechanisms of lysine-derived aliphatic poly(ester urethane) scaffolds.* Biomaterials, 2011. **32**(2): p. 419-429.

59. Barbetta, A., Gumiero, A., Pecci, R., Bedini, R., and Dentini, M., *Gas-in-liquid foam templating as a method for the production of highly porous scaffolds.* Biomacromolecules, 2009. **10**(12): p. 3188-3192.

60. Salerno, A., Oliviero, M., Di Maio, E., Iannace, S., and Netti, P. A., *Design of porous polymeric scaffolds by gas foaming of heterogeneous blends.* Journal of Materials Science: Materials in Medicine, 2009. **20**(10): p. 2043-2051.

61. Klempner, D. and Frisch, K., eds. *Handbook of Polymeric Roams and Foam technology* 1991, Hanser Munich.

62. Gibson, L. J. and Ashby, M. F., eds. *Cellular solids, Structure and properties - Second edition*. 1997, Cambridge Uniersity Press: Cambridge, UK.

63. Elwell, M. J., Ryan, A. J., Gruenbaurer, H. J. M., Van Lieshout, H. C., and Thoen, J. A., *Correlated view of reaction kinetics and structure development during the reactive processing of water blown, flexible polyurethane foam.* Progress in rubber and plastics technology, 1993. **9**(2): p. 120-142.

64. Spitael, P., Macosko, C. W., and McClurg, R. B., *Block copolymer micelles for nucleation of microcellular thermoplastic foams.* Macromolecules, 2004. **37**(18): p. 6874-6882.

65. Zettlemoyer, A. C., ed. *Nucleation*. 1969, Marcel-Dekker: New York.

66. Colton, J. S. and Suh, N. P., *Nucleation of microcellular thermoplastic foam with additives: Part I: Theotrical considerations* Polymer Engineering and Science, 1987. **27**(7): p. 485-492.

67. Colton, J. S. and Suh, N. P., *Nucleation of microcellular thermoplastic foam with additives: Part II: Experimental results and discussion* Polymer Engineering and Science, 1987. **27**(7): p. 493-499.

68. McClurg, R. B., *Design criteria for ideal foam nucleating agents.* Chemical Engineering Science, 2004. **59**(24): p. 5779-5786.

69. Leung, S. N., Wong, A., Park, C. B., and Zong, J. H., *Ideal surface geometries of nucleating agents to enhance cell nucleation in polymeric foaming processes.* Journal of Applied Polymer Science, 2008. **108**(6): p. 3997-4003.

70. Lee, L. J., Zeng, C., Cao, X., Han, X., Shen, J., and Xu, G., *Polymer nanocomposite foams.* Composites Science and Technology, 2005. **65**(15-16 SPEC. ISS.): p. 2344-2363.

71. Rodríguez-Pérez, M. A., Velasco, J. I., Arencón, D., Almanza, O., and De Saja, J. A., *Mechanical characterization of closed-cell polyolefin foams.* Journal of Applied Polymer Science, 2000. **75**(1): p. 156-166.

72. Doroudiani, S. and Kortschot, M. T., *Polystyrene foams. I. Processing-structure relationships.* Journal of Applied Polymer Science, 2003. **90**(5): p. 1412-1420.

73. Zhang, Y., Rodrigue, D., and Ait-Kadi, A., *High-Density Polyethylene Foams. I. Polymer and Foam Characterization.* Journal of Applied Polymer Science, 2003. **90**(8): p. 2111-2119.

74. Street, J. R., Fricke, A. L., and Philip Reiss, L., *Dynamics of phase growth in viscous, non-newtonian liquids: Initial stages of growth.* Industrial and Engineering Chemistry Fundamentals, 1971. **10**(1): p. 54-64.

75. Amon, M. and Denson, C. D., *Study of The Dynamics of Foam Growth: Analysis of the Growth of Closely Spaced Spherical Bubbles.* Polymer Engineering and Science, 1984. **24**(13): p. 1026-1034.

76. Arefmanesh, A. and Advani, S. G., *Nonisothermal bubble growth in polymeric foams.* Polymer Engineering and Science, 1995. **35**(3): p. 252-260.

77. Pugh, R. J., *Foaming in chemical surfactant free aqueous dispersions of anatase (titanium dioxide) particles.* Langmuir, 2007. **23**(15): p. 7972-7980.

78. Dickinson, E., Ettelaie, R., Kostakis, T., and Murray, B. S., *Factors controlling the formation and stability of air bubbles stabilized by partially hydrophobic silica nanoparticles.* Langmuir, 2004. **20**(20): p. 8517-8525.

79. Hunter, T. N., Pugh, R. J., Franks, G. V., and Jameson, G. J., *The role of particles in stabilising foams and emulsions.* Advances in Colloid and Interface Science, 2008. **137**(2): p. 57-81.

80. Gonzenbach, U. T., Studart, A. R., Tervoort, E., and Gauckler, L. J., *Ultrastable particle-stabilized foams.* Angewandte Chemie - International Edition, 2006. **45**(21): p. 3526-3530.

81. Cohen-Addad, S., Krzan, M., Höhler, R., and Herzhaft, B., *Rigidity percolation in particle-laden foams.* Physical Review Letters, 2007. **99**(16).

82. Alargova, R. G., Warhadpande, D. S., Paunov, V. N., and Velev, O. D., *Foam superstabilization by polymer microrods.* Langmuir, 2004. **20**(24): p. 10371-10374.

83. Thareja, P., Ising, B. P., Kingston, S. J., and Velankar, S. S., *Polymer foams stabilized by particles adsorbed at the air/polymer interface.* Macromolecular Rapid Communications, 2008. **29**(15): p. 1329-1334.

84. Stocco, A., Rio, E., Binks, B. P., and Langevin, D., *Aqueous foams stabilized solely by particles.* Soft Matter, 2011. **7**(4): p. 1260-1267.

85. Landrock, A. H., ed. *Handbook of Plastic Foams: Types, Properties, Manufacture and Applications*. 1994, Noyes Publications: New Jersey.

86. Raghavan, S. R., Walls, H. J., and Khan, S. A., *Rheology of silica dispersions in organic liquids: New evidence for solvation forces dictated by hydrogen bonding.* Langmuir, 2000. **16**(21): p. 7920-7930.

87. Lau, K. T. and Hui, D., *Effectiveness of using carbon nanotubes as nano-reinforcements for advanced composite structures [4].* Carbon, 2002. **40**(9): p. 1605-1606.

88. Iijima, S. and Ichihashi, T., *Single-shell carbon nanotubes of 1-nm diameter.* Nature, 1993. **363**(6430): p. 603-605.

89. Luo, Z., Lu, Y., Somers, L. A., and Johnson, A. T. C., *High yield preparation of macroscopic graphene oxide membranes.* Journal of the American Chemical Society, 2009. **131**(3): p. 898-899.

90. Jang, B. Z. and Zhamu, A., *Processing of nanographene platelets (NGPs) and NGP nanocomposites: A review.* Journal of Materials Science, 2008. **43**(15): p. 5092-5101.

91. Jang, B. Z. and Huang, W. C., *Nano-scaled graphene plates*, in *United States Patent*2006.

92. Koo, J. H., Lao, S. C., Lee, J., Chen, D. Z., Lam, C., Yong, W., Londa, M., and Pilato, L. A., *Morphology and thermal characterization of nanographene platelets.* Journal of Materials Science, 2011. **46**(10): p. 3583-3589.

93. Debelak, B. and Lafdi, K., *Use of exfoliated graphite filler to enhance polymer physical properties.* Carbon, 2007. **45**(9): p. 1727-1734.

94. Ramanathan, T., Abdala, A. A., Stankovich, S., Dikin, D. A., Herrera-Alonso, M., Piner, R. D., Adamson, D. H., Schniepp, H. C., Chen, X., Ruoff, R. S., Nguyen, S. T., Aksay, I. A., Prud'Homme, R. K., and Brinson, L. C., *Functionalized graphene sheets for polymer nanocomposites.* Nature Nanotechnology, 2008. **3**(6): p. 327-331.

95. Bao, C., Guo, Y., Song, L., Kan, Y., Qian, X., and Hu, Y., *In situ preparation of functionalized graphene oxide/epoxy nanocomposites with effective reinforcements.* Journal of Materials Chemistry, 2011. **21**(35): p. 13290-13298.

96. Kim, H., Kobayashi, S., Abdurrahim, M. A., Zhang, M. J., Khusainova, A., Hillmyer, M. A., Abdala, A. A., and MacOsko, C. W., *Graphene/polyethylene nanocomposites: Effect of polyethylene functionalization and blending methods.* Polymer, 2011. **52**(8): p. 1837-1846.

97. Lin, W., Zhang, R., and Wong, C. P., *Modeling of thermal conductivity of graphite nanosheet composites.* Journal of Electronic Materials, 2010. **39**(3): p. 268-272.

98. Xie, X. L., Mai, Y. W., and Zhou, X. P., *Dispersion and alignment of carbon nanotubes in polymer matrix: A review.* Materials Science and Engineering R: Reports, 2005. **49**(4).

99. Kelly, B. T., *The thermal expansion coefficient of graphite parallel to the basal planes.* Carbon, 1972. **10**(4): p. 429-433.

100. Qi, K., Zhang, G., Li, S., Liu, L., and He, Z., *Preparation and properties of high performance polyimide foam*, 2011: Qingdao. p. 66-71.

101. Zhai, W., Yu, J., Wu, L., Ma, W., and He, J., *Heterogeneous nucleation uniformizing cell size distribution in microcellular nanocomposites foams.* Polymer, 2006. **47**(21): p. 7580-7589.

102. Sharudin, R. W., Nabil, A., Taki, K., and Ohshima, M., *Polypropylene-dispersed domain as potential nucleating agent in PS and PMMA solid-state foaming.* Journal of Applied Polymer Science, 2011. **119**(2): p. 1042-1051.

103. Shen, J., Zeng, C., and Lee, L. J., *Synthesis of polystyrene-carbon nanofibers nanocomposite foams.* Polymer, 2005. **46**(14): p. 5218-5224.

104. Mahfuz, H., Rangari, V. K., Islam, M. S., and Jeelani, S., *Fabrication, synthesis and mechanical characterization of nanoparticles infused polyurethane foams.* Composites Part A: Applied Science and Manufacturing, 2004. **35**(4): p. 453-460.

105. Nam, P. H., Maiti, P., Okamoto, M., Kotaka, T., Nakayama, T., Takada, M., Ohshima, M., Usuki, A., Hasegawa, N., and Okamoto, H., *Foam processing and cellular structure of polypropylene/clay nanocomposites.* Polymer Engineering and Science, 2002. **42**(9): p. 1907-1918.

106. Strauss, W. and D'Souza, N. A., *Supercritical $CO_2$ processed polystyrene nanocomposite foams.* Journal of Cellular Plastics, 2004. **40**(3): p. 229-241.

107. Zeng, C., Han, X., Lee, L. J., Koelling, K. W., and Tomasko, D. L., *Polymer-Clay Nanocomposite Foams Prepared Using Carbon Dioxide.* Advanced Materials, 2003. **15**(20): p. 1743-1747.

108. Han, X., Zeng, C., Lee, L. J., Koelling, K. W., and Tomasko, D. L., *Extrusion of Polystyrene Nanocomposite Foams With Supercritical CO 2.* Polymer Engineering and Science, 2003. **43**(6): p. 1261-1275.

109. Haibach, K., Menner, A., Powell, R., and Bismarck, A., *Tailoring mechanical properties of highly porous polymer foams: Silica particle reinforced polymer foams via emulsion templating.* Polymer, 2006. **47**(13): p. 4513-4519.

110. Saha, M. C., Kabir, M. E., and Jeelani, S., *Enhancement in thermal and mechanical properties of polyurethane foam infused with nanoparticles.* Materials Science and Engineering A, 2008. **479**(1-2): p. 213-222.

111. Rivera-Armenta, J. L., Heinze, T., and Mendoza-Martínez, A. M., *New polyurethane foams modified with cellulose derivatives.* European Polymer Journal, 2004. **40**(12): p. 2803-2812.

112. Feng, H., Wang, X., and Xia, H., *Preparation of polyurethane/carbon nanotubes composites foam through in situ polycondensation.* Acta Polymerica Sinica, 2009(9): p. 953-957.

113. Verdejo, R., Saiz-Arroyo, C., Carretero-Gonzalez, J., Barroso-Bujans, F., Rodriguez-Perez, M. A., and Lopez-Manchado, M. A., *Physical properties of silicone foams filled with carbon nanotubes and functionalized graphene sheets.* European Polymer Journal, 2008. **44**(9): p. 2790-2797.

114. Verdejo, R., Barroso-Bujans, F., Rodriguez-Perez, M. A., De Saja, J. A., and Lopez-Manchado, M. A., *Functionalized graphene sheet filled silicone foam nanocomposites.* Journal of Materials Chemistry, 2008. **18**(19): p. 2221-2226.

115. Kim, S. H., Lee, M. C., Kim, H. D., Park, H. C., Jeong, H. M., Yoon, K. S., and Kim, B. K., *Nanoclay reinforced rigid polyurethane foams.* Journal of Applied Polymer Science, 2010. **117**(4): p. 1992-1997.

116. Thirumal, M., Khastgir, D., Singha, N. K., Manjunath, B. S., and Naik, Y. P., *Effect of a nanoclay on the mechanical, thermal and flame retardant properties of rigid polyurethane foam.* Journal of Macromolecular Science, Part A: Pure and Applied Chemistry, 2009. **46**(7): p. 704-712.

117. Mondal, P. and Khakhar, D. V., *Rigid polyurethane-clay nanocomposite foams: Preparation and properties.* Journal of Applied Polymer Science, 2007. **103**(5): p. 2802-2809.

118. Wouterson, E. M., Boey, F. Y. C., Hu, X., and Wong, S. C., *Effect of fiber reinforcement on the tensile, fracture and thermal properties of syntactic foam.* Polymer, 2007. **48**(11): p. 3183-3191.

119. Svagan, A. J., Samir, M. A. S. A., and Berglund, L. A., *Biomimetic foams of high mechanical performance based on nanostructured cell walls reinforced by native cellulose nanofibrils.* Advanced Materials, 2008. **20**(7): p. 1263-1269.

120. Cook, B. A., Yudin, V. E., and Otaigbe, J. U., *Thermal properties of polyimide foam composites.* Journal of Materials Science Letters, 2000. **19**(21): p. 1971-1973.

121. Istrate, O. M. and Chen, B., *Relative modulus-relative density relationships in low density polymer-clay nanocomposite foams.* Soft Matter, 2011. **7**(5): p. 1840-1848.

122. Technical white paper, *Performance of high temperature plastics*, 2005, Zeus Industurial Products Inc.

123. Keller, T. M., *Phthalonitrile resin as a carbon source.* Polymer communications Guildford, 1990. **31**(6): p. 229-231.

124. Nielsen, L. E. and Landel , R. F., eds. *Mechanical Properties of Polymers and Composites*. 1993, CRC Press

125. Kissenger, H. E., *Reaction Kinetics in Differential Thermal Analysis.* Analytical Chemistry, 1957. **29**(11): p. 1702-1706.

126. Achar, B. N., Fohlen, G. M., and Parker, J. A., *A new solid-phase polymerization—metal phthalocyanine sheet polymers.* Journal of Polymer Science: Polymer Chemistry Edition, 1983. **21**(2): p. 589-597.

127. Vogt, B. D., Chavez, V. L., Dai, M., Arreola, M. R. C., Song, L., Feng, D., Zhao, D., Perera, G. M., and Stein, G. E., *Impact of film thickness on the morphology of mesoporous carbon films using organic-organic self-assembly.* Langmuir, 2011. **27**(9): p. 5607-5615.

128. Fan, H., Hartshorn, C., Buchheit, T., Tallant, D., Assink, R., Simpson, R., Kissel, D. J., Lacks, D. J., Torquato, S., and Brinker, C. J., *Modulus-density scaling behaviour and framework architecture of nanoporous self-assembled silicas.* Nature Materials, 2007. **6**(6): p. 418-423.

129. Ebbesen, T. W. and Ajayan, P. M., *Large-scale synthesis of carbon nanotubes.* Nature, 1992. **358**(6383): p. 220-222.

130. Han, J., Kim, H., Kim, D. Y., Jo, S. M., and Jang, S. Y., *Water-soluble polyelectrolyte-grafted multiwalled carbon nanotube thin films for efficient counter electrode of dye-sensitized solar cells.* ACS Nano, 2010. **4**(6): p. 3503-3509.

131. Liu, K., Sun, Y., Liu, P., Lin, X., Fan, S., and Jiang, K., *Cross-stacked superaligned carbon nanotube films for transparent and stretchable conductors.* Advanced Functional Materials, 2011. **21**(14): p. 2721-2728.

132. Sedláčková, K., Lobotka, P., Vávra, I., and Radnóczi, G., *Structural, electrical and magnetic properties of carbon-nickel composite thin films.* Carbon, 2005. **43**(10): p. 2192-2198.

133. Walton, T. R., Griffith, J. R., and Reardon, J. P., *Electrical conducting polymers froms conjuated bis-phthalonitrile monomers* Journal of Applied Polymer Science, 1985. **30**(7): p. 2921-2939.

134. Ferrari, A. C. and Robertson, J., *Interpretation of Raman spectra of disordered and amorphous carbon.* Physical Review B - Condensed Matter and Materials Physics, 2000. **61**(20): p. 14095-14107.

135. Gibson, L. J., *Mechanical behavior of metallic foams.* Annual Review of Materials Science, 2000. **30**: p. 191-227.

136. Simone, A. E. and Gibson, L. J., *Effects of solid distribution on the stiffness and strength of metallic foams.* Acta Materialia, 1998. **46**(6): p. 2139-2150.

137. Santhosh Kumar, K. S., Reghunadhan Nair, C. P., and Ninan, K. N., *Mechanical properties of polybenzoxazine syntactic foams.* Journal of Applied Polymer Science, 2008. **108**(2): p. 1021-1028.

138. Kanny, K., Mahfuz, H., Thomas, T., and Jeelani, S., *Static and Dynamic Characterization of Polymer Foams Under Shear Loads.* Journal of Composite Materials, 2004. **38**(8): p. 629-639.

139. Rangari, V. K., Hassan, T. A., Zhou, Y., Mahfuz, H., Jeelam, S., and Prorok, B. C., *Cloisite clay-infused phenolic foam nanocomposites.* Journal of Applied Polymer Science, 2007. **103**(1): p. 308-314.

140. Cao, X., James Lee, L., Widya, T., and Macosko, C., *Polyurethane/clay nanocomposites foams: Processing, structure and properties.* Polymer, 2005. **46**(3): p. 775-783.

141. Dos-Santos, C. G., Costa, M. A., De Morais, W. A., and Pasa, V. M. D., *Phenolic foams from wood tar resols.* Journal of Applied Polymer Science, 2010. **115**(2): p. 923-927.

142. Zhang, L., Yilmaz, E. D., Schjødt-Thomsen, J., Rauhe, J. C., and Pyrz, R., *MWNT reinforced polyurethane foam: Processing, characterization and modelling of mechanical properties.* Composites Science and Technology, 2011. **71**(6): p. 877-884.

143. Leung, S. N., Wong, A., Guo, Q., Park, C. B., and Zong, J. H., *Change in the critical nucleation radius and its impact on cell stability during polymeric foaming processes.* Chemical Engineering Science, 2009. **64**(23): p. 4899-4907.

144. Gambaryan-Roisman, T., *Dynamics of free liquid films during formation of polymer foams.* Colloids and Surfaces A: Physicochemical and Engineering Aspects, 2011. **382**(1-3): p. 113-117.

145. Kristen, N. and Von Klitzing, R., *Effect of polyelectrolyte/surfactant combinations on the stability of foam films.* Soft Matter, 2010. **6**(5): p. 849-861.

146. Brent S, M., *Stabilization of bubbles and foams.* Current Opinion in Colloid & Interface Science, 2007. **12**(4-5): p. 232-241.

147. Louvet, N., Rouyer, F., and Pitois, O., *Ripening of a draining foam bubble.* Journal of Colloid and Interface Science, 2009. **334**(1): p. 82-86.

148. Jashnani, I. L. and Lemlich, R., *Foam drainage, surface viscosity, and bubble size bias.* Journal of Colloid and Interface Science, 1974. **46**(1): p. 13-16.

149. Binks, B. P. and Rodrigues, J. A., *Enhanced stabilization of emulsions due to surfactant-induced nanoparticle flocculation.* Langmuir, 2007. **23**(14): p. 7436-7439.

150. Britan, A., Liverts, M., Ben-Dor, G., Koehler, S. A., and Bennani, N., *The effect of fine particles on the drainage and coarsening of foam.* Colloids and Surfaces A: Physicochemical and Engineering Aspects, 2009. **344**(1-3): p. 15-23.

151. Sun, Q., Tan, L., and Wang, G., *Liquid foam drainage: An overview*. International Journal of Modern Physics B, 2008. **22**(15): p. 2333-2354.

152. Lei, S., Guo, Q., Shi, J., and Liu, L., *Preparation of phenolic-based carbon foam with controllable pore structure and high compressive strength.* Carbon, 2010. **48**(9): p. 2644-2646.

153. Li, S., Song, Y., Shi, J., Liu, L., Wei, X., and Guo, Q., *Carbon foams with high compressive strength derived from mixtures of mesocarbon microbeads and mesophase pitch.* Carbon, 2007. **45**(10): p. 2092-2097.

154. Beechem, T. and Lafdi, K., *Novel high strength graphitic foams.* Carbon, 2006. **44**(8): p. 1548-1559.

155. Zhao, X., Lai, S., Liu, H., and Gao, L., *Preparation and characterization of activated carbon foam from phenolic resin.* Journal of Environmental Sciences, 2009. **21**(SUPPL. 1): p. S121-S123.

# APPENDICES

I. Curing Kinetics Studies of RPh Resins

II. Degradation Kinetics of RPh Resin

III. MWNT Surface Modification

IV. Supporting Figures

# I Curing Kinetics Studies of RPh Resin

To compare the curing reaction of RPh in the presence of APB, dynamic kinetic analysis was performed using an established non-isothermal kinetic model, the Kissinger model[125]. This model does not require prior knowledge of the reaction mechanism for thermoset curing, this is especially useful for RPh resin because of the complex curing reactions. The activation energy ($E_a$) for curing was obtained by Equation I-1:

$$ln\left(qT_{peak}^{\ 2}\right) = ln\left(\frac{AR}{E_a}\right) + \left(\frac{1}{T_{peak}}\right)\left(\frac{E_a}{R}\right) \qquad \textbf{Equation I-1}$$

where $T_{peak}$ is the peak exotherm temperature from dynamic DSC scans, q is the constant heating rate, and R is the universal gas constant. The value of $E_a$ in this simplistic equation can be obtained from the slope of the plot in ($q/T_{peak}^2$) versus $1/T_{peak}$ without the need to make any assumption with conversion-dependant function. Figure I-1 shows the typical DSC thermograms from the dynamic heating experiments conducted at rates between 5 and 20 °C/min. Table I-1 summarized the peak isotherm temperatures ($T_{peak}$) and the calculated $E_a$ obtained from the dynamic kinetics analysis model.

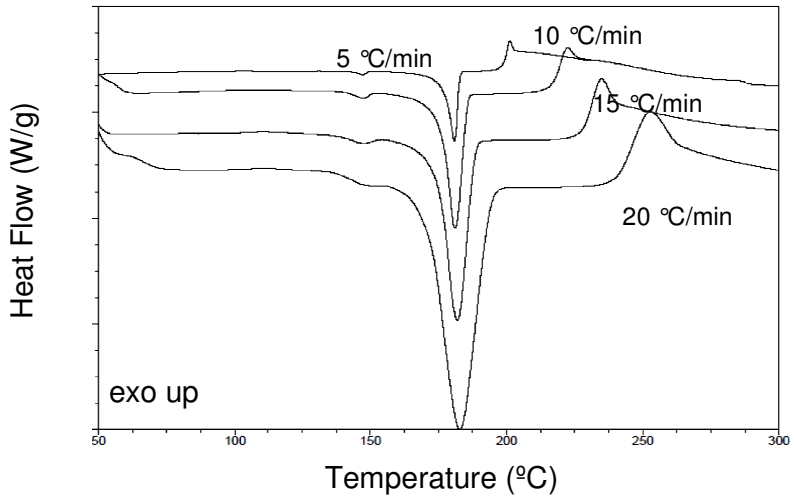


**Figure I-1 Typical dynamic DSC thermograms of RPh/APB system.**

For the system without the additive, there was no curing peak being observed from dynamic heating up to 400 °C or under isothermal heating at 200 °C. The resin remained as liquid for days at 200 °C and no viscosity increase was detected. The reaction time was significantly reduced by the addition of APB from days to merely 2 hours. Table I-1 shows that as the amount of APB increases, reaction isotherms shifted to higher temperature and the calculated $E_a$ values increased, an indication of reactions requires higher activation energy. Clearly in this case, APB is not functioning as a catalyst as it did not reduce the curing activation energy. The shift in temperature and increased $E_a$ values could be due to the higher amount of energy required to support different types of reactions involving the formation of macrocyclic and linear polymeric molecules structures simultaneously.

**Table I-1 Peak exotherm temperatures at different heating rates and the corresponding $E_a$ of the RPh/APB systems obtained by Kissinger method.**

| q(°C/min) | $T_{peak}$ °C for various amount of curing additives | | | | | | |
|---|---|---|---|---|---|---|---|
| | 0mol% | 1mol% | 2mol% | 5mol% | 10mol% | 15mol% | 20mol% |
| 5 | * | 226 | 238 | 245 | 253 | 260 | 269 |
| 10 | * | 246 | 251 | 255 | 270 | 276 | 289 |
| 15 | * | 263 | 270 | 273 | 276 | 283 | 294 |
| 20 | * | 274 | 279 | 285 | 289 | 296 | 315 |
| $E_a$ (kJ/mol) | - | 57.9 | 49.1 | 63.9 | 87.1 | 92.6 | 98.2 |

*** No exotherm was observed from dynamic heating from 50-400°C.**

# II Degradation Kinetics of RPh Resin

Thermal decomposition of a material is characterized by both the initial degradation temperature and the degradation rate. The thermal decomposition kinetics of RPh/APB systems were studied by TGA at different heating rates both in $N_2$ and in air. The apparent degradation activation energy ($E_d$) was determined by the Kissinger[125] method based Equation II-1 and determined from the plot of $ln(\alpha/T_{max})$ versus $1000/T_{max}$. This method is an ideal model to be used for systems with complicated degradation mechanisms since the calculation is independent of the reaction order.

$$ln\frac{\alpha}{T_{max}^2} = \ln\left(\frac{nRAW_{max}^{n-1}}{E_a}\right) - \frac{E_d}{RT_{max}} \qquad \textbf{Equation II-1}$$

in which α is the heating rate, $T_{max}$ is the temperature at the maximum rate of weight loss, n is the apparent reaction order, R is the universal gas constant and $W_{max}$ is the residual weight at maximum rate of weight loss. Average $T_{max}$ values of repeated TGA runs were used for calculation.

Figure II-1 shows DTGA curves of RPh/APB (5 mol% APB was used as illustration) systems at different heating rates in $N_2$ and air. One prominent degradation step was clearly shown in $N_2$ and multiple steps were observed in air. $E_d$ values were calculated based on the main degradation stage. The degradation stages after 700 °C could be likely due to oxidation weight loss and were ignored. Figure II-2 shows the Kissinger plots of thermal decomposition in $N_2$ for systems containing 0, 5 and 10 mol% of APB respectively, the linear relationship confirmed the validity of the equation used.

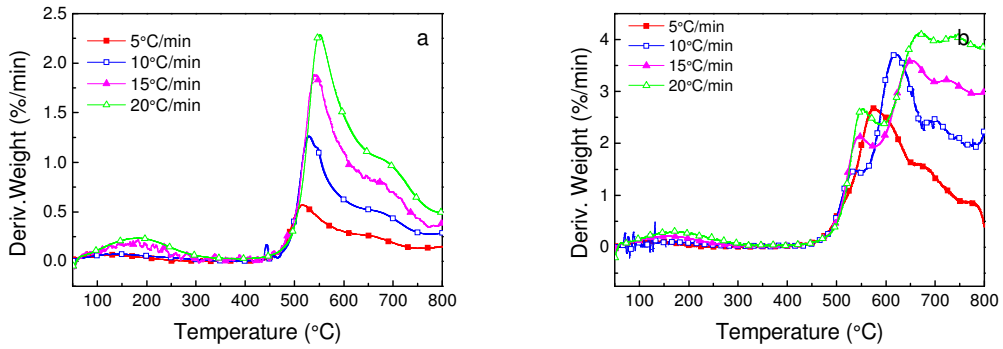


**Figure II-1 DTGA curves of typical RPh/APB system at different heating rate in (a) $N_2$ and (b) air.**

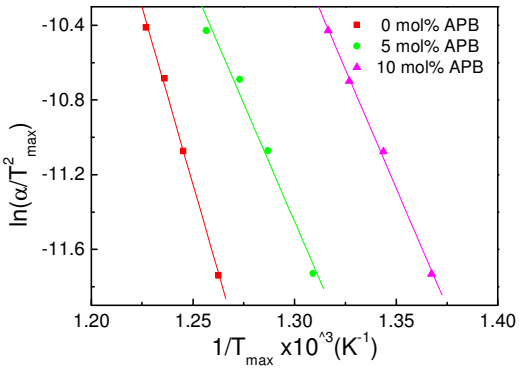


**Figure II-2 Kissinger plots of the main degradation stage of RPh/APB systems in $N_2$.**

$E_d$ and the corresponding linear fit regression coefficients are summarized in Table II-1. Resin system without the curing additive has the highest $E_d$ value of 326.6 kJ/mol. Upon addition of 2 mol% of APB, $E_d$ dropped substantially to 237.5 kJ/mol. The variation in activation energy for curing at different APB content has clearly indicated the distinct structures formed during curing which should led to very different degradation behaviour and kinetics. However the $E_d$ values varied in a relatively narrow zone between 212 and 240 kJ/mol. The thermal stability and degradation were independent to the amount of amine added, which contradicted what Keller had reported [1]. Therefore it is essential to

carry out detail studies on the structural formation at different APB content to generate understandings and elucidate the relationship between structural formation and the thermal properties. It will also aid in the selection of the optimum processing conditions and structural characteristics for further developments.

**Table II-1 $T_{max}$ and Ed of the major degradation stage of RPh/APB resin in $N_2$ and in air calculated by the Kissinger equation.**

| | | $T_{max}$ | | | | |
|---|---|---|---|---|---|---|
| APB content (mol%) | | 0 | 2 | 5 | 10 | 20 |
| 5 ºC/min | | 519 | 517 | 515 | 516 | 520 |
| 10 ºC/min | | 530 | 533 | 528 | 531 | 535 |
| 15 ºC/min | | 536 | 543 | 538 | 542 | 545 |
| 20 ºC/min | | 542 | 547 | 549 | 549 | 550 |
| $E_d$ (kJ/mol) | $N_2$ | 326.6 | 237.5 | 212.1 | 221.5 | 232.6 |
| | $R^{2*}$ | 0.9996 | 0.9992 | 0.9866 | 0.9963 | 0.9976 |
| | Air | 175.0 | 82.4 | 83.0 | 83.3 | 82.6 |

*** $R^2$: linear fit regression coefficient**

# III MWNT and GH Surface Modifications

It is well known that pristine MWNT agglomerate due to surface interaction. The surfaces were acid treated to enhance the dispersion in solution and in polymer matrix. The pristine MWNT is rather long (up to hundred of microns) through SEM observation; the length was shortened by ball milling. This significantly reduced the length and introduced defects on the MWNT surfaces to facilitate the surface modification.

MWNT was ball milled by pulveriser from Pulverisette for 6 hours at 250 rpm before subjected to surface modification. 3 g of the ball milled sample was stirred in 300 mL of 3:1 (v/v) concentrated $H_2SO_4$ (98%) and $HNO_3$ (69%) mixture, both obtained from Sigma-Aldrich, used as received. The mixture was ultrasonicated in a water bath (Elma S40H) for 6 hours at 35 ºC, centrifuged to separate the solid from the acid followed by neutralization until the filtrate reached pH 6 with deionized water. The MWNT residue obtained by vacuum assisted filtration was freeze dried.

**Graphite Surface Modification**

Natural flake graphite was pre-dried dried followed by stirring in a mixture of concentrated $H_2SO_4$ (98%) and $HNO_3$ (69%) (4:1, v/v). The mixture was filtered and neutralized until the filtrate reach pH 6 with deionized water. The neutralized graphite was filtered and freeze dried. The dried graphite was subjected to thermal shock at 1050ºC for about 20 seconds forming expanded graphite. The expanded graphite was probe sonicated under high power in ethanol for 14 hours before the solvent was removed and dried thoroughly to yield graphite nanosheets (GH).

**Nanofillers Dispersion and Morphology Characterization**

FS, MWNT and GH were sonicated (Vibra-Cell™ Ultasonic Processor) under high energy for 15 minutes in acetone to form a homogeneous suspension. The filler dispersed solvent was added to RPh monomer and transferred to water sonication (Elma, S40H) for another 2 hours to further enhance the filler dispersion. Solvent was removed by rotary evaporator and the mixture was dried in vacuum oven overnight. The dried mixture was melt blended for 2 hours before curing additives was added. Samples were fractured and sputter coated with platinum for dispersion characterization by FESEM (JOEL F6360).

**Nanofillers Treatment and Dispersion**

Treated MWNT and GH were shown in Figure III-1. The length of MWNT was reduced from hundreds of micrometer (μm) to few μm. GH with an average sheet diameter range of 5-20 μm and 30-80 nm in thickness were obtained.

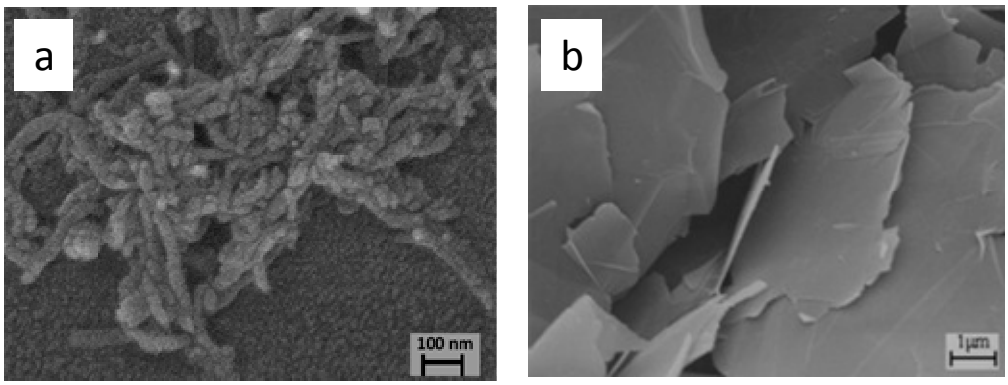


**Figure III-1 SEI images of the treated MWNT and GH.**

# IV Supporting Figures

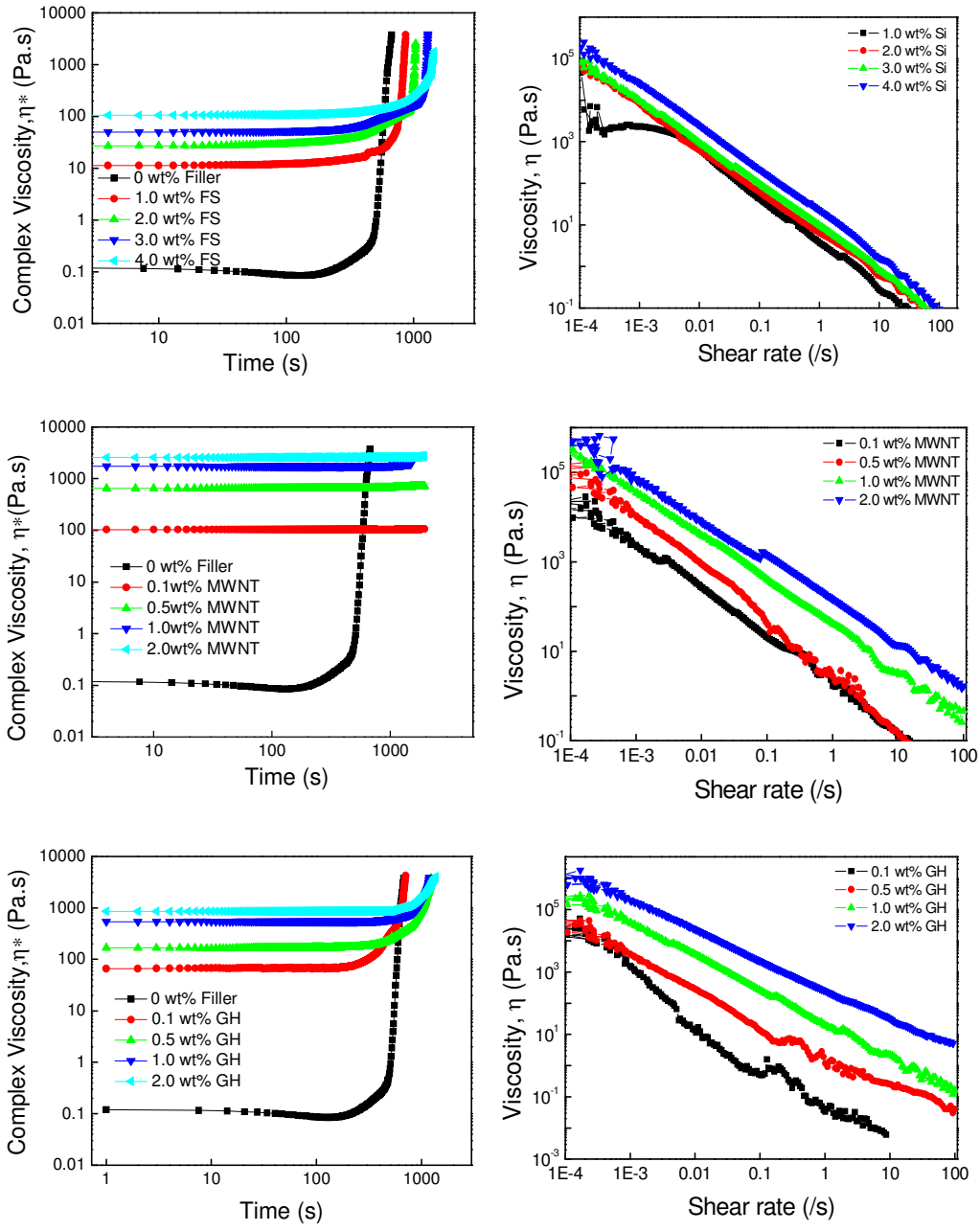


**Figure IV-1 Complex viscosity of RPh/nanofillers systems as a function of time at constant shear rate of 1/s and viscosity change under dynamic shear rate.**

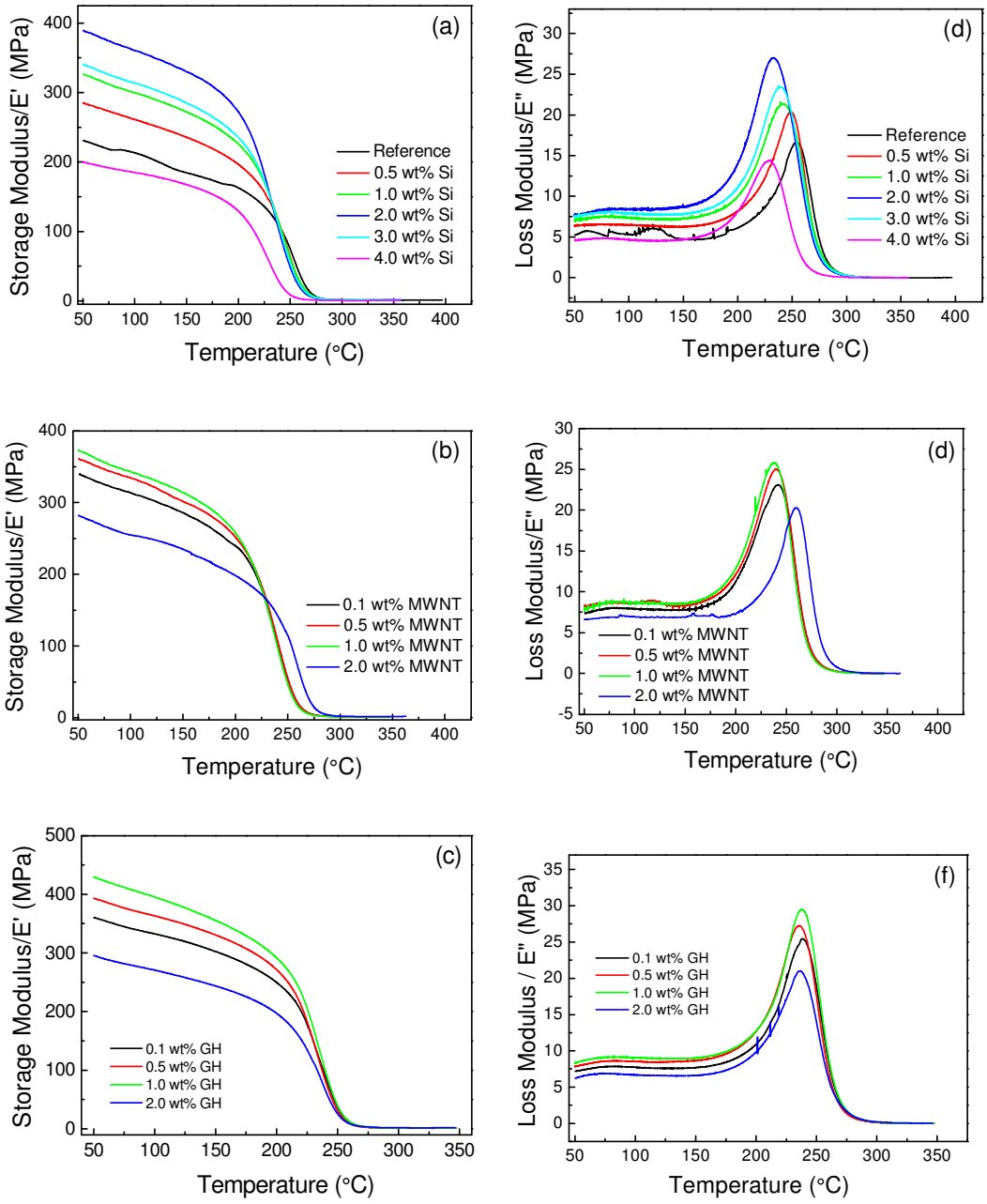


**Figure IV-2 Storage modulus and loss modulus of the nanocomposite foams (a) (d): RPh/FS, (b) (e): RPh/MWNT, and (c) (f): RPh/GH. Pure RPh foams were included in (a) and (d) as reference. Reference is taken as 0 wt% filler.**